Fall 12-2010

The Influence of Nanoporous Crystalline Structure on Low Molecular Weight Mass Transport in Syndiotactic Polystyrene

Justin Paul Brandt
University of Southern Mississippi

The University of Southern Mississippi

THE INFLUENCE OF NANOPOROUS CRYSTALLINE STRUCTURE ON LOW MOLECULAR WEIGHT MASS TRANSPORT IN SYNDIOTACTIC POLYSTYRENE

by

Justin Paul Brandt

Abstract of a Dissertation
Submitted to the Graduate School
of The University of Southern Mississippi
in Partial Fulfillment of the Requirements
for the Degree of Doctor of Philosophy

December 2010

ABSTRACT

THE INFLUENCE OF NANOPOROUS CRYSTALLINE STRUCTURE ON LOW MOLECULAR WEIGHT MASS TRANSPORT IN SYNDIOTACTIC POLYSTYRENE

by Justin Paul Brandt

December 2010

Solid-state structure, crystalline morphology, crystallization kinetics, thermal, free volume, and gas transport properties of semicrystalline *syndiotactic* polystyrene (sPS) and ethylene vinyl alcohol copolymers (EVOH) have been investigated. Solid-state structure of sPS after crystallization from the melt and glassy state was examined by differential scanning calorimetry (DSC), density and wide angle x-ray diffraction analysis (WAXD). The measurements confirmed low density of *syndiotactic* polystyrene crystalline forms, which in the case of α and δ_e was smaller and in the case of β and γ crystalline forms was slightly larger than the density of the glassy amorphous sPS. Positron annihilation lifetime spectroscopy (PALS) experiments have been carried out to study the free volume properties of these materials.

The diffusion characteristics of amorphous, α, and β forms of sPS were successfully measured via a custom made dynamic gas permeation system utilizing a mass-spectrometer. It was shown experimentally that the amorphous and β forms demonstrate similar diffusion. Conversely, experimental results as well as molecular dynamics simulations have shown that the unique "superstructure," packing of triplets forming hexagonally shaped nanochannels along the chain direction, found in the α form of sPS, facilitate high diffusion rates parallel to the chain direction in larger permeants (greater than 2.6Å). This was attributed to a transition from a nearly 3-dimensional behavior for small permeant size, to a 1-dimensional behavior for larger permeant sizes. Larger permeants are confined to the hexagonally shaped nanochannels between the triplets in the α" form, and cannot move between parallel channels. The smaller permeants,

however, can move relatively freely between neighboring channels, resulting in a 3-dimensional diffusion behavior.

The vapor sorption of several industrial and chemical simulants within semicrystalline domains of syndiotactic polystyrene was studied with a quartz crystal microbalance. To increase the overall sensitivity of the sensing medium a new method for sample preparation was proposed. This method has utilized the ability to prepare high degrees of γ phase crystallinity, through supercritical CO_2, to generate highly δe crystalline samples via crystalline-crystalline solid state transitions. Sorption characteristics are established as a function of crystalline fraction and chemical properties of the test analytes. It has been demonstrated experimentally that increased crystallinity directly influences the sensitivity of the sensing medium. The use of δ_e crystalline phase sPS as a sensing medium in cooperation with QCM to selectively detect the chemical warfare simulant 2-chloroethyl ethyl sulfide was shown.

Transport in a broad range of ethylene vinyl alcohol copolymers (EVOH) as it is related to hydrogen bonding interaction through a measure of free volume and cohesive energy characteristics was conducted. Solid state structure was probed utilizing wide angle x-ray diffraction, differential scanning calorimetry, density measurements, and positron annihilation lifetime spectroscopy, to directly study free volume behavior. Characteristic FTIR spectra of EVOH copolymers demonstrate that the width and intensity of the OH stretching vibration increase with increasing vinyl alcohol content. The measure of intermolecular interaction, cohesive energy density (CED), was calculated through group contribution methods and also obtained using molecular dynamics computer simulations. Oxygen transport characteristics of the copolymers, i.e. permeability, diffusivity, and solubility were measured and correlations were made between vinyl alcohol content, free volume, and CED.

The University of Southern Mississippi

THE INFLUENCE OF NANOPOROUS CRYSTALLINE STRUCTURE ON LOW MOLECULAR WEIGHT MASS TRANSPORT IN SYNDIOTACTIC POLYSTYRENE

by

Justin Paul Brandt

A Dissertation
Submitted to the Graduate School
of The University of Southern Mississippi
in Partial Fulfillment of the Requirements
for the Degree of Doctor of Philosophy

Approved:

Sergei Nazarenko
_____
Director

Kenneth Mauritz
_____

Sarah Morgan
_____

Jefferey Wiggins
_____

Robert Moore
_____

Susan A. Siltanen
_____
The Dean of the Graduate School

December 2010

ACKNOWLEDGMENTS

I would like to thank my graduate research advisor, Dr. Sergei Nazarenko, for his mentorship. It is with his motivation that I feel my future has been shaped in a positive direction. There are numerous others to whom I would like to extend my gratitude including my graduate committee members, Dr. Jeffrey Wiggins, Dr. Sarah Morgan, Dr. Kenneth Mauritz, and Dr. Robert Moore, for their advice and support throughout my graduate career in Polymer Science and Engineering. I would also like to express my appreciation to Dr. Brian Olson for his endless patience and always finding time to answer my questions.

Fellow graduates within the Nazarenko Research Group and the Polymer Science & Engineering department have my utmost respect and thanks for their continuous support. Financially, this work was supported by the Materials Research Science and Engineering Center (MRSEC), and Southeast Region Research Initiative (SERRI) Programs of the National Science Foundation.

TABLE OF CONTENTS

LIST OF TABLES

Table

LIST OF ILLUSTRATIONS

Figure

CHAPTER I

INTRODUCTION

The transport and sorption properties of a polymer are significantly affected by its composition and morphology. Factors relating to the chemical composition and structure of the polymer (secondary interactions, presence of side chains, and crosslinking) and those factors involving heterogeneities in the polymer (orientation, crystallinity, and the presence of plasticizers and fillers) exert the greatest influence.[1, 2] Among them, hydrogen bonding, crystallinity and crystalline morphology factors are of great importance for transport through polymeric membranes and will be discussed here.

Many membranes of practical interest are semicrystalline, as the crystallinity often gives them the necessary strength and temperature resistance. The effect of degree of crystallinity on the solubility and diffusivity has been studied before and it was shown that crystallites usually act as inert fillers in which gases would neither dissolve nor diffuse. [3] While most semi-crystalline polymers show little to no permeability through the crystalline phase due to high crystalline densities several polymers including *syndiotactic* polystyrene, *syndiotactic* poly-p-methyl styrene, and isotactic poly(4-methyl-pentene-1) have been known to exhibit unusually low crystalline densities. The low-density crystalline structure of α and δ *syndiotactic* polystyrene raises several interesting questions such as whether crystalline structure is permeable for transport of small molecules, what is the contribution of crystalline and amorphous phases to the entire diffusion mechanism in the semicrystalline polymer, and what role does host guest interaction play in sorption.

Chapter II explores syndiotactic polystyrene solid state structure, determination of the crystalline fraction, crystallization kinetics and nature of crystalline-crystalline transitions. Wide angle X-ray diffraction patterns of α, β, γ, δ and the mesomorphic phases are presented. Quantitative comparisons of the percent crystallinity for differential scanning calorimetry, wide

angle X-ray diffraction and density are reported. Heat of fusion for 100% α and β crystalline sPS, 56 and 52 ± 1 J g^{-1} respectively, is obtained though extrapolation of $\Delta H = H_m - H_{cc}$ with respect to density for a series of melt-crystallized and crystalline-crystalline manipulated samples. Weight fraction crystallinity versus density linear regression demonstrates the 100% γ form crystalline density to be 1.074 g cm^{-3}. Isothermal crystallization kinetics of γ phase sPS with respect to pressure is shown. Efficiency of step wise, carbon disulfide and supercritical CO_2 solvent extraction methods for removal of trapped solvents within the chlathrated δ form of sPS is also reported.

The goal of Chapter III is to elucidate the diffusion mechanism and the fundamental structural characteristics that control gas transport through semicrystalline polymers, which exhibit a porous crystalline structure permeable to small gas molecules. A novel approach to materials containing uniform nanochannels or nanopores with diameters less than 10 Å has been focused. Specifically, we center our attention on the solid state structure and gas transport behavior in thermally induced crystalline forms of sPS. The research objective is to study transport properties of various gases in semicrystalline α phase sPS, in order to probe the structure of the low-density crystalline phase and to examine the role of crystalline morphology on gas permeation behavior.

The primary emphasis of Chapter V revolves around the clathrated δ phase of syndiotactic polystyrene possessing host guest interactions. Previous work has revealed the potential of nanoporous δ crystalline form of sPS to predominantly absorb aromatic hydrocarbon and the halogenated low molecular compounds.[4-6] The capability of δ_e sPS to selectively absorb specific organic substances can be used to separate solvent mixtures or as a sensing elements in senorics. Mensitieri et al.[7] showed that nanoporous sPS can be used as sensing medium for development of quartz crystal microbalance sensors for detection of chlorinated compounds and other toxic volatile pollutants. The current research considers development of a new highly

sensitive quartz crystal microbalance based transducer for real-time detection in gaseous and aqueous environments the presence of dangerous chemical warfare agents. In particular, mono-functional sulfur mustard simulant, 2-chloroethyl ethyl sulfide (CEES), and dimethyl methylphosphonate (DMMP) a nerve agent simulant were explored. Both samples being of similar size and molecular weight allows for the exploration of chemical selectivity.

Though previous work has shown δ_e crystalline sPS to possess host cavity size selectivity, the question still remains as to what role electrostatic interactions play in the accommodation of guest molecules. In Chapter IV we systematically study the sorption characteristics between various linear chain alkyl halide test analytes to determine the role that electrostatic interactions and size play in the sorption of host sPS nanopores. Using classical thermodynamic models, differences in the Flory Huggins interaction parameter value as it relates to monosubstituted linear organohalides of varying electronegativity in amorphous and δ_e semicrystalline syndiotactic polystyrene are examined.

The main objective of Chapter VI is to establish a fundamental understanding of oxygen transport in a broad range of ethylene vinyl alcohol copolymers (EVOH) as it is related to hydrogen bonding interaction through a measure of free volume and cohesive energy characteristics. Ethylene vinyl alcohol (EVOH) copolymers with various ethylene contents (0, 24, 27, 32, 38, 44, 48, 60, 75, 82, 95 and 100 mol %), were used in this study. Solid state structure was probed utilizing wide angle x-ray diffraction, differential scanning calorimetry, density measurements, and positron annihilation lifetime spectroscopy, to directly study free volume behavior. Characteristic FTIR spectra of EVOH copolymers demonstrate that the width and intensity of the OH stretching vibration increase with increasing vinyl alcohol content. The measure of intermolecular interaction, cohesive energy density (CED), was calculated through group contribution methods and also obtained using molecular dynamics computer simulations. Oxygen transport characteristics of the copolymers, i.e. permeability, diffusivity, and solubility,

were measured and correlations were made between vinyl alcohol content, free volume, and CED. We have shown through a correlation of CED and glass transition that the degrees of freedom in expressions of kinetic energy of the chain backbones are constant across all EVOH copolymer compositions. It is shown at a given temperature that the primary factor controlling free volume is not chain rigidity but cohesive energy in this system with fractional free volume and CED being related through a modification of Van der Waals law. Furthermore, temperature measurements show a linear dependence of semi log permeability and diffusion coefficients with reciprocal average hole free volume and CED. It is demonstrated that temperature dependence of diffusion can be estimated directly from positron annihilation lifetime spectroscopy through energy of activation predictions.

References

1. Crank, J.; Park, G. S., In *Diffusion in Polymers*; Medgi P.; Academic Press: London and New York, 1968.

2. Rogers, C. E., In *Polymer Permeability*, Comyn, J., Ed.; Chapman & Hall: New York, 1985; pp 11-74.

3. Mayers, A. W.; Rogers, C. E.; Stannett, V.; Szwarc, M. *TAPPI* **1958,** *41*, 716.

4. Chatani, Y.; Shimane, Y.; Inoue, Y.; Inagaki, T.; Ishioka, T.; Ijitsu, T.; Yukinari, T. *Polymer* **1992,** *33*, 488.

5. Guerra, G.; Vitagliano, V. M.; De Rosa, C.; Petraccone, V.; Corradini, P. *Macromolecules* **1990,** *23*, 1539.

6. Immirzi, A.; de Candian, F.; Iannelli, P.; Vittoria, V.; Zambelli, A. *Makromol. Chem. Rapid Commun.* **1988,** *9*, 761.

7. Mensitieri, G.; Venditto, V.; Guerra, G. *Sensors and Actuators* **2003,** *B92*, 255-261.

CHAPTER II

SOLID STATE STRUCTURE AND CRYSTALLINE/CRYSTALLINE TRANSITIONS IN *SYNDIOTACTIC* POLYSTYRENE

Introduction

The primary objective of this section is characterization of syndiotactic polystyrene (sPS) solid state structure, determination of the crystalline fraction, study of crystallization kinetics and nature of crystalline-crystalline transitions. The correlation between the solid-state structure and several unusual properties are revealed. Highly stereoregular syndiotactic polystyrene (sPS) is a relatively new engineering thermoplastic polymer first obtained by Ishihara et al. in 1985. [1-3] A variety of titanium and zirconium compounds that are soluble in aromatic hydrocarbons in the presence of methylalumoxane (MAO), promote the syndiotactic polymerization of styrene with a tacticity greater than 98% via a polyinsertion mechanism. [4, 5] Specific characteristics that make sPS an exciting new engineering thermoplastic, both academically and industrially, include enhanced mechanical performance at elevated temperatures (T_m = 270°C), a high crystallization rate to enable processing by extrusion, broad availability of styrene monomer, excellent electrical properties, low crystalline density, good processing characteristics and low moisture content. In particular, the low-density crystalline structure raises several interesting questions such as whether crystalline structure is selectively permeable for small molecule gas transport, what is the contribution of crystalline and amorphous phases to the entire diffusion mechanism, and what is the role of crystalline morphology. Fundamental solid state structural analysis outlined in this chapter provides the foundation for subsequent work.

Polymorphism in Syndiotactic Polystyrene

Most semicrystalline polymers possess only one type of crystalline unit cell, while for others, polymorphism exist. The sPS solid-state crystalline structure is very complex, consisting of several polymorphic crystalline forms and a mesomorphic form. Syndiotactic polystyrene can crystallize in five main crystalline structures as assigned by Guerra et al.[6, 7] Two thermotropic or

thermally induced crystalline forms, α and β, as well as three lyotropic or solvent induced forms, γ, δ and ε are characteristic in sPS and will be explored with exception of the newly discovered ε form. These five crystalline forms differ according to conformational order and by the mode of crystalline packing within the same conformation order. Forms α and β have TTTT conformation (all trans planer zigzag chains) with an identity period of 5.1 Å, [1, 6, 8] while γ and δ have TTGG conformation (trans-trans-gauche-gauche helical chains) with an identity period of 7.7 Å.[9-11]

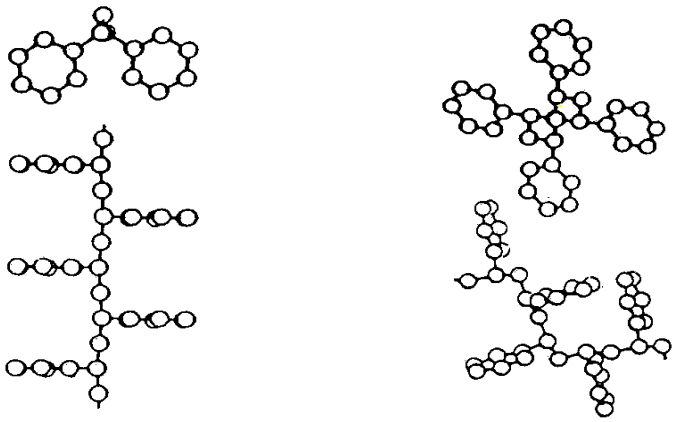

(A) (B)

Figure 1. Chain conformations for the (A) all trans α and β and the TTGG (B) γ and δ crystalline forms of sPS.

Many studies investigated phase transformation in sPS using Fourier transformation infrared (FT-IR) and/or Raman spectroscopy, differential scanning calorimetry (DSC), and X-ray analysis.[6, 12-17] In general, crystallization by cooling the melt or heating the glass produces the α or β forms, while crystallization in the presence of solvent generates the γ, δ and ε forms. Upon heating, sPS undergoes a glass transition at about 100°C and a cold crystallization at about 135°C to give the planar mesomorphic phase, which serves as a template for growth of the α form.[8] The α form can also be obtained by rapid cooling from the melt state or by heating the helical mesomorphic, δ or γ form. [6, 12, 18] The β form can be obtained by slow cooling from the melt or by

casting from a solution at elevated temperatures. [19] The α and β forms are further classified into structurally ordered (″) and disordered (′) phases. The disorder in α′ refers to the orientation of styrene triplet clusters statistically distributed between two values, while in the case of β′, the disorder corresponds to the stacking of ordered macromolecular bilayers. This leads to the existence of a cylindrical cavity in the α″ phase while the α′ lacks inter-lamella ordering necessary for continuous cavity formation. Depending on the solvent nature, the δ or γ crystal form is obtained when amorphous sPS is immersed in liquid solvent or directly exposed to solvent vapor and then dried. [13, 20] Generally, the δ form contains solvent molecules entrapped in the crystal structure, whereas the γ form is free of solvent. The mesomorphic phase with helical conformation is obtained by removing select solvent molecules from the δ-form just below glass transition temperature, and the mesomorphic phase with the zigzag conformation is obtained by annealing or stretching amorphous sPS above its T_g.[18, 21]

Adding to the complexity exhibited by sPS polymorphism, several crystalline-crystalline transitions exist. Due to the higher thermodynamic stability of the TTTT conformation over the TTGG conformation, γ and δ forms can undergo thermal transitions to give the α form but rarely the kinetically unfavorable β form.[22] The complex thermal transitions are well illustrated upon consideration of the δ_e sPS sample heated from room temperature to melting. Upon heating, the δ form transforms to the helical mesophase around 90°C and then to the γ form around 120°C, which then transforms to the α form around 190°C. [15, 17] On exposure to slow cooling from the melt, the β form is obtained at 250°C. The TTTT-based mesomorphic phase can directly transform to the α form on thermal annealing in the range of 120-220°C, whereas the TTGG-based mesomorphic phase first transforms to the γ form before giving the α form.[23, 24] All of these solid-solid transitions are irreversible due to the lower energy state of the TTTT conformation.

Crystalline Structures and Packing Models: Crystal Forms in Thermally-Processed sPS

Mesomorphic zigzag form. The inability of x-ray analysis to detect high amounts of crystalline phases within sPS when formed upon annealing at relatively low temperatures above the T_g, was recognized earlier and related to the formation of the mesomorphic phase associated with conformational order inside the chains (plane chain zigzag) and with paracrystalline disorder between the chains. [23] Recently, a detailed structural analysis of the mesomorphic structure was conducted by Auriemma et al. using x-ray diffraction and FTIR.[25] Results suggest the mesomorphic phase consists of ordered polystyrene chain triplets with paracrystalline disorder between the triplets, rather than randomly spaced chains with conformational order as originally hypothesized.

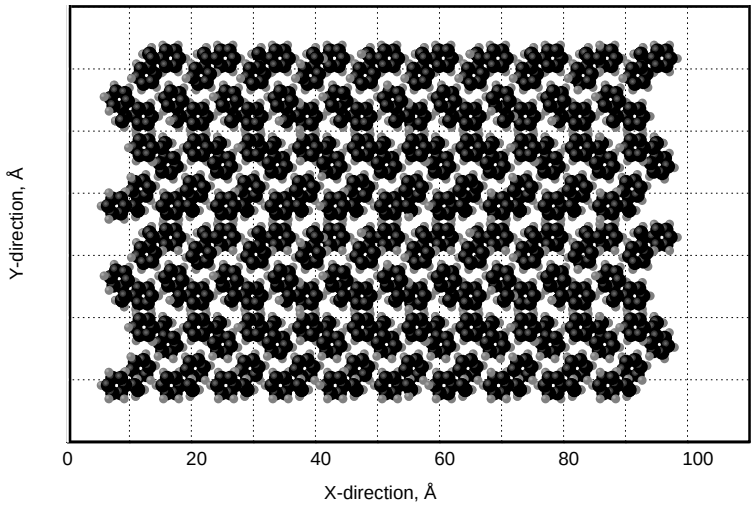

Figure 2. Scale model of the β crystalline form of sPS (carbon and hydrogen atoms are depicted in black and gray, respectively).[26]

β-Crystalline form. The all-trans-planar zigzag structure of the β crystalline form, first proposed by Chatani et al., is usual.[27] This crystalline form is characterized by orthorhombic chain packing with unit cell dimensions a=8.81Å, b=28.82Å, and c (fiber axis)=5.1Å. The crystalline density of the β crystalline form, 1.068 g/cm^3, was calculated from the parameters of the unit cell and is slightly larger than the density of amorphous sPS.[28] Figure 2 illustrates a model of the β crystalline form drawn to scale. Carbon and hydrogen atoms are drawn

approximately to the corresponding van der Waals radii. The most thermodynamically stable crystalline structure present in sPS is the β crystalline form. Therefore, it will not undergo any crystalline-crystalline transitions.

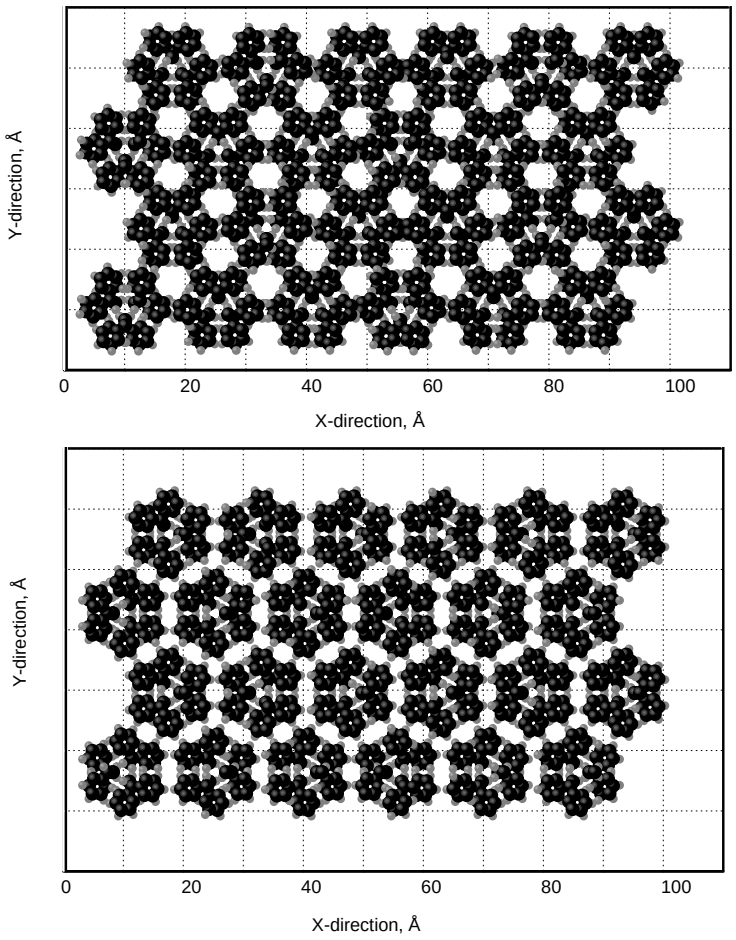

Figure 3. Scale model of α crystalline forms of s-PS: (top) proposed by Greis et al. and (bottom) proposed by De Rosa et al.[26, 29]

α-Crystalline form. The crystalline structure of the α form is unusual and has no known analogue among synthetic polymers. In particular the α crystalline form has been shown to possess a crystalline density of 1.033 g cm^{-3}, lower than the amorphous phase of 1.049 g cm^{-3}. This unique crystalline property is a result of chain arrangement. Two different modifications of the α form having different degrees of structural order have been accepted. The α structure obtained upon cold crystallization from the glassy state is known as limiting disordered

modification α′, while the α form obtained upon crystallization from the melt state is known as limiting ordered modification α″.[26] Formation of α″ over the more thermodynamically stable β is possible because α″ is kinetically favorable. The chains in the α crystalline form are first packed into clusters (triplets), each containing three chains. The backbones of these three chains make the core of the triplet while the phenyl rings point toward the periphery, this forms a "superstructure". The relative arrangement of triplets in the "superstructure" still remains a subject of controversy despite numerous efforts to resolve this puzzle. There are two main proposed packing models for the α form; trigonal and hexagonal models. In the trigonal model of the α″ structure, proposed by Greis et al. as shown in Figure 3, three triplets are included in a trigonal unit cell with the dimensions $a = b = 26.26$ Å, $c = 5.1$ Å.[29] The triplets are considered at the same height with two identically positioned triplets and one rotated by 180°. Greis et al. also proposed a one-triplet trigonal model for the α′ structure.[29] In the hexagonal model of the α″ structure as illustrated in Figure 4, De Rosa et al. proposed that the triplets have a relative shift c/3 along the *c*-axis and is rotated by 30° relative to azimuthal position of the triplets in the Greis model.[26] Limiting ordered modification, α″, according to De Rosa et al., indicates an order in the positioning of the triplets, e.g. considering any three adjacent triplets in the structure, one triplet is always oriented in one direction and the other two are rotated by 60° relative to the orientation of the first triplet. Although the orientation of one and the other two triplets are different, these two orientations are isosteric with respect to the orientation of the phenyl rings as shown in Figure 4. The phenyl rings in each triplet are oriented in the same manner despite the triplet rotation. In the limiting disordered modification, α′, the distribution of the two isosteric orientations between triplets is random.

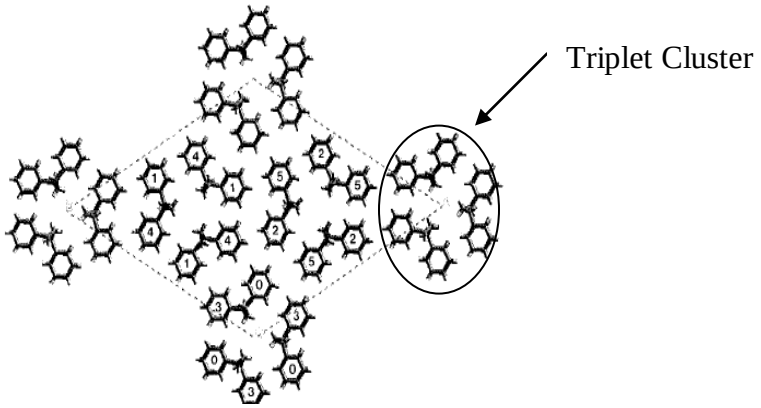

Figure 4. Schematic representation of the α″ semi crystalline s-PS triplet structure as proposed by De Rosa et al.[26]

In 1998, Lotz et al. suggested an alternative model of the frustrated crystalline structure of the α form in which the azimuthal orientations of the three triplets is different from those considered by Greis et al. and De Rosa et al.[30] In this model, the azimuthal settings and relative shifts of the triplets are such that two triplets maximize their interactions, while the third interacts less favorably with its neighbors. This model indicated the best agreement with the experimental electron diffraction pattern of the corresponding single crystal of the α form.

Despite the differences, all models of the α crystalline form predict the same density, 1.033 g/cm^3, which is smaller than the density of the amorphous phase. However, the models predict different distributions of an unoccupied space in crystalline sPS, responsible for the low density of α crystals. In the Greis et al. model, the structure exhibits wide opened channels. Six channels adjacent to the sides of each triplet, have almost a circular aperture about 5Å in diameter. In the De Rosa et al. model of the α form, the unoccupied space almost uniformly surrounds each triplet in the form of a hollow hexagonal prism with the thickness about 3-4Å. In the model proposed by Lotz et al., the distribution of unoccupied space is more complex and resembles features existing in both previously mentioned models. To circumvent these discrepancies, Nazarenko and coworkers attempted to probe the free volume of the α form through positron annihilation lifetime spectroscopy (PALS) and gas transport.[31, 32] PALS was

unable to detect changes in the free volume of the crystalline form as quantum mechanical calculations concluded that the positron lifetime in a cavity with aperture 3-5 Å and length 100 Å was similar to that of the amorphous polymer. Furthermore, diffusion models based on O_2 and CO_2 found that the low density of the α crystalline form was capable of gas transport via channeling of the gas molecules through the low density crystals, however variations in lamellar thickness and the anisotropic nature of the crystalline structure amplifies error beyond the point of confirming one packing model over another.

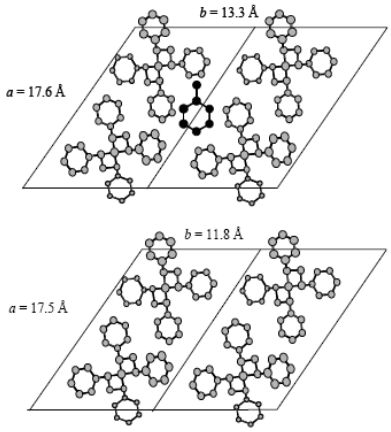

Figure 5. Model of packing, in the space group $P2_1/a$, (top) for the crystal structure of the clathrate δ form of sPS including toluene and (bottom) for the crystal structure of the emptied δ form of s-PS (δ_e form).[33]

Crystalline Structures and Packing Models: Crystal Forms in Solvent-Treated sPS

δ-Crystalline form. The δ forms of sPS demonstrate s(2/1)2 helical chains having TTGG (Figure 1) conformation with an identity period c = 7.7 Å, by means of the δ crystalline lattice encaging guest solvent molecules (clathrated δ form).[34] Discovered in 1994, the δ crystalline form was the first nanoporous polymeric crystalline phase, possessing a packing density of 0.98 g cm^{-3}.[33] A proposed model for the crystal structure of the solvent-induced δ form of sPS swelled by toluene molecules is shown in Figure 5, having the monoclinic unit cell dimensions a = 17.11 Å, b = 12.17 Å, c = 7.70 Å, and monoclinic angle γ = 120°.[35] In addition to the clathrated δ form, an emptied δ_e form can be obtained via extraction of the solvent molecules. While the packing

remains the same, the dimensions change slightly. This is achieved through the use of stepwise solvent extraction,[36-38] carbon disulfide vapor, or super-critical CO_2 extraction.[39, 40] A model for the crystal structure of the emptied δ-form (δ_e-form) of sPS is shown in Figure 5, having the unit cell dimensions a = 17.4 Å, b = 11.85 Å, c = 7.70 Å, and monoclinic angle γ= 117°, according to the space group $P2_1/a$.[41]

γ-Crystalline form. The γ form is also of a helical conformation, but the details of the crystallography and model have yet to be fully investigated.

ε-Crystalline form. Petraccone et al.[42-44] demonstrated continuous guest molecules not trapped in a clathrate but rather possessing an intercalate molecular complex. Discovered in 2007, the ε crystalline form of sPS was obtained by sorption of chloroform into the γ form followed by subsequent desorption. Wide-angle x-ray diffraction (WAXD) demonstrates an orthorhombic unit cell with dimensions a=16.1 Å, b=21.8 Å and c=7.9 Å, with four chains of sPS in the s(2/1)2 helical conformation and a density of 0.977 g cm^{-3}.[45]

Experimental

Materials

Syndiotactic polystyrene with average molecular weight, $M_w \approx 300{,}000$ g mol^{-1}, and polydispersity, $M_w/M_n \approx 2$, was supplied by the Dow Chemical Company, Midland, MI in the pellet form**.**

Amorphous syndiotactic polystyrene. Specimens in the form of 165 mm x 165 mm and 300 μm thick rectangular plaques were prepared through melt pressing of commercial pellets directly between two polished steel platens. The pellets were dried in a vacuum oven for 3 hours at 80°C prior to molding. The pellets were then taken directly from the oven, placed in a press and preheated at a mold temperature of 310°C for 15 minutes without pressure. A constant flow N_2 blanket was maintained during the initial 15 minute melting period to minimize oxidation reactions. Pressure was increased to 25,000 psi and released. This cycle was repeated three times

to ensure removal of trapped gases which may contribute to bubble formation and burn marks upon volatilization under high temperature and pressure. The plates were then held at 25,000 psi for 10 minutes followed by sequential pressure release. Finally, the plates containing sample were rapidly quenched into an ice-water mixture and dried under vacuum.

α″ Crystalline syndiotactic polystyrene. Samples containing pure α″ crystalline form with various degrees of crystallinity were prepared using isothermal crystallization from the melt. First, amorphous specimens were created in the melt press (310°C) as stated in the above process. Contrary to quenching in an ice-water bath the plates containing sample were rapidly transferred to a convection oven with a preset crystallization temperature of $T_c = 260^oC$. In the oven the samples were isothermally crystallized at different times, depending on the desired percent crystallinity. After crystallization was complete, samples were then rapidly quenched into an ice-water mixture and dried under vacuum.

An alternate method for obtaining samples containing a pure α″ crystalline form with various degrees of crystallinity was prepared via solid state transition from the γ crystalline form. The γ crystalline samples with varying degrees of crystallinity prepared with supercritical CO_2, for which the process is described later, were placed between two polished steel plates. Samples were transferred to a convection oven where the temperature was held at 210^oC for 60 minutes, in accordance with γ to α crystalline transition temperature observed during DSC scans. The plates containing the sample were rapidly quenched into an ice-water mixture and dried under vacuum.

α′ Crystalline syndiotactic polystyrene. Samples containing the α′crystalline form were prepared via cold crystallization. Amorphous samples were sandwiched between steel plates, placed in the oven and annealed using the following procedure. The temperature of the oven was slowly increased by 5^oC/min from room temperature to the final crystallization temperature ranging from 100^oC to 260^oC. Crystallization temperature determines final percent crystallinity.

The samples are kept at the final crystallization temperature for 30 minutes. After cold-crystallization, the samples are quenched in an ice-water mixture and dried under vacuum.

β Crystalline syndiotactic polystyrene. The β crystalline form was prepared in a manner similar to the preparation of the melt crystallized α″ form. The compression molding temperature was 310°C with a preheat time of 10 minutes. The convection oven for isothermal crystallization was preset to 250°C, in accordance with β crystalline transition temperature observed during DSC scans. To vary percent crystallinity, samples were isothermally crystallized at different times in the convection oven and subsequentially quenched in an ice-water mixture.

γ Crystalline syndiotactic polystyrene. Samples containing the pure γ crystalline form with various degrees of crystallinity were prepared using super-critical CO_2. Amorphous samples were placed in the extraction vessel at a temperature of 35°C and CO_2 was flushed through the system 3 times to ensure a CO_2 rich environment. CO_2 was introduced at various pressures (above 120 bar, ensuring the supercritical state of CO_2) and held for various times (up to 5 hours). These parameters were optimized to vary the degree of crystallinity. Finally, the super-critical CO_2 was extracted and the sample removed.

δ Crystalline syndiotactic polystyrene. Samples containing the clathrated δ form were prepared by soaking amorphous thin films, as confirmed through WAXD, in guest solvents for 24 hours at ambient pressure and temperature followed by drying at room temperature. Samples containing the pure δ_e form were prepared by soaking amorphous thin films in chloroform for 24 hours at ambient pressure and temperature followed by supercritical CO_2 extraction or through a crystalline-crystalline transition process. In the case of the crystalline-crystalline transition process, amorphous sample was converted to γ crystalline phase through conditioning in supercritical CO_2 at 35°C and 300 bar for 2 hrs. The sample was removed from the supercritical chamber and heated to 210°C for 1 hr followed by an ice water quench cooling, resulting in a transition to the α crystalline phase. Submerging of the sample in CS_2 for 2 hrs at 23°C allows

for conversion to the clathrated δ crystalline phase. A final solvent extraction in supercritical CO_2 at 35°C and 200 bar for 1 hr resulted in the δ_e crystalline phase.

Measurements

The crystalline structure of syndiotactic polystyrene and the amount of crystallinity was determined by WAXD measurements, conducted at room temperature with a Rigaku Ultima III X-ray spectrometer operating in reflection mode using nickel filtered CuKα radiation (wavelength 1.542 Å). Powder samples were scanned within scattering angle 2θ from 5 to 40°. PeakFit automated nonlinear peak separation and analysis software was employed to deconvolute the crystalline reflections and amorphous halo. The weight fraction of crystallinity, ω_c, was determined from the corresponding integrated areas under the crystalline reflections and the amorphous halo.

Density was measured using a density gradient column constructed from a solution of isopropanol and diethylene glycol in accordance with ASTM-D Standard 1505 Method B. It was confirmed that the selected combination of solvents does not lead to measurable swelling of sPS samples. The column was calibrated with glass floats of known density. Small film pieces (~25 mm^2) were cut and placed in the graduated column and allowed to equilibrate for 1 hr before the measurements were taken. Experimental error of density measurements did not exceed ± 0.0004 g/cm^{-3}.

Differential scanning calorimetry (DSC) was utilized to measure glass transition temperature (T_g), enthalpy of melting (ΔH_m), and enthalpy of crystallization (ΔH_{cc}). The measurements were carried out under nitrogen purge from 30°C to 320°C at a heating rate of 10°C min^{-1} using a Perkin-Elmer DSC 7. The midpoint of the corresponding C_p transition of the second scan was used to define the glass transition temperature (T_g). TA Universal Analysis was used to integrate the area under the crystalline and melting peak.

Results and Discussion

Solid State Structure of Syndiotactic Polystyrene

The crystallographic structure of α, β, γ and δ crystalline forms of sPS has been intensively studied, predominantly using WAXD.[6, 19, 26-30, 46, 47] The primary objective of this section is the characterization of syndiotactic polystyrene (sPS) solid state structure, determination of crystalline fraction, study of crystallization kinetics and nature of crystalline-crystalline transitions.

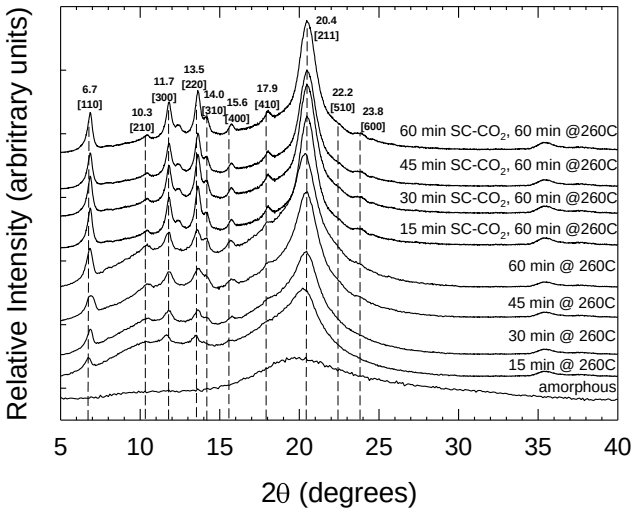

Figure 6. WAXD spectra for α″ sPS samples melt crystallized at 260°C for various times and γ to α″ crystalline-crystalline transition samples.

α" Syndiotactic polystyrene. Figure 6 shows the X-ray diffraction pattern for the α″ form sPS samples created from the melt and though the crystalline-crystalline transition from γ to α. The corresponding maximums were located at 2θ = 6.7 (110), 10.3 (210), 11.7 (300), 13.5 (220), 14.0 (310), 15.6 (400), 17.9 (410), 20.4 (211), 22.2 (510) and 23.8 degrees (600). Both isothermally crystallized and crystalline-crystalline transition from γ phase samples exhibited diffraction patterns typical of pure the α crystalline form. Specifically, peaks located at 2θ = 6.7, 11.7, 13.5, 17.9, 20.4, 22.2 and 23.8 degrees are generally assigned to the α crystalline form. Three additional characteristic peaks located at 2θ = 10.3, 14 and 15.6 degrees indicated that this

was the limiting ordered modification, α″, of the α form. Characteristic diffraction associated with the crystalline phase is more pronounced as isothermal crystallization time and supercritical CO_2 conditioning increases, demonstrating an ability to prepare samples that contain pure crystalline phase with varying crystallinity. Furthermore, a crystalline-crystalline transition process from γ to α was used to increase the overall percent crystallinity. Under isothermal melt crystallization a maximum weight percent crystallinity of 33% was obtained, however by starting with a highly crystalline γ sample it was possible to achieve a maximum crystallinity of 49.5%. Deconvolution of the aforementioned highly crystalline α″ sample is shown in figure 7 with the amorphous halo indicated. The degree of crystallinity, ω_c, was calculated using the following expression:

$$\omega_c = \frac{A_c}{A_c + A_a} \tag{2.1}$$

where A_c and A_a correspond to the integrated areas under the crystalline and amorphous domains respectively. Based on DSC results, it has been suggested that the γ to α transition proceeds through a melting and recrystallization mechanism.[6] Recently, Gowd et al. have used simultaneous measurements of SAXS/WAXD combined with infrared spectral and DSC data to propose a mechanism in which, "A large change in the stacked lamellar structure occurs in association with the unraveling of the helices into planar-zigzag form and the disordering at the boundary of crystalline and amorphous region, during which the chain orientation is kept almost perfectly".[48, 49] Despite extensive work, the true nature of this transition is still unknown. Retention of chain orientation upon recrystallization is favored by this study as it more accurately depicts increased crystallinity shown experimentally.

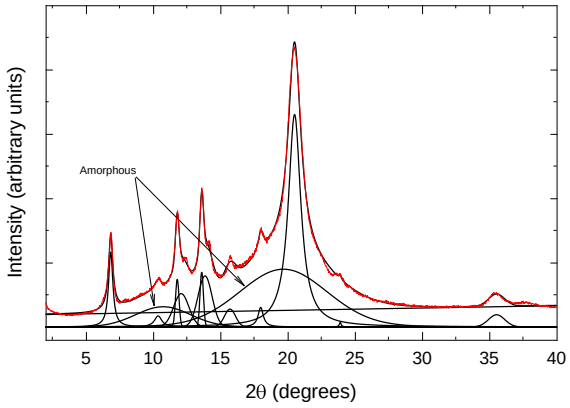

Figure 7. Deconvoluted WAXD pattern of the highly crystalline α″ form sPS obtained through a γ to α crystalline-crystalline transition approach.

α and β Crystalline heat of fusion analysis. DSC results of samples containing the α″ crystalline forms are shown in Figure 8. Amorphous samples exhibit a glass transition at about 95°C followed by a cold crystallization peak with onset at 130°C and maximum at 150°C and a melting peak with maximum at about 270°C. Samples isothermally melt crystallized at 260°C for less than 60 minutes also exhibited a cold crystallization peak. However, this peak was substantially smaller in comparison with that for the amorphous polymer. This result clearly indicates that a significant amount of amorphous material was already transformed into the crystalline phase at short annealing times. DSC scans correlate with the x-ray measurement in which the amount of the α″ crystals increases with isothermal crystallization time and supercritical CO_2 conditioning time.

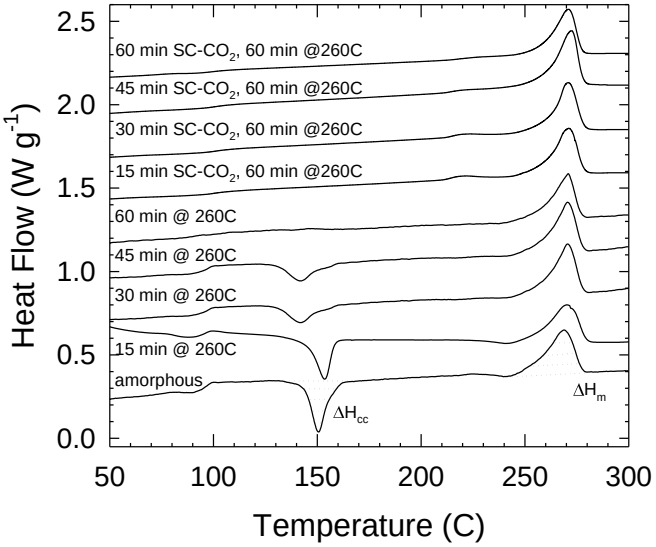

Figure 8. DSC thermograms for α″ sPS samples melt crystallized at 260°C for various times and γ to α″ crystalline-crystalline transition samples. Integrated ΔH_{cc} and ΔH_m areas for the amorphous sample are depicted as dotted lines.

Accurate measurement of DSC crystallinity is dependent upon knowing the correct value for the heat of fusion of a one hundred percent crystalline polymer. For sPS the value 53.2 J/g is generally used. This value was obtained by Pasztor et al., using extrapolation of the change in specific heat at glass transition (ΔC_p) plotted versus $\Delta H = H_m - H_{cc}$ toward zero change for a series of differently crystallized sPS, where H_m is the enthalpy of melting and H_{cc} is the enthalpy of cold crystallization.[50] The heat of fusion, ΔH, for a one hundred percent crystalline polymer, can also be determined from the density and DSC data. Figure 9 illustrates the plot of $H_m - H_{cc}$ versus density for sPS samples melt crystallized at 260°C for various times and γ to α″ crystalline-crystalline transition samples containing pure α. Also shown are melt crystallized β samples reported previously within our group. The linear regression extrapolated toward the density of pure α and β form indicates that despite a significant structural difference between the two crystalline forms, the values of the heat of fusion for a one hundred percent crystalline polymer in both forms are surprisingly similar, 56 ± 1 J/g and 52 ± 1 J/g, respectively, while the β

form exhibits good agreement with the value reported by Pasztor et al.[50] Using only melt crystallized α samples, previously reported results demonstrated a heat of fusion of 50 ± 1 J/g.

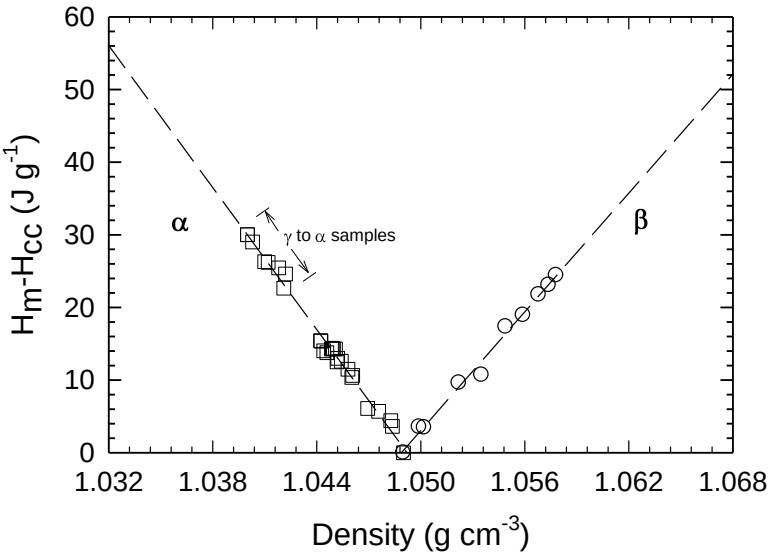

Figure 9. Heat of fusion (H_m – H_{cc}) versus density for γ to α and melt crystallized syndiotactic polystyrene samples containing pure α and β crystalline structures.

γ Syndiotactic polystyrene. The γ phase crystallization utilizes supercritical CO_2 to swell and plasticize the glassy amorphous phase. Samples display typical characteristics of the γ form, 2θ = 9.3 (200), 10.3 (020, 210), 16.0 (121), 20.0 (031, 131), and 28.3 (132) degrees.[39, 51-53] Plasticization of the amorphous phase increases the mobility of the polymer chains, allowing chains to undergo a reorientation mechanism resulting in a more ordered crystalline structure. This effect also leads to a depression of the glass transition temperature, making solid-solid transitions obtainable at reduced temperatures.

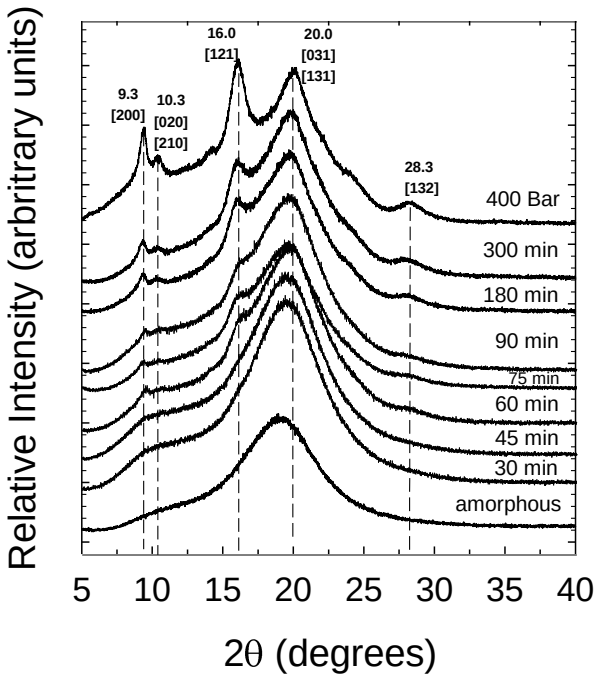

Figure 10. WAXD patterns for glassy amorphous sPS samples isothermally crystallized in supercritical CO_2 at 35°C and 120 bar for various times.

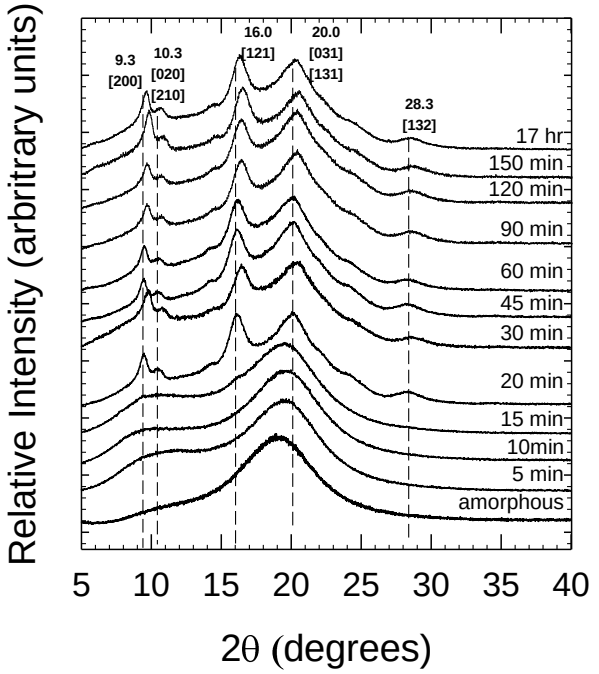

Figure 11. WAXD patterns for glassy amorphous sPS samples isothermally crystallized in supercritical CO_2 at 35°C and 200 bar for various times.

WAXD patterns for isothermally crystallized samples conditioned in supercritical CO_2 at 120°C and 200 bar are shown in Figure 10 and Figure 11, respectively. In both cases the relative crystalline fraction increases with increasing supercritical CO_2 exposure time. An example of the deconvoluted WAXD pattern for highly crystalline γ sPS is illustrated below in Figure 12. Also shown in Figure 10 is a sample prepared at 35°C with a supercritical CO_2 pressure of 400 bar for 5 hrs. This was the pressure limit of the extraction vessel and the goal was to determine the role pressure plays in the overall crystalline fraction. The sample conditioned at 400 bar possesses 10% higher crystallinity than that conditioned at 120 bar, however, there was no difference between the crystalline fraction of the sample condition at 200°C and 400 bar. This leads to the conclusion that maximum crystallinity is reached at 200 bar. At short periods, a broad peak located at 2θ = 10.0 appears upon supercritical CO_2 loading. This peak is directly associated with ordering into the helical paracrystalline mesomorphic phase.

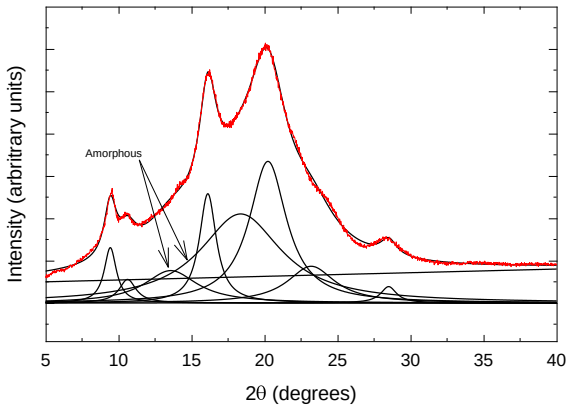

Figure 12. Deconvoluted WAXD pattern of the highly crystalline γ form sPS obtained through isothermal crystallization in supercritical CO_2 at 35°C and 200 bar.

To determine the structural effect of supercritical CO_2 loading on sPS, a separate study was conducted on two amorphous samples conditioned in supercritical CO_2 and immediately discharged under 120 and 200 bar of pressure, as shown in Figure 13. It is apparent that regardless of loading time, helical mesomorphic phase is formed. Henceforth, the presence of

mesomorphic structural order was subtracted during the deconvolution of subsequent crystallization studies when necessary.

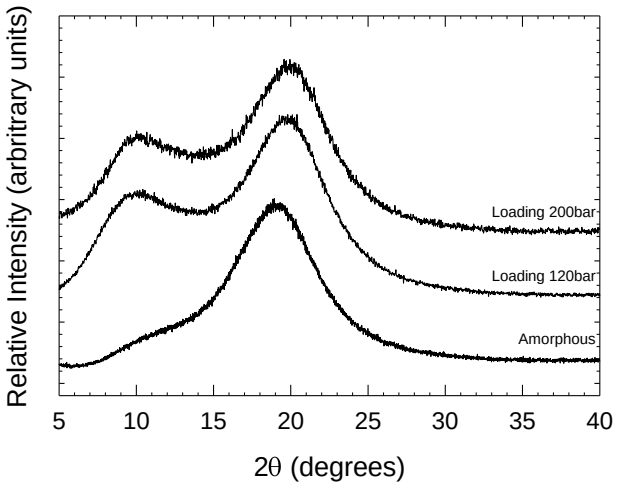

Figure 13. Isothermal loading of SC-CO_2 in amorphous sPS at 35°C and various pressures.

Supercritical CO_2 plasticization also has an effect on the isothermal crystallization kinetics shown in Figure 14 for γ sPS weight fraction crystallinity as a function of time at 35°C and various pressures, 120 and 200 bar. The observed rate of crystallization is accelerated and maximum weight fraction crystallinity, $\omega_{c\infty}$, is increased with higher pressures. The higher the pressure of supercritical CO_2, the higher the activity, thus it results in a greater effect on the increasing relaxation times of the polymer. In turn, this lowers the energy barriers responsible for solid state transitions.

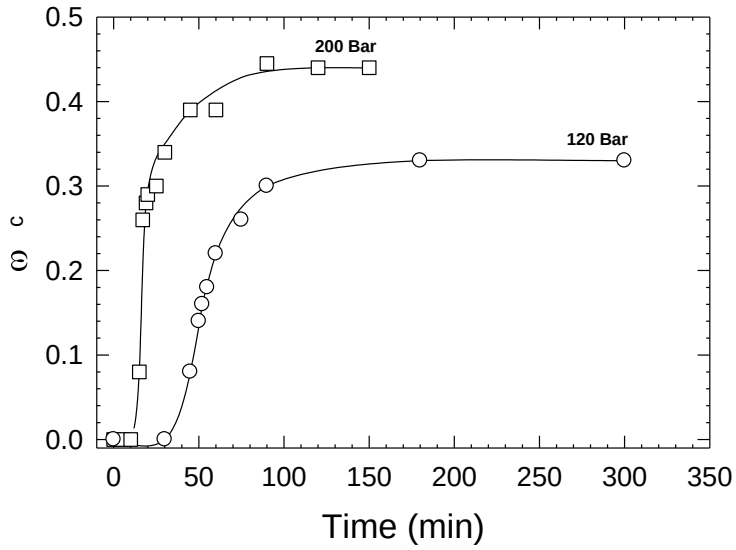

Figure 14. Crystallization isotherms of sPS at 35°C under pressures of 120 and 200 bar. Solid lines are drawn through the data points to indicate a trend.

Conversion from weight fraction to volume fraction crystallinity, easily obtained with corresponding density values, allows analysis of crystallization kinetic data. As is applicable to any type of crystallization, the kinetics were found to follow the Avrami equation:

$$1-\frac{\upsilon_c}{\upsilon_{c\infty}}=\exp(-Kt^n) \tag{2.2}$$

Where: $\upsilon_{c\infty}$ refers to volume fraction crystallinity at time infinity, υ_c is volume fraction crystallinity at time *t*, the Avrami exponent is *n* and reflects the mechanism of nucleation and crystal growth, and *K* is the kinetic rate constant for nucleation and growth. These constants are obtained through the double logarithm of equation 2.2:

$$\ln\left[-\ln\left(1-\frac{\upsilon_c}{\upsilon_{c\infty}}\right)\right]=\ln K+n\ln t \tag{2.3}$$

Avrami plots for sPS at 35°C and various pressures, 120 and 200 bar, are illustrated in Figure 15 where the values for n are reported on the graph. The tendency for the Avrami exponent to decrease with increasing supercritical CO_2 pressure is believed to be due to differences in crystal growth mechanisms. Athermal Avrami exponent values of 1.06 and 3.70

correspond to fibrillar and spherical three-dimensional nucleation and growth mechanisms, respectively.

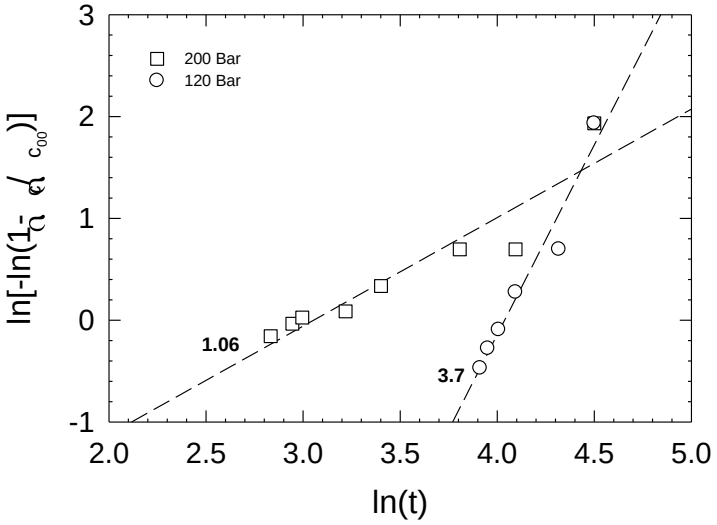

Figure 15. Avrami plots showing crystallization data at low degrees of conversion for samples conditioned in supercritical CO_2 at 35°C and various pressures.

There is an opportunity to explore the crystalline density of the γ-form of sPS for which limited data has been published. Manfredi and coworkers[18] reported a 45% crystalline sample to have a density of 1.07 g cm^{-3} utilizing molecular dynamic simulations, Tamai and Fukuda[54] proposed a density of 1.062 g cm^{-3}, and in a review by Pilla and coworkers,[55] a value of 1.08 g cm^{-3} is reported. It is apparent that a broad range of crystalline densities are extensively detailed. In an attempt to experimentally determine the density of 100% crystalline γ sPS, we chose to plot weight fraction crystallinity results obtained from WAXD with respect to density, as shown in Figure 16. It is important to note that samples were heated to 100°C for 30 min. in a vacuum oven and allowed to cool prior to density measurements. It was found that samples measured directly after supercritical CO_2 conditioning had a lower density than purely amorphous materials. The process of utilizing supercritical CO_2 is believed to swell the amorphous phase thus lowering the density. The thermal cycle slightly above the glass transition allowed the

material to relax which greatly increased measurement accuracy. Linear regression extrapolated to 100% weight fraction crystallinity indicates a pure γ form sPS density equal 1.074 g cm^{-3}.

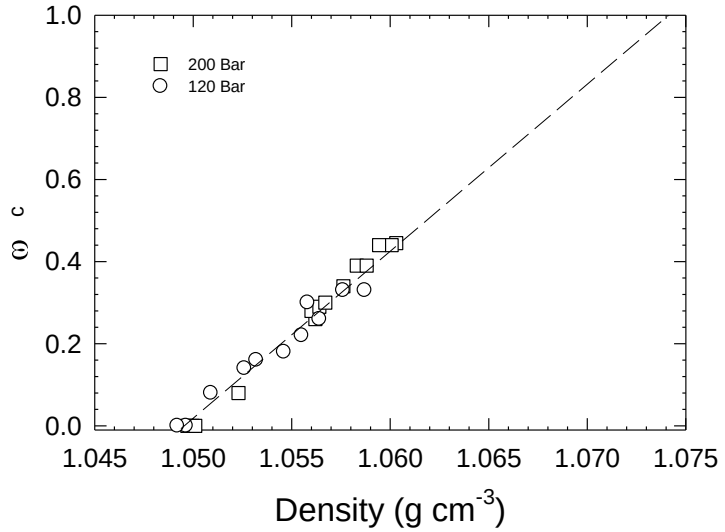

Figure 16. Weight fraction crystallinity as a function of density for samples conditioned in supercritical CO_2 at 35C for various times and pressures.

δ Syndiotactic polystyrene. Figure 17 shows the X-ray diffraction pattern for clathrated δ and δ_e form syndiotactic polystyrene samples prepared from various solvents. The corresponding peak maximums for the emptied δ_e form are located at 2θ = 8.7 (010), 11.0 (210), 13.5 (220), 17.7 (020) (111), 21.3 (311) (321), 24.2 (421), and 28.3 degrees (132). [56] Chloroform and toluene have been shown extensively to form the clathrated structure with changes in crystalline diffractions. This is indicative of changes in unit cell dimensions, the extent of which is beyond the scope of this research. [33] Chloroethyl ethyl sulfide (CEES) and dimethyl methyl phosphonate (DMMP) were chosen for scouting experiments into the viability of using nanoporous δ phase sPS for a sensing medium for chemical warfare agents, in particular sulfur mustard gas. Results indicate CEES forms clathrated δ phase while DMMP shows no sign of solvent ingress despite similar size and molecular weight. This demonstrates selectivity through preferential absorbance of the halide containing guest.

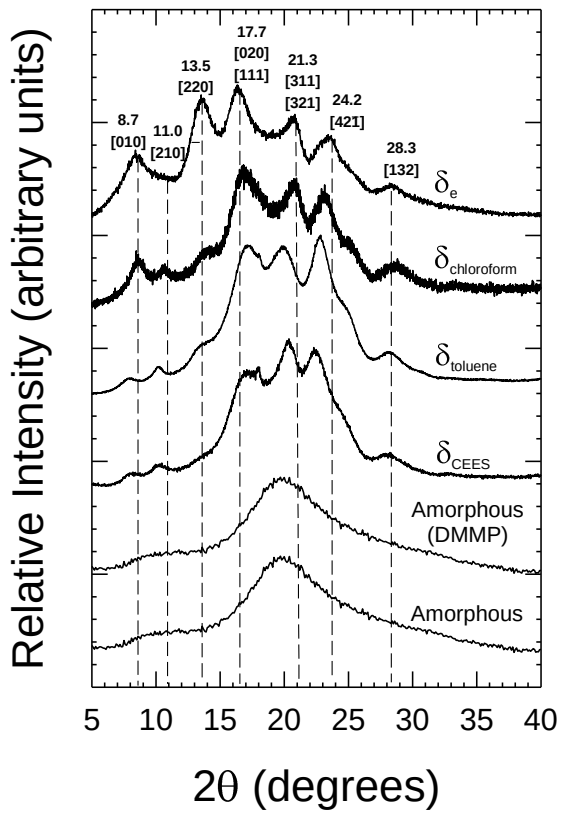

Figure 17. WAXD diffraction patterns for amorphous, clathrated δ (guest molecule indicated by subscript) and δ_e form syndiotactic polystyrene samples prepared from various solvents. The sample prepared from DMMP did not result in a clathrated structure.

The most unique characteristic property of δ_e sPS is that it has higher sorption capacity in the crystalline phase than in the amorphous phase.[57, 58] This is a consequence of the low density nanoporous crystalline phase (0.977 g cm^{-3}) with respect to that of the amorphous phase (1.049 g cm^{-3}). Other low density semi-crystalline polymers such as isotactic poly (4-methyl-1-pentane) have been found to absorb small molecule penetrants, such as CO_2 or CH_4.[59] However, these suggested molecules do not form a clathrate structure. As a result, they dissolve into the crystalline phase but to a lesser extent than that of the amorphous phase.

The absorption of small organic molecules by the nanoporous δ_e form sPS from different environments is selective and can take place at low activities.[59-62] The δ sPS crystalline phase provides an exciting opportunity for use in water or air purification, chemical separation, and

chemical sensing. However, the nature of these associations is not well understood and requires further investigation. To probe these concepts further, Chapter V examines the effect of halide electro-negativity and alkyl chain length on the sorption and diffusion of low molecular weight halogenated species, while Chapter IV examines δ_e sPS as a sensing medium in collaboration with a quartz crystal microbalance for the detection of volatile organic pollutants and chemical warfare agents.

δ_e Syndiotactic polystyrene solvent extraction. In preparing the δ_e crystalline phase difficulties arise during the removal of the guest solvent. Due to the high affinity of the guest molecule within the clathrated structure and increased segmental motions associated with the presence of the solvent, simple extraction by thermal means not only results in volatilization of the guest solvent but a crystalline phase transition to the γ form. Three primary methods for solvent removal without destroying the nanoporous structure of the host δ_e phase exist; (1) step wise solvent extraction, (2) supercritical CO_2 extraction, and (3) carbon disulfide vapor extraction. An outline of these three methods is illustrated in Figure 18.

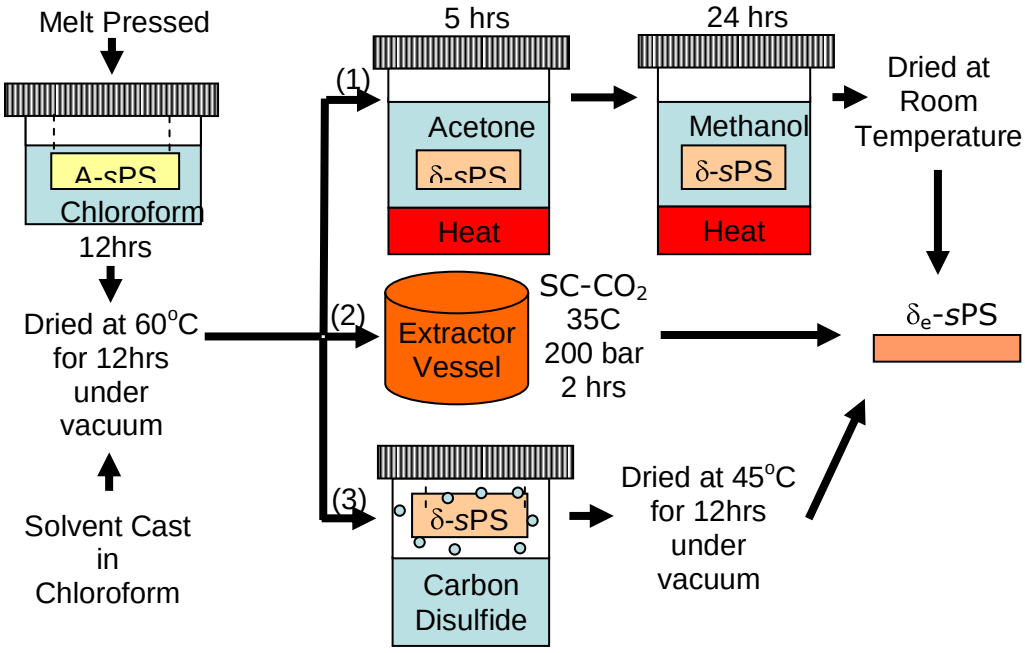

Figure 18. Experimental procedure for obtaining the δ_e crystalline form of sPS where (1) step by step, (2) supercritical CO_2, and (3) carbon disulfide solvent extraction techniques are described.

The first method, Solvent Stepwise Extraction, was undertaken by exposure of the samples to boiling acetone for 5 hours and then to boiling methanol for 24 hours, in accordance with the procedure demonstrated by Yoshimizu and coworkers.[63] Supercritical CO_2 extraction was carried out on a Dense Gas Management (DGM) system from MARC SIMS SFE supercritical fluid extractor. Samples were conditioned in supercritical CO_2 at 35°C and 200 bar for one hour. Finally, solvent replacement and subsequent extraction through the use of chemical potential differences associated with clathrated δ sPS samples placed in a CS_2 rich vapor chamber at room temperature followed by 24 hours in a vacuum oven at room temperature was employed.

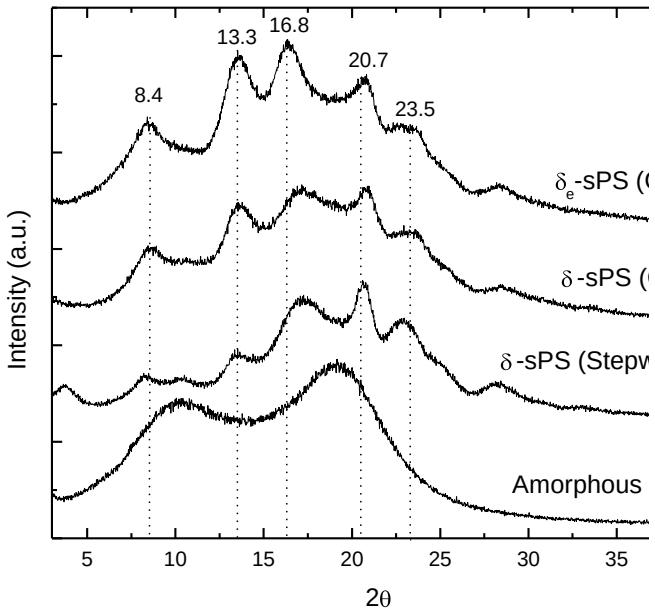

Figure 19. WAXD patterns for an amorphous sample, δ_e-sPS conditioned in supercritical CO_2, and δ_e-sPS sample conditioned in carbon disulfide.

Upon creation of the films, at the above specified conditions, wide angle X-ray diffraction and density measurements were conducted to verify crystalline form. Shown in Figure 19 are the WAXD patterns for 20μm thick samples utilizing the solvent stepwise (SSW), supercritical CO_2 (SC-CO_2) and carbon disulfide (CS_2) solvent extraction procedures. It is indicated that all processes possess the δ form in accordance with the characteristic crystalline

deflections at diffraction angles $2\theta \sim 8.4$, 10.1, 13.3, 16.8, 20.7, 23.5 and 28.3.[56] It has been reported by De Rosa et al.[41] that as the clathrated δ phase (solvent containing δ phase) is transformed to the δ_e phase (emptied δ phase), the peaks at $2\theta \sim 8.4$ and 13.3 degrees will increase while the peak at $2\theta \sim 10.1$ degrees decreases. Observations conclude samples conditioned in the supercritical CO_2 are void of chloroform, while samples conditioned in carbon disulfide and the stepwise solvent procedure contain residual solvent. Density measurements confirmed similar trends demonstrating that carbon disulfide conditioned samples have an average density of 1.041 g cm^{-3}, stepwise solvent procedure yield a density of 1.044 g cm^{-3}, and the SC-CO_2 conditioned samples yield the lowest density average of 1.002 g cm^{-3}. These results suggest that supercritical CO_2 was found to be the most efficient method for removing residual solvent in the clathrated δ phase.

Highly crystalline δ_e syndiotactic polystyrene. To increase the overall crystallinity of δ_e sPS with intentions of utilizing the crystalline phase as a sensing medium, a new method for sample preparation was proposed. This method utilized the ability to prepare high degrees of γ phase crystallinity through supercritical CO_2, to generate highly δ_e crystalline samples via crystalline-crystalline solid state transitions. Such high degrees of crystallinity were previously unobtainable. Preparation was carried out as detailed in the experimental section.

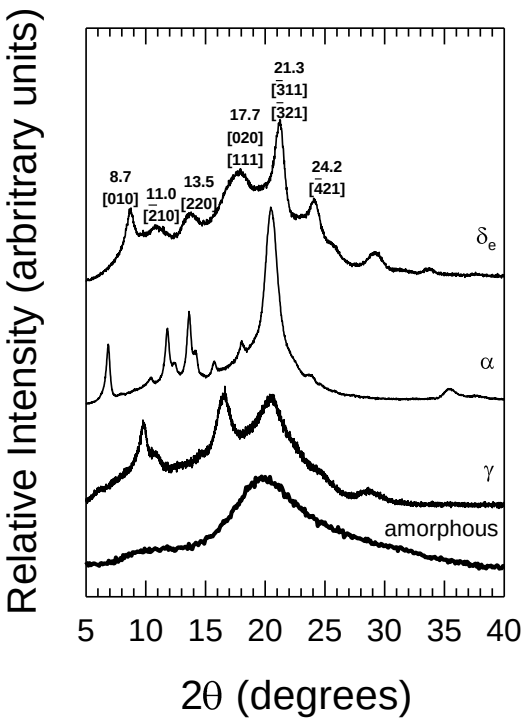

Figure 20. WAXD patterns for crystalline-crystalline transitions of syndiotactic polystyrene used to create δ_e sPS.

Figure 20 corresponds to WAXD patterns for the various crystalline forms of sPS used to create δ_e phase sPS samples. Figure 21 corresponds to the deconvoluted WAXD pattern of δ_e sPS. These data demonstrate high degrees of crystallinity at 42 wt% δ_e phase obtained via solid state crystalline transitions. Such high degrees of crystallinity could not be obtained through direct formation of the α and δ forms. Presumably, the presence of the previously formed crystallite acts to assist the nucleation process through introducing surfaces suitable in development of the lattice structure of the stable phase. It has been shown that by increasing the nanoporous crystalline fraction we can obtain sensors of amplified sensitivity.

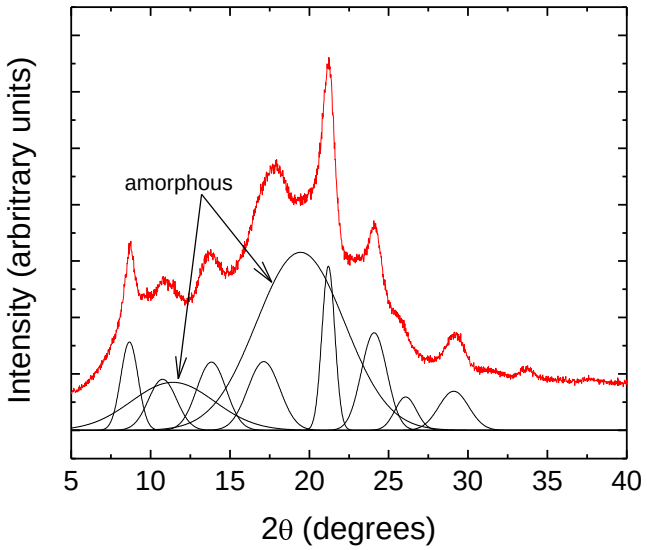

Figure 21. Deconvoluted WAXD pattern of the highly crystalline δ_e form sPS obtained through crystalline-crystalline transitions ($\gamma-\alpha-\delta-\delta_e$).

Conclusions

Characterization of syndiotactic polystyrene (sPS) solid state structure, determination of the crystalline fraction, study of crystallization kinetics and nature of crystalline-crystalline transitions was reported. Wide angle X-ray diffraction patterns of α, β, γ, δ and the mesomorphic phases demonstrate homogeneous structure. Heat of fusion for 100% α and β crystalline sPS, 56 and 52 ± 1 J g^{-1}, respectively, is obtained though extrapolation of $\Delta H = H_m - H_{cc}$ with respect to density for a series of melt-crystallized and crystalline-crystalline manipulated samples. Weight fraction crystallinity versus density linear regression demonstrates 100% γ form crystalline density to be 1.074 g cm^{-3}. Isothermal crystallization kinetics of γ phase sPS with respect to pressure is detailed. Efficiency of step wise, carbon disulfide and supercritical CO_2 solvent extraction methods for removal of trapped solvents within the clathrated δ form of sPS were examined with supercritical CO_2 yielding the most thorough extraction. Results indicate CEES forms a clathrated δ phase while DMMP shows no sign of solvent ingress despite similar size and molecular weight, demonstrating selectivity through preferential absorbance of the halide containing guest.

References

1. Ishihara, N.; Kuramoto, M.; Uoi, M. *Macromolecules* **1986,** *19*, 2464.

2. Ishihara, N.; Kuramoto, M.; Uoi, M. *Macromolecules* **1988,** *21*, 3356.

3. Po, R.; Cardi, N. *Prog. Polym. Sci.* **1996,** *21*, 47.

4. Pellecchia, C.; Long, P.; Proto, A.; Zambelli, A. *Makromol. Chem. Rapid Commun.* **1992,** *13*, 265.

5. Yang, M.; Cha, C.; Shen, Z. *Polym. Journal* **1990,** *22*, 919.

6. Guerra, G.; Vitagliano, V. M.; De Rosa, C.; Petraccone, V.; Corradini, P. *Macromolecules* **1990,** *23*, 1539.

7. Rizzo, P.; Daniel, C.; De Girolamo Del Mauro, A.; Guerra, G. *Chem. Mat.* **2007,** *19*, 3864.

8. Vittoria, V.; Russo, R.; De Candia, F. *J. Macromol. Sci., Phys.* **1989,** *B28*, 419.

9. Immirzi, A.; de Candian, F.; Iannelli, P.; Vittoria, V.; Zambelli, A. *Makromol. Chem. Rapid Commun.* **1988,** *9*, 761.

10. Vittoria, V.; De Candia, F.; Iannelli, P.; Zambelli, A. *Makromol. Chem. Rapid Commun.* **1988,** *9*, (765).

11. Vittoria, V.; Russo, R.; De Candia, F. *Polymer* **1991,** *32*, 3371.

12. De Candia, F.; Guadagno, L.; Vittoria, V. *Makromol. Chem. Rapid Commun.* **1995,** *B34*, 95.

13. Grassi, A.; Longo, P.; Guerra, G. *Makromol. Chem. Rapid Commun.* **1989,** *10*, 687.

14. Kobayashi, Y.; Nakaoki, T.; Ishihara, N. *Macromolecules* **1989,** *22*, 4377.

15. Reynolds, N. M.; Stidham, H. D.; Hsu, S. L. *Macromolecules* **1991,** *24*, 3662.

16. Savage, J. D.; Wang, Y. K.; Stidham, H. D.; Corbett, M.; Hsu, S. L. *Macromolecules* **1992,** *25*, 3164.

17. Wang, Y. K.; Savage, J. D.; Yang, D.; Hsu, S. L. *Macromolecules* **1992,** *25*, 3659.

18. Manfredi, C.; De Rosa, C.; Guerra, G.; Rapacciuolo, M.; Auriemma, F.; Corradini, P. *Macromol. Chem. Phys.* **1995,** *196*, 2795.

19. De Rosa, C.; Rapacciuolo, M.; Guerra, G.; Petraccone, V.; Corradini, P. *Polymer* **1992,** *33*, 1423.

20. De Candia, F.; Carotenuto, M.; Guadagno, L.; Vittoria, V. *J. Macromol. Sci., Phys.* **1996,** *B35*, 265.

21. De Candia, F.; Filho, A. R.; Vittoria, V. *Macromol. Chem., Rapid Commun.* **1991,** *12*, 295.

22. Doherty, D. C.; JHopfinger, A. J. *Macromolecules* **1989,** *22*, 2472.

23. De Candia, F.; Filho, A. R.; Vittoria, V. *Colloid. Polym. Sci.* **1991,** *269*, 650.

24. De Candia, F.; Guadagno, L.; Vittoria, V. *J. Macromol. Sci., Phys.* **1995,** *B34*, 95.

25. Auriemma, F.; Petraccone, V.; Dal Poggetto, F.; De Rosa, C.; Guerra, G.; Manfredi, C.; Corradini, P. *Macromolecules* **1993,** *26*, 3772.

26. De Rosa, C.; Guerra, G.; Petraccone, V.; Corradini, P. *Polym. Journal* **1991,** *23*, 1435.

27. Chatani, Y.; Fujii, Y.; Shimane, Y.; Ijitsu, T. *Polym. Prep. Jpn. (Eng. Ed.)* **1988,** *37*, E428.

28. Sun, Z.; Morgan, R. J.; Lewis, D. N. *Polymer* **1992,** *33*, 661.

29. Greis, O.; Xu, Y.; Asano, T.; Petermann, J. *Polymer* **1989,** *30*, 590.

30. Cartier, L.; Okihara, T.; Lotz, B. *Macromolecules* **1998,** *31*, 3303.

31. Hodge, K.; Prodpran, T.; Shenogina, N. B.; Nazarenko, S. *J. Polym. Sci., Part B: Polym. Phys.* **2001,** *39*, 2519-2538.

32. Olson, B. G.; Prodpran, T.; Jamieson, A. M.; Nazarenko, S. *Polymer* **2002,** *43*, 6775-6784.

33. Guerra, G.; Manfredi, C.; Rapacciuolo, M.; Corradini, P.; Mensitieri, G.; Del Nobile, M. A. Italy, IT1228915, **1994**.

34. Rizzo, P.; Lamberti, M.; Albunia, A.; Ruiz, O.; Guerra, G. *Macromolecules* **2002,** *35*, 5854-5860.

35. Guerra, G.; Milano, V.; Venditto, P.; Musto, C.; De Rosa, C.; Cavallo, L. *Chem. Mater.* **2000,** *12*, 363.

36. Amutha Rani, D.; Yammamoto, Y.; Mohri, S.; Sivakumar, M.; Tsujita, Y.; Yoshimizu, H. *J. Polym. Sci., Part B* **2002,** *41*, 269-273.

37. Amutha Rani, D.; Yamaki, B. S.; Mohri, S.; Sivakumar, M.; Tsujita, Y.; Toshimizu, H. *J. Polym. Sci., Part B: Polym. Phys.* **2003,** *41*, 269.

38. Mahesh, K.; Sivakumar, M.; Yamamoto, Y.; Tsujita, Y.; Yoshimizu, H.; Okamoto, S. *J. Polym. Sci., Part B* **2002,** *41*, 269-273.

39. Ma, W.; Yu, J.; He, J. *Macromolecules* **2004,** *37*, 6912-6917.

40. Reverchon, E.; Guerra, G.; Venditto, P. *J. App. Polym. Sci.* **1999,** *74*, 2077-2082.

41. De Rosa, C.; Guerra, G.; Petraccone, V.; Pirozzi, B. *Macromolecules* **1997,** *30*, 4147-4152.

42. De Giraolamo Del Mauro, A.; Carotenuto, M.; Venditto, P.; Petraccone, V.; Scoponi, M.; Guerra, G. **2007,** *19*,6041.

43. Petraccone, V.; Tarallo, O.; Venditto, P.; Guerra, G. *Macromolecules* **2005,** *38*, 6965-6971.

44. Tarallo, O.; Petraccone, V.; Venditto, P.; Guerra, G. *Polymer* **2006,** *47*, 2402.

45. Petraccone, V.; Ruiz de Ballesteros, O.; Tarallo, O.; Rizzo, P.; Guerra, G. *Chem. Mat.* **2008,** *20*, 3663-3668.

46. Chatani, Y.; Shimane, Y.; Ijitsu, T.; Yukinari, T. *Polymer* **1993,** *34*, 1625.

47. De Rosa, C. *Macromolecules* **1996,** *29*, 8640.

48. Gowd, E. B.; Shibayama, N.; Tashiro, K. *Macromolecules* **2007,** *40*, 6291.

49. Gowd, E. B.; Shibayama, N.; Tashiro, K. *Macromolecules* **2008,** *41*, 2541.

50. Pasztor Jr., A. J.; Landes, B. G.; Karjala, P. *Thermochim. Acta.* **1991,** *177*, 187.

51. Handa, Y. P.; Zhang, Z.; Wong, B. *Macromolecules* **1997,** *30*, 8499.

52. Rizzo, P.; Albunia, A.; Guerra, G. *Polymer* **2005,** *46*, 9549-9554.

53. Sun, Y. S.; Woo, E. M.; Wu, M. C.; Ho, R. M. *Polymer* **2003,** *44*, 5293.

54. Tamai, Y.; Fukuda, M. *Macromol. Rapid Commun.* **2002,** *23*, 892.

55. Pilla, P.; Cusano, A.; Cutolo, A.; Giordano, M.; Mensitieri, G.; Rizzo, P.; Sanguigno, L.; Venditto, P.; Guerra, G. *Sensors* **2009,** *9*, 9816.

56. Rizzo, P.; Mensitieri, G.; Di Maio, L. *Macromol. Symp.* **2002,** *185*, 65.

57. Musto, P.; Mensitieri, G.; Cotugno, S.; Guerra, G.; Venditto, V. *Macromolcules* **2002,** *35*, 2296.

58. Tarallo, O.; Petraccone, V. *Macromolcules* **2004,** *205*, 1351.

59. Puleo, A. C.; Paul, D. R.; Wong, P. K. *Polymer* **1989,** *30*, 1357.

60. Guerra, G.; Manderkern, L.; Musto, C.; Tavone, S. *Macromolecules* **1998,** *31*, 1329.

61. Manfredi, C.; Del Nobile, M. A.; Mensitieri, G.; Guerra, G.; Rapacciuolo, M. *Polym. Sci., Polym. Phys.* **1997,** *35*, 133.

62. Musto, P.; Manzari, M.; Guerra, G. *Macromolecules* **1999,** *32*, 2770.

63. Amutha Rani, D.; Yamamoto, Y.; Mohri, S.; Sivakumar, M.; Tsujita, Y.; Yoshimizu, H. *J. Polym. Sci., Part B* **2002,** *41*, 269-273.

CHAPTER III

DEVELOPMENT OF A MASS SPECTROMETER-BASED DYNAMIC GAS PERMEATION SYSTEM: TRANSPORT CHARACTERISTICS OF *SYNDIOTACTIC* POLYSTYRENE

Introduction

Gas Transport Measurement

Understanding the gas permeation through a polymeric membrane is of great importance both academically and industrially and has been approached by numerous methods.[1, 2] One in particular, known as the dynamic differential approach, has been widely used since 1970. [3] In this method, a test gas is introduced into the upstream side of a polymer membrane at time $t = 0$. A constant carrier gas flows through the downstream side and transfers the permeated test gas to the sensor. The diffusion flux, $J(t)$, can then be determined from the concentration of the test gas present in the carrier gas, $c(t)$, and volume flow rate of carrier gas, $\dot{V}$ in the following equation:

$$J(t) = c(t)\dot{V} \tag{3.1}$$

A typical experimental curve consists of non-steady and steady state parts, from which diffusivity and permeability coefficients can be determined, respectively. It is assumed that the concentration of test gas in the downstream is small compared to the concentration of carrier gas, while the carrier gas flow rate is fast enough to neglect the adsorption of test gas on the walls. The concentration of upstream permeant may be adjusted over a wide range by varying pressures and any analytical technique may be used to determine the concentrations of single permeant or permeant mixtures in the downstream effluent. Numerous publications have described the advantages of this approach over the constant volume variable pressure approach. [4-7] The test apparatus based on this principle has been commercialized by Infotronics Co. and then developed successfully by MOCON, Inc.

There are some limitations to utilizing carrier gas in this dynamic differential approach. Carrier gas with flow rates of 1-50 cc min^{-1} is typically used to avoid adsorption of the test gas on

tubing walls. Too high a flow rate will lower the sensitivity of the signal since the concentration of test gas in the carrier gas will become too small to be determined by the sensor. Sensitivity cannot be simply increased by decreasing the carrier gas flow rate, as permeant may diffuse through the membrane back upstream, and the carrier gas may also diffuse to the upstream and dilute test gas. If the flow rate of carrier gas is to be changed only slightly, one may see from equation 4.1 that the sensitivity of the permeation flux determination is defined mainly by the sensitivity of the sensor selected to measure the low concentration of test gas in the carrier gas.

The mass-spectrometer (MS) is able to detect very small amounts of gas molecules to give the compositions of the test gases and to have short response times. It is because of this sensitivity that MS can be used for gas permeation measurements and has been documented in the following literature. Eustache et al.[8] estimated the permeability of oxygen and carbon dioxide through thick rigid PVC, based on the proportionality between pressure and flow rate through a fixed leak. Mapes et al.[9-11] estimated the steady-state gas flow rate by determining the relationship between the conductance through the orifice plate and ion gauge pressure within the MS chamber for the test gas. With known volume of the upstream chamber and area of the polymer membrane, Nörenberg et al.[12, 13] calculated steady-state permeation rates by measuring the exponentially decreasing pressure within the MS chamber connected to downstream side of the membrane. In all of the above noted works, only the steady-state gas permeation flux was measured while the diffusion and solubility coefficients were not determined. Ward and coworkers employed the basic principles of the dynamic differential approach to measure permeability, diffusion and solubility coefficients using MS.[14] In this process, the downstream side of the permeation cell was connected directly to both a diffusion pump and MS through which the concentration of permeant in the downstream was measured. The permeation flux rate can be obtained based on the linear relationship between the response of the MS and a reference input pressure. Watson et al.[15] developed a so-called continuous-flow vacuum permeation cell

using MS to evaluate the water transport properties of poly(dimethylsiloxane). Utilizing characteristic time, which is the time for permeation flux to rise from the initial to final steady-state level, they determined the diffusion coefficient. However, it was difficult to accurately define this characteristic time since the change of permeation flux was not sharp but smooth. Moreover, the original water content existing in the system was not easily extracted; this directly affected the accuracy of the water permeation measurement.

Despite the advantages of MS detection, including the high sensitivity to near all gases along with the ability to measure multi-component permeation, the method was never widely adopted because of the high price of the instrument. With the current availability of small and inexpensive quadrupole-type MS, the use for gas permeation measurements will be increased. This will allow for the improvement of experimental procedures and data treatment, which has been determined as insufficient within past literature.

In the present work, the advantages of the dynamic techniques developed in the past for industrial applications will be utilized in our MS-detection apparatus for effective measurements of gas permeability along with diffusion and solubility coefficients. No carrier gas will be applied in our permeation apparatus. Instead, a powerful turbomolecular pumping system will be responsible for establishing a rapid equilibrium concentration of permeant in the downstream that is proportional to the permeant flux across the polymer membrane at any time. The permeation apparatus will have the capacity to measure the permeability and diffusivity coefficient of any gas and gas mixture (up to 300 atomic mass units) through a polymer membrane.

Gas Separation Membranes

The concept of membrane separation was originally proposed by Graham in 1866, when he used a natural rubber polymer to increase oxygen concentrations in atmospheric air.[16] It was poor performance that delayed commercialization until 1977 when Monsanto and Perma introduced their hydrogen recovery system.[17] Membrane performance is directly proportional to

two key characteristics - permeability and selectivity. Permeability represents the flux of a specific gas through the membrane, while selectivity represents the preference for a membrane to permeate one gas species and not another. The best gas separation membranes possess high permeability and high selectivity toward a specific gas penetrant. Molecular sieving and solution diffusion are the main mechanisms for nearly all gas separating membranes. In particular, molecular sieves are a unique class of materials that have molecularly-sized uniform pores or channels and can effectively discriminate between molecules on the basis of size and shape. This allows diffusion of smaller gases at a much faster rate than larger gas molecules.

A novel approach to materials containing uniform nanochannels or nanopores with an aperture diameter less than 10 Å has been discussed within the literature. Such materials can function as "molecular size reaction vessels" to carry out chemical processes, serve as hosts for the fabrication of novel electronic materials or can be employed as molecular sieves. Mineral nanoporous structures, known as zeolites, have become crucially important materials for numerous technical processes and are the synthesis basis for a gallery of inorganic molecular sieves.[18] Design of novel molecular sieves with unconnected channels is currently a key research and development target in this area, given that they will enable higher permeant fluxes in shape selective permeation. The drawbacks of mineral nanoporous molecular sieves are high capital cost, brittleness and limited options for the processing of large-scale membranes.[19] Conversely, polymeric molecular sieves would offer low cost, toughness, material variability and versatility of processing methods. Polymer rubbers are highly permeable for gas molecules due to ineffective packing and the high mobility of polymer chains, but exhibit poor selectivity. Glassy polymers also exhibit reasonably high permeability due to ineffective packing of polymeric chains upon vitrification, but molecular size gaps between adjacent chains in the glassy amorphous state are not uniform and this seriously compromises the selectivity of polymeric glasses for use as molecular sieves. Nevertheless, many glassy polymers find application as gas separation membranes, primarily because polymers are inexpensive and mechanically robust at moderate

temperatures.[20, 21] Polymer crystals provide uniformly packed chains, however, the gaps between chains are usually too small to allow passage of even small gas molecules. The density of polymer crystals (ρ_c) typically exceeds the density of the amorphous phase by 10-15%, and polymer crystals are considered virtually impermeable for gas transport.[22] It is this reason that semicrystalline polymers are generally not used for gas separations.

It has recently been recognized that several polymers including syndiotactic polystyrene, syndiotactic poly-p-methyl styrene, isotactic poly(4-methyl-pentene 1) and possibly several others exhibit an unusually low density crystalline phase, which is smaller than the density of the amorphous phase. Low crystalline density is associated with the substantial, molecular size openings (4-6 Å) existing between the polymer chains in the crystalline structure. The uniformity of these inter-chain gaps makes these semicrystalline polymers very interesting materials for molecular sieving applications. In 1989, Puleo et al. confirmed unusual gas transport behavior for semicrystalline isotactic poly(4-methyl-pentene 1) (P4MP1).[23] The crystalline phase of P4MP1 was found to be highly permeable for small molecules. Nazarenko et al. have discovered that the crystalline structure of syndiotactic polystyrene is also highly permeable for small molecules such as oxygen and carbon dioxide.[24] This is the foundation upon which the current research of gas transport behavior in semicrystalline syndiotactic polystyrene (sPS) is based.

Experimental

Materials

Amorphous syndiotactic polystyrene. Syndiotactic polystyrene (Questa 102), Mw≈300,000 g/mol and Mw/Mn≈2, was purchased from Dow Chemical Co. in pellet form. Amorphous samples of 165 mm x 165 mm and 400 μm thick were prepared by compression molding. The pellets were placed between two polished steel platens at 315°C, and 23,000 psi for 15 minutes, then quenched into an ice-water mixture.

Semicrystalline syndiotactic polystyrene containing α″ form. Samples containing pure α″ crystalline form with various degrees of crystallinity were prepared using isothermal crystallization from the melt. First, amorphous specimens were created in the melt press (310°C) as stated in the above process. Contrary to quenching in an ice-water bath, the plates containing sample were rapidly transferred to a convection oven with a preset crystallization temperature T_c = 260°C. In the oven, the samples were isothermally crystallized for different times, depending on the desired percent crystallinity. After crystallization was completed, samples were rapidly quenched into ice-water mixture and then dried under vacuum. An alternate method for obtaining samples containing pure α″ crystalline form with high degrees of crystallinity were prepared via solid state transition from the γ crystalline form. Amorphous samples were placed in a CO_2 extraction vessel at a temperature of 35°C. Carbon dioxide was flushed trough the system 3 times to ensure a CO_2 rich environment. Carbon dioxide was introduced at 200 bar pressure (ensuring the supercritical state of CO_2) and held for 2 hours. Super-critical CO_2 was extracted and the now γ form sPS removed. The γ crystalline samples were placed between two polished steel plates and transferred to a convection oven where temperature was held at 210°C for 60 minutes, in accordance with gamma to alpha crystalline transition temperature as observed during DSC scans. Ultimately, the plates containing sample were rapidly quenched into an ice-water mixture and dried under vacuum.

Calibration films. National Institute of Standards and Technology (NIST) traceable standard for oxygen transmission rate calibrated film (O_2TR=0.00996 cc/pkg/day at 23°C and 0% RH) was purchased from MOCON, Inc. Poly(ethylene terephthalate) (PET), was purchased from Mitsubishi Polyester Film, LLC in pellet form. The amorphous PET films of 200 μm thickness were prepared by compression molding at 290°C under 23,000 psi pressure and then being quenched into ice-water.

High purity test gases. The test gases were purchased from Nordan Smith Inc. and the purity of all gases was greater than 99.9%. The carrier gases used in MOCON OX-TRAN 2/21 units are the mixture of 98% nitrogen and 2% hydrogen. All permeation measurements in DGPS-MS and OX-TRAN 2/21 units were performed at room temperature and 1 atmosphere pressure.

Measurements

Wide angle X-ray diffraction. The crystalline structure and amount of crystallinity were determined by wide-angle X-ray diffraction (WAXD). WAXD measurements were conducted at room temperature with a Rigaku Ultima III X-ray spectrometer operating in reflection mode using nickel filtered CuKα radiation (wavelength 1.542 Å). Powder samples were scanned within scattering angle 2θ from 5 to 40°. PeakFit automated nonlinear peak separation and analysis software was employed to deconvolute the crystalline reflections and amorphous halo. Weight fraction of crystallinity, ω_c, was determined using Ruland method from the corresponding integrated areas under the crystalline reflections and the amorphous halo.

MOCON OX-TRAN. Oxygen flux, *J(t)* at 25°C and 0% of relative humidity was measured using MOCON OX-TRAN® 2/21 commercially built diffusion apparatus. This instrument employs continuous flow cell method (ASTM D3885-81) using nitrogen as a carrier gas. Oxygen partial pressure 1 atm across the film thickness was maintained. The temperature during permeation measurements was controlled within ± 0.5°C. All samples were preconditioned in a vacuum desiccator at least for 24 hours and rapidly transferred to the test cell to minimize humidity exposure. Permeability and diffusion coefficient were obtained by performing a two parametric least square fit of the experimental flux data to the solution of Fick's second law:

$$J(t) = \frac{Pp}{l}\left[1 + 2\sum_{n=1}^{\infty}(-1)^n \exp(-D\pi^2 n^2 t / l^2)\right] \tag{3.2}$$

Where: P is the permeability coefficient, D is the diffusion coefficient, l is the specimen thickness which was determined by micrometer, and p is oxygen partial pressure difference across the film. The solubility S was obtained from the relationship $P=DS$.

Dynamic gas permeation system using mass-spectrometer. A schematic of the dynamic gas permeation system using mass-spectrometer (DGPS-MS) is shown below in Figure 22. The polymeric test membrane was placed in a custom built temperature controlled high-pressure filter holder (a detailed drawing file is provided at the end of this chapter). The temperature during permeation measurements was controlled within ± 0.2^{o}C, via a circulating chiller. A calibrated NIST certified polymer membrane was placed in the calibration cell of identical design. The upstream, test gas side of the sample cell consists of a Fisher maxima C plus roughing pump, test gas inlet and Omega Engineering PX181-300G5V pressure transducer. The downstream side of the sample membrane is connected through a valve to the gas inlet of the quadrupole mass-spectrometer to monitor sample conditioning and diffusion test. Between the sample cells and the gas inlet of the mass-spectrometer is a MKS 226A differential pressure transducer (DPT) connected to a controlled high vacuum low pressure volume, which is used for constant volume variable pressure and calibration measurements. The quadrupole mass-spectrometer, modular mass selective detection system, was purchased from Ferran Scientific Incorporated.

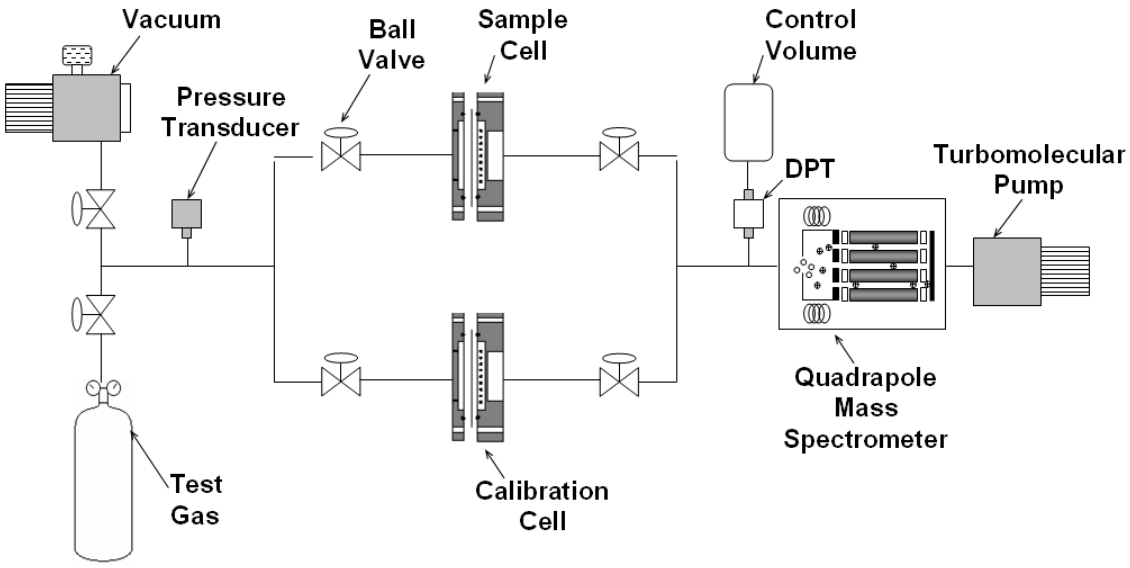

Figure 22. Schematic of a custom-made dynamic gas permeation system using mass-spectrometer (DGPS-MS).

The mass spectrometer acts as an atomic mass filter using the principles used for quadrupoles, the theory of operation for DGPS-MS is as follows. First, a filament injects electrons at a specific velocity into an ion chamber. Molecules that have permeated through the test film now passing through this stream of electrons may have one or more electrons stripped off. These molecules, now positively charged ions, are accelerated to the bottom of the ion chamber and injected onto the center of four parallel rods by voltage "lenses". A large radio frequency AC signal and a specific DC voltage are applied to the parallel rods to "tune" the MPA for ions with specific mass and charge. The combination of the two voltages gives the positive ions with specific mass-to-charge ratio stable trajectories allowing them to reach the collector. All other ions have unstable trajectories leading them to crash into the rods and are therefore lost. The Spectra Converter then counts the ions that make it to the collector. The signal is further processed by the computer network interface for output to the computer. The MS system is pumped by a vacuum system driven by a Varian V70 turbomolecular pump with dry backing pump. The working gas inlet pressure was around 0.07 Pa. The gas molecules of from 2 to 300

atomic mass units (AMU) can be monitored on eight separate channels at the same time, and for each selected AMU the area counts, which are proportional to the partial pressure, can be monitored as well. Therefore, up to eight different kinds of gases can be introduced to the permeation system and be monitored simultaneously.

Consider at the time, *t*, the flux of permeant, *i*, through the polymer membrane is $J_i(t)$. Assuming that there is no leak in the system and the turbomolecular pump is ideal (no return flux), the differential equation describing the mass balance for the permeant *i* in the system is:

$$\frac{V dp_i(t)}{dt} = -S_i p_i(t) + J_i(t) \tag{3.3}$$

Where: S_i is volumetric pumping speed and $p_i(t)$ is partial pressure for the given permeant *i*. At steady state, $\frac{dp_i(t)}{dt} = 0$ and equation 4.3 can be expressed by:

$$J_i(t) = S_i p_i(t) \tag{3.4}$$

The size of the ionization chamber of the quadrupole MS, *V*, is about 0.1 liter. It is evacuated by a turbomolecular pump system with pumping speed S = 70 liter s^{-1}. Therefore, the equilibrium concentration of the permeant *i* will be established very rapidly, $\tau_i = V/S_i \approx 0.001$ s. Typically it will take about one minute to scan the full mass range up to 300 AMU. The scanning time can be reduced to several seconds if only several specified atomic masses need to be monitored. Compared with the scanning speed of MS, τ_i is so small that the measured equilibrium $p_i(t)$ is proportional to the permeation flux $J_i(t)$ at every moment. The short response time is an advantage of MS detection in comparison with the coulometric sensor in MOCON OX-TRAN 2/20 unit, which requires several minutes to reach the equilibrium.

For different gases, the pumping speed may be altered. Therefore, an accurate calibration of the instrument is required. Such calibration was performed using commercially available

NIST standard calibrated film with known constant flow rate J_i^* from 1 atmosphere to the vacuum. According to equation 3.4, S_i can be obtained by:

$$S_i = J_i^* / p_i^* \tag{3.5}$$

Where p_i^* is the partial pressure of the permeant *i* through the calibrated film, while the permeation flux $J_i(t)$ can be expressed by:

$$J_i(t) = (J_i^* / p_i^*) p_i(t) \tag{3.6}$$

The sensitivity of the instruments can be varied in a very wide range by changing the pumping speed S_i. The commercially available conductance controllers can be utilized to change pumping speed in four orders of magnitude. Even without the change of S_i, the instrument is capable of measuring the change of gas flux in six orders of magnitude (from 10^{-1} to 10^5 cc (STP) m^{-2} day^{-1} atm^{-1}). With addition of the conductance controller, this instrument will cover the whole range of permeation measurements starting from rubbers (the permeability *P* in the range of $10^2 - 10^4$ barrers) to semi-crystalline polymers (*P* in the range of $10^{-3} - 10^{-5}$ barrers) for different kinds of gases and gas mixtures.

A constant volume variable pressure method is also employed as an added measurement capability and calibration for various homogeneous gases. This method is well established in the literature.[25, 26] The experimental plot provided below in Figure 23 exhibits a well-defined steady-state slope typical of Fickian behavior, and is representative of all measurements. Slope of the linear regression, *dp/dt*, was used to calculate permeability, *P*, according to:

$$P = \frac{V_d l}{pART}\left(\frac{dp}{dt}\right) \tag{3.7}$$

Where V_d is the downstream volume, l is the membrane thickness, p is the applied upstream pressure, A is the testing area, R is the universal gas constant, and T is the temperature. A time-lag approach was used to calculate diffusion coefficient, D, according to:

$$D = \frac{l^2}{6t_L} \tag{3.8}$$

Where time lag, t_L, is equal to the steady state linear regression extrapolated to zero pressure. The specimen is weighed and the area carefully measured. The average thickness is calculated as $l = W/A\rho$ where W is the sample weight, A is the sample area, and ρ is the density. The density of each sample was measured with the gradient column with typical error 0.001 g/cm^3 (less then 0.1 % of sample density). The accuracy of sample thickness measurements was within 1 % error, giving an accuracy of better than 3% for permeability and better than 5% for the diffusion coefficient.

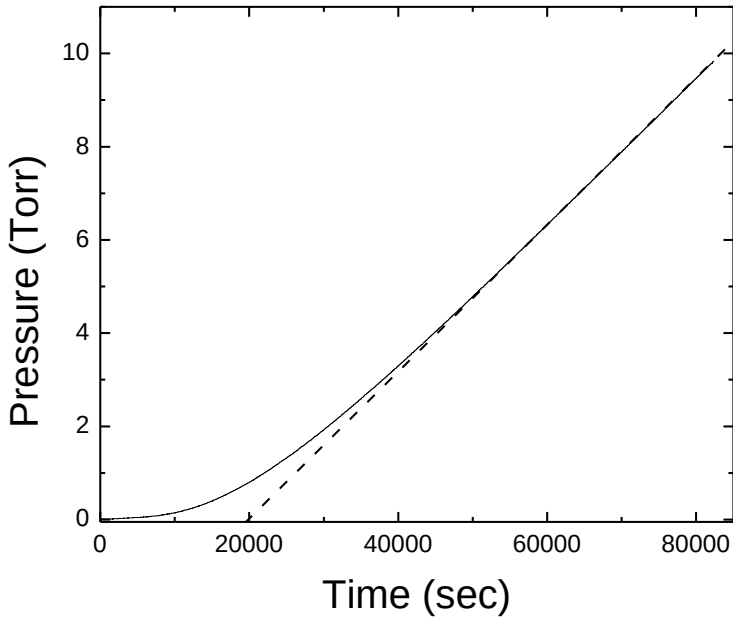

Figure 23. Representative constant volume variable pressure curve for oxygen flux through amorphous syndiotactic polystyrene at 25C. Dotted line indicates extrapolation of the steady state portion demonstrating the time-intercept, used to calculate time lag, t_L.

Results and Discussion

DGPS-MS Qualification

A typical experimental curve from DGPS-MS is illustrated in Figure 24. Both sides of the sample and calibrated membranes were conditioned under vacuum until all the permeants initially absorbed in the samples have fully desorbed. A stable equilibrium baseline signal was obtained when the partial pressure reported by MS approached background contributed from the system. Test gas at one atmosphere pressure was introduced to the calibrated NIST control with the sample cell closed and the calibration procedure started. The partial pressure during this calibration period, subtracted from system background, gave the partial pressure contributed by the permeant *i* through the calibrated membrane p_i^*. Once partial pressure equilibrium was reached due to the constant flow of test gas through the calibrated membrane, the upstream side of sample membrane was opened to the feed system to start the permeation test until a final steady state was reached.

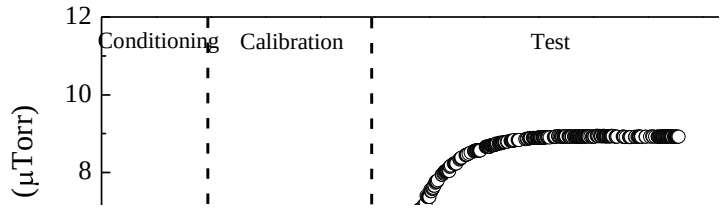

Figure 24. A typical experimental curve obtained from DGPS-MS.

The test section of the experimental curve shown in Figure 24 is similar to the oxygen flux curve obtained from MOCON OX-TRAN 2/21 unit, consisting of a non-steady state region,

determined mainly by the diffusivity D_i and a steady state region. The steady state value of the partial pressure P_i^{∞} can be converted to permeation flux J_i^{∞} according to equation 3.6. This flux value, normalized by the film thickness l and the partial pressure of the permeant p_i at the upstream side of the sample membrane during the test, defines the permeability P_i:

$$P_i = J_i^{\infty} l / p_i \tag{3.9}$$

The diffusivity D and permeability P can be obtained by fitting the data to the solution of Fick's second law with appropriate boundary conditions:

$$J(t) = \frac{Pp}{l}\left[1 + 2\sum_{n=1}^{\infty}(-1)^n \exp(-D\pi^2 n^2 t / l^2)\right] \tag{3.10}$$

The equation above works well for long diffusion time, while only the first term in the expansion is needed for $t > \frac{l^2}{3.9631D}$. However, for those with very fast diffusion conducted in DGPS-MS, equation 3.10 cannot give a good fit for the experimental data. An alternative equation is given as the following:

$$J(t) = \frac{2Pp}{\sqrt{\pi Dt}}\sum_{n=1}^{\infty}\exp[-(2n-1)^2 l^2/(4Dt)] \tag{3.11}$$

Only the first term in the expansion is needed for $t \le \frac{l^2}{3.9631D}$. Finally we use the following expression to fit the experimental curves:

$$J(t) = \begin{cases} \dfrac{2Pp_i}{\sqrt{\pi Dt}}\exp\left(-\dfrac{l^2}{4Dt}\right), & t \le \dfrac{l^2}{3.9631D} \\ \dfrac{Pp_i}{l}\left[1 - 2\exp\left(-\dfrac{D\pi^2 t}{l^2}\right)\right], & t > \dfrac{l^2}{3.9631D} \end{cases} \tag{3.12}$$

The solubility *S* is obtained from the relationship *P=DS*. The fitting curves are included in all figures with the experimental data points and the qualities of the fits are excellent.

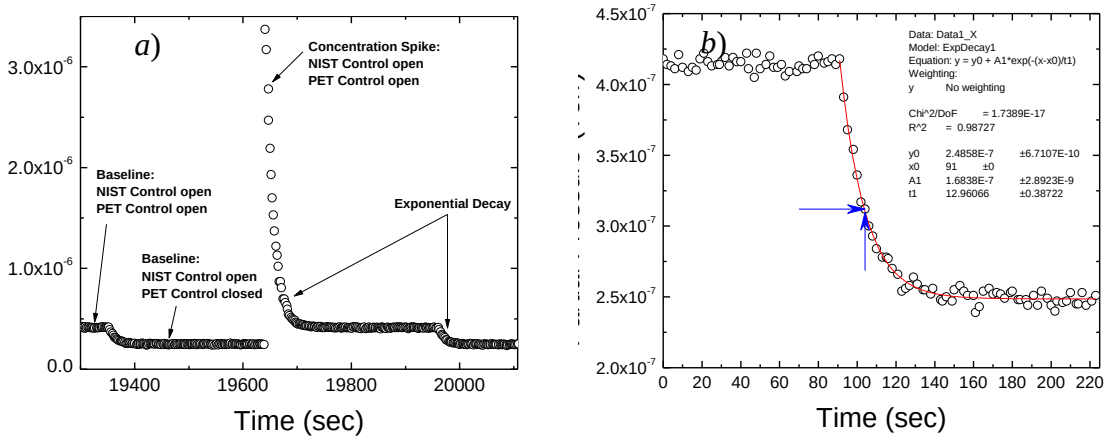

Figure 25. Instrumental characteristic response for instantaneous gas loading and unloading; *a*) experimental representation of the test method and *b*) representative nonlinear fit according to the experimental decay relation.

Instrumental characteristic response time may be obtained by determining the time it takes for the system to respond to instantaneous gas loading and unloading. Response time was determined using NIST and PET control films at 25°C and 1 atm pressure for multiple gases. The method is depicted experimentally in Figure 25*a*. The measurement begins as NIST and PET controls, pressurized with test gas in the upstream, are opened directly to the MS detector. Upon closing of the valve located between the PET sample and the MS, an exponential decay is observed, representing instantaneous test gas unloading. Concurrent with this decay, test gas concentration increases between the PET sample and the downstream valve. Upon opening of the downstream valve a concentration spike is observed, indicative of instantaneous test gas loading. The decay of these two processes may be related to the characteristic response according to the following equation:

$$p_i = A\exp^{-\left(\frac{t-t_o}{\tau}\right)} \tag{3.13}$$

Where: t_o is the initial time of the experiment, p_i is partial pressure of the test gas, A is a constant, and τ is the characteristic response time. A representative nonlinear fit according to the above experimental decay relation is shown in Figure 25*b*. Measurements were repeated 10 times for multiple gases with characteristic response time equal to 13.10±0.70 and 14.37±0.49 seconds for baseline shift and concentration spike method, respectively. This system shows greater than one order of magnitude faster response than that characteristic of commercial OX-TRAN measurements (approximately 10 minutes).

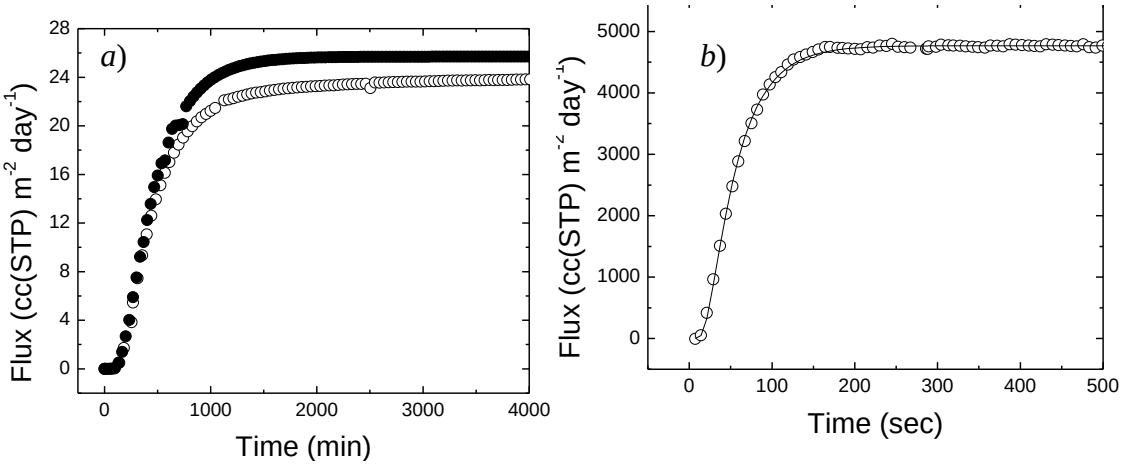

Figure 26. Comparison of *a*) measured oxygen flux through melt pressed 200 μm PET between from DGPS-MS (●) and from MOCON OX-TRAN 2/21 (○) and *b*) measured He Flux through melt pressed 200 μm PET from DGPS-MS.

Figure 26*a* shows a comparison of DGPS-MS and MOCON OX-TRAN 2/21 measured oxygen flux curves for a melt pressed PET film. The permeability and diffusion coefficients of O_2 measured from DGPS-MS indicates good agreement with those obtained from OX-TRAN 2/21 and are comparable with constant volume variable pressure. As expected, DGPS-MS was able to measure the relative slow diffusion of O_2. For the very fast diffusion of He, DGPS-MS acquired enough data points to well define the non-steady state region of the permeation, as demonstrated in Figure 26*b*. This shows the capability of DGPS-MS to run the diffusion test for various gases, from slow to very fast diffusion.

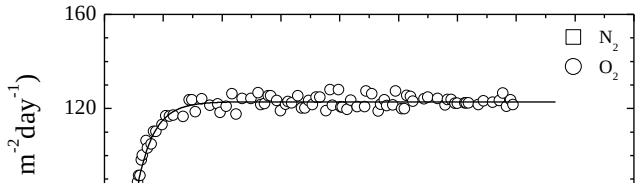

Figure 27. Experimental permeation curves of air through 12 μm PET-24CT measured by DGPS-MS.

Shown in Figure 27 for an air gas mixture, the simultaneous diffusion of N_2 and O_2, the two major components in the air, were recorded by DGPS-MS. The obtained permeability and diffusion coefficients of N_2 and O_2 from the air indicated similar results as to those obtained from pure gas diffusion tests. This result was produced because the diffusion of gas components would not be affected by each other in the mixture at such low pressure, which contributes to a lack of competitive transport.

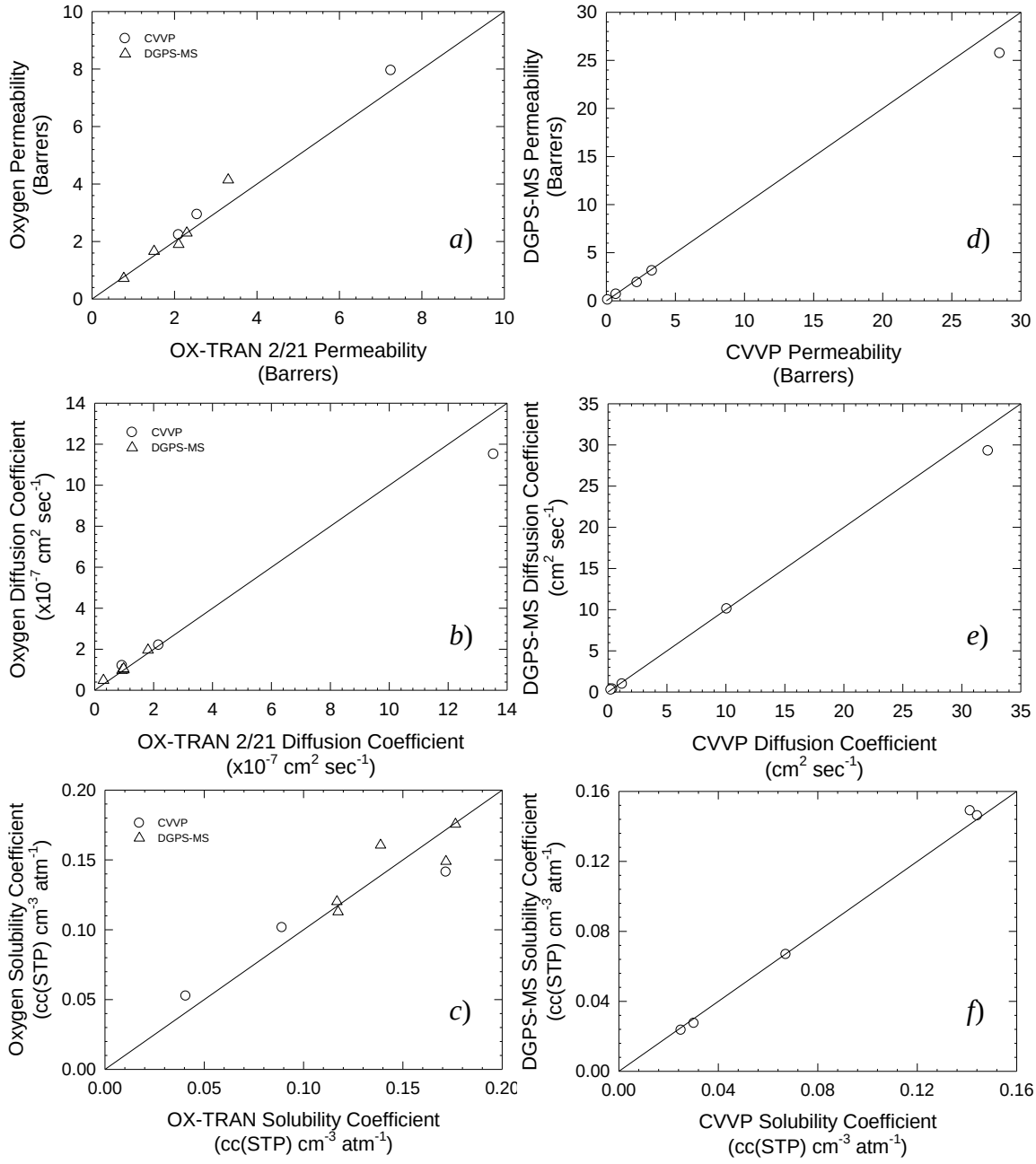

Figure 28. Comparison profiles of constant volume variable pressure (CVVP), dynamic gas permeation system with mass spectrometer (DGPS-MS), and MOCON OX-TRAN 2/21 measurement techniques. Solid lines represent an ideal relationship. Correlations of oxygen permeability, diffusion coefficient, and solubility coefficient are shown in *a*, *b* and *c*, respectively. Correlation between CVVP and DGPS-MS for various gases as it relates to permeability, diffusion coefficient, and solubility coefficient are shown in *d*, *e* and *f*, respectively.

All samples considered in this study were plotted with respect to the three measurement techniques to demonstrate experimental confidence as shown in Figure 28*a-f*. Graphical

representation of permeability, diffusion coefficient and solubility coefficients show good correlation.

Gas Transport in Syndiotactic Polystyrene

Constant volume variable pressure measurements for various gases through amorphous and semicrystalline α" syndiotactic polystyrene samples are shown in Figure 29. All measurements were fit with equal confidence to extract permeability, diffusion and solubility values with the exception of diffusion and solubility coefficients for helium though 42% α" syndiotactic polystyrene. When a sample thickness was increased, diffusion was too fast to be accurately reported by CVVP techniques. It was observed for a given sample that a relative decrease in slope accompanies changes in gas permeant indicates a decrease in permeability with increasing permeant size.

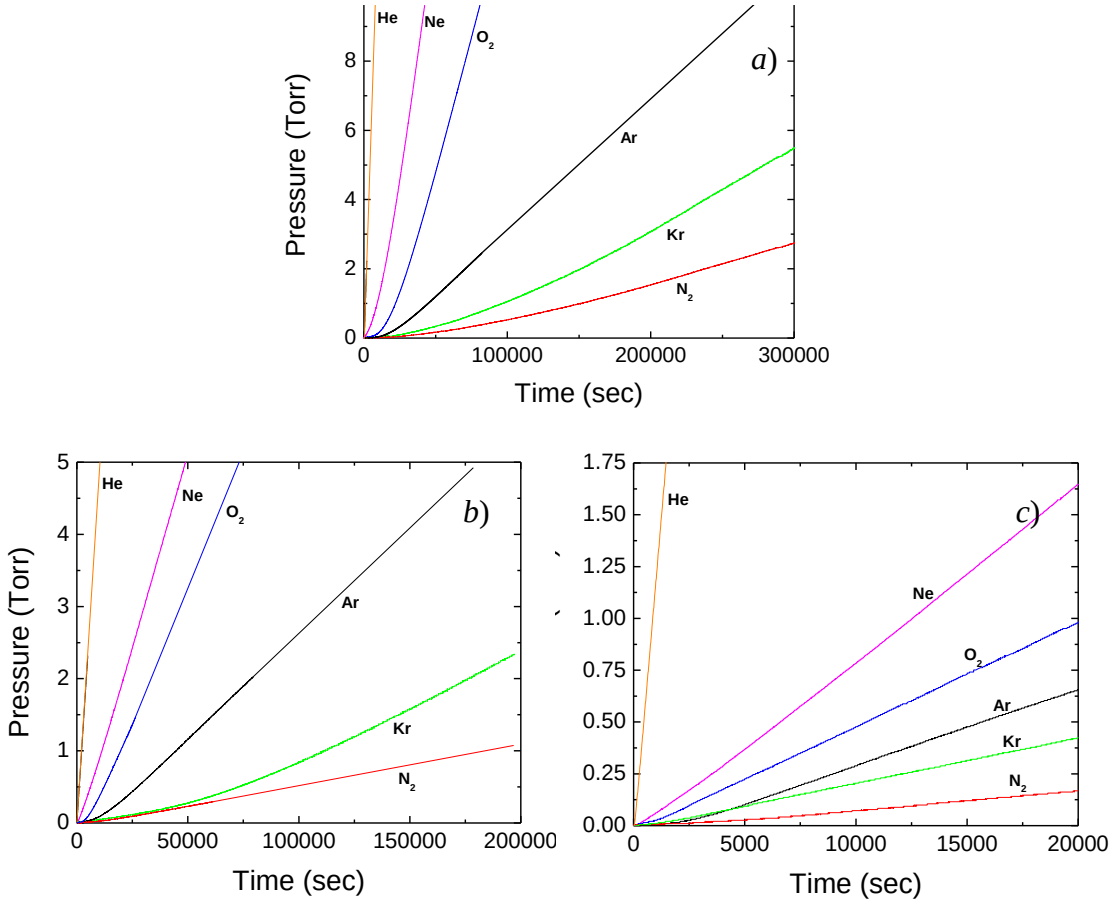

Figure 29. Constant volume variable pressure measurements for various gases through *a*) amorphous, *b*) 11% α", and *c*) 42% α" syndiotactic polystyrene at 25°C.

Previous results in our group considering experimental permeation curves of He, Ne, Ar and CH_4 through amorphous sPS, semicrystalline sPS containing 28% α" form and semicrystalline sPS containing 32% β form (ca. 400 μm thick) are shown in Figure 29*a-d*, respectively. These results were obtained on an earlier permutation of the DGPS-MS in which a calibrated leak was used in place of the NIST calibrated film. Lack of temperature control, gas leaks and constant difficulties associated with clogging of the calibrated leak has driven the evolution of the original test method. These results demonstrate excellent agreement with amorphous and α samples recently obtained and are shown to demonstrate the effect of β phase crystallinity not explored in the current work.

a) *b*)

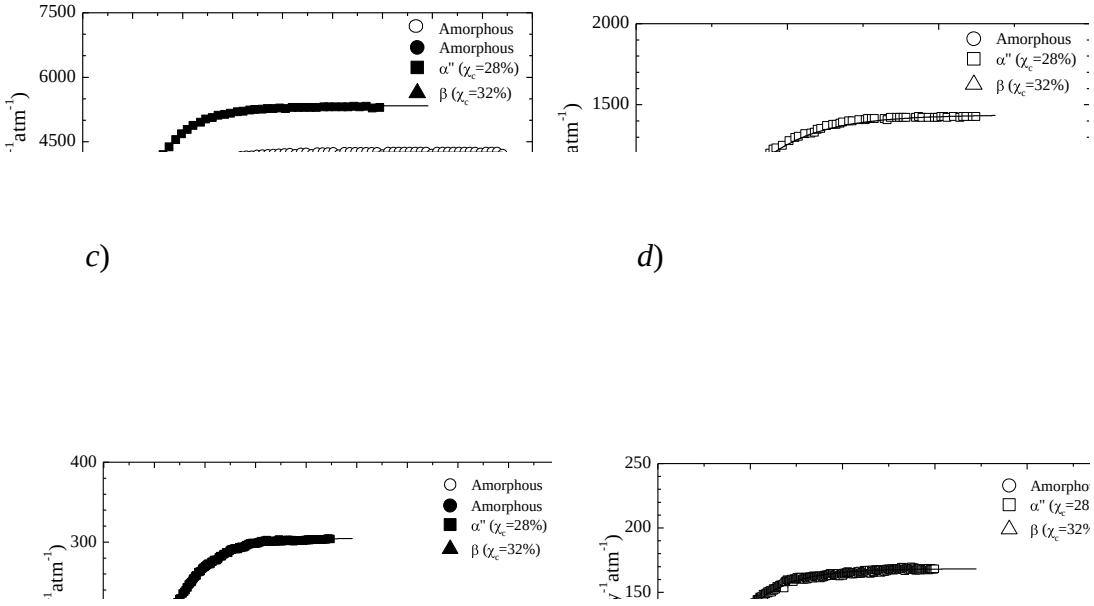

c) *d*)

Figure 30. Experimental Flux curves of *a*) He, *b*) Ne, *c*) Ar and *d*) CH_4 through amorphous, α" and β crystalline s-PS measured by DGPS-MS previously obtained in our lab.

It can be seen that the time to reach the equilibrium of permeation process ranges from a few minutes to a couple of days, depending on the permeants. The non-steady state region, associated with the progress of the concentration profile across the thickness of the film, was easily detected even when using Helium as the permeant. The fits for all the experimental data were equally good indicating that a very wide range of gas permeation through a polymer membrane can be successfully measured by DGPS-MS. In all cases the β sample shows the lowest permeability and diffusion coefficient. The β crystalline form follows typical diffusion rates of semicrystalline polymers in which the crystalline phase is impermeable to the penetrant gases. An effect which becomes more pronounced as the kinetic diameter of the inert permeant gas increases. If we account for crystallinity according to a simple two phase model in which the

relationship for permeability is rewritten as $P=\upsilon_a^2 DS$, where υ_a is the volume fraction of the amorphous phase, the amorphous fraction transport characteristics are accurately extracted.

The diffusion coefficient, *D*, in polymers usually decreases with increasing cross-sectional molecular diameter of the penetrant. It has been shown that the dependence of diffusion coefficient as it relates to molecular diameter for many low molecular weight gases is optimally expressed by:

$$LogD = K_1 - K_2 d_{ef}^2 \tag{3.14}$$

Where: K_1 and K_2 are constants dependent upon the polymer of interest and d_{ef} refers to the effective molecular diameter as obtained by comparing the diffusion coefficients of various gases in different polymers and kinetic diameter.[27] Figure 31 demonstrates the room temperature semi logarithmic dependence of diffusivity on d_{ef}^2 for several gases and polymers including amorphous, 11% α" and 42% α" syndiotactic polystyrene. There is a strong correlation between molecular size and separation properties in strongly size-sieving polymers where penetrant solubility is minimal. It is also observed that the size-sieving properties may be related to the relative slopes of various polymers. Additionally, it is apparent that the sieving properties of syndiotactic polystyrene possessing the low density α" crystalline phase change with increased crystalline fraction.

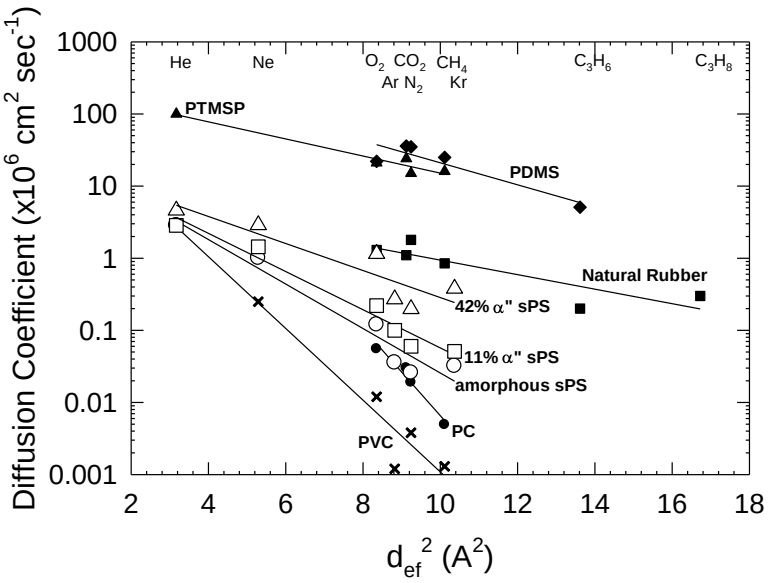

Figure 31. Room temperature semi-logarithmic dependence of diffusivity on d_{ef}^2 for several gases and polymers, poly(1-trimethylsilyl-1-propyne) (PTMSP),[28] poly dimethyl siloxane (PDMS),[29] natural rubber,[30] polycarbonate (PC),[30] polyvinyl chloride (PVC),[30] and amorphous, 11% α" and 42% α" syndiotactic polystyrene (sPS).

For a broad range of polymers, specifically various carbon chain length penetrants for which classical approaches break down with increased size, the use of effective molecular diameter was preferred. Kinetic diameter is perhaps more accurate when concerning mono- and di- atomic light gases (H_2, He, N_2, O_2, Ne, etc.). The diffusion rate for several gases in various semicrystalline syndiotactic forms are shown in Figure 32, as a function of probe kinetic diameter. Also indicated in Figure 32 are the diffusion rates determined from simulation of 100% crystalline α" form sPS with helium, neon, and argon permeants.

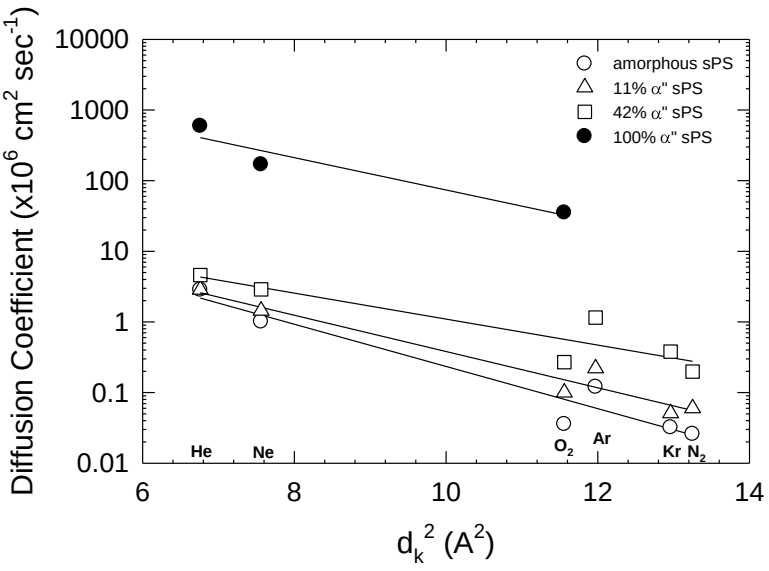

Figure 32. Room temperature semi-logarithmic dependence of diffusivity on d_k^2 for several gases in amorphous and semicrystalline α" syndiotactic polystyrene.

From Figure 30, it is observed that the diffusion rates in both amorphous and semicrystalline sPS containing the β form are remarkably similar. However, for semicrystalline sPS containing the α" form, the diffusion rate was slightly larger than that for the amorphous sample. This effect becomes progressively more prominent with increasing crystallinity. In addition, as the permeant kinetic diameter increases, the difference between amorphous and α" form sPS amplifies. This behavior is also evident from the simulation work of Tamai et al.[31] The molecular dynamics simulation work of Tamai et al. further explored how the diffusion rate parallel, $D_{\|}$, and perpendicular, $D_{\perp}$ to the sPS chain axis varies with crystal form and permeant size. They found that for the β form, $D_{\|}$ and $D_{\perp}$ were essentially the same at each permeant size studied. However, for the α" form, $D_{\|}$ and $D_{\perp}$ were nearly equal for He due to the small permeant size, but differed as the permeant size increased. Simulation showed that the $D_{\perp}$ was zero for Ne and Ar. This was attributed to a transition from a nearly 3-dimensional behavior for small permeant size to a 1-dimensional behavior for larger permeant sizes. Larger permeants are confined to the hexagonally shaped nanochannels between the triplets in the α" form, and cannot

move between parallel channels. The smaller permeants, however, can move relatively freely between neighboring channels, resulting in a more 3-dimensional diffusion behavior. The activation energy for channeling was calculated to be rather small (~7 kJ/mol for Ar). This 1-dimensional behavior resulting from the nanochannels in the α" form was first proposed by Hodge et al.[24] from analysis of oxygen and carbon dioxide permeability measurements, and further corroborated by positron annihilation measurements.[32] Despite large diffusivity in the α" form, molecular dynamics simulations and experimental results showed gas solubility was comparable to that in the amorphous sPS.

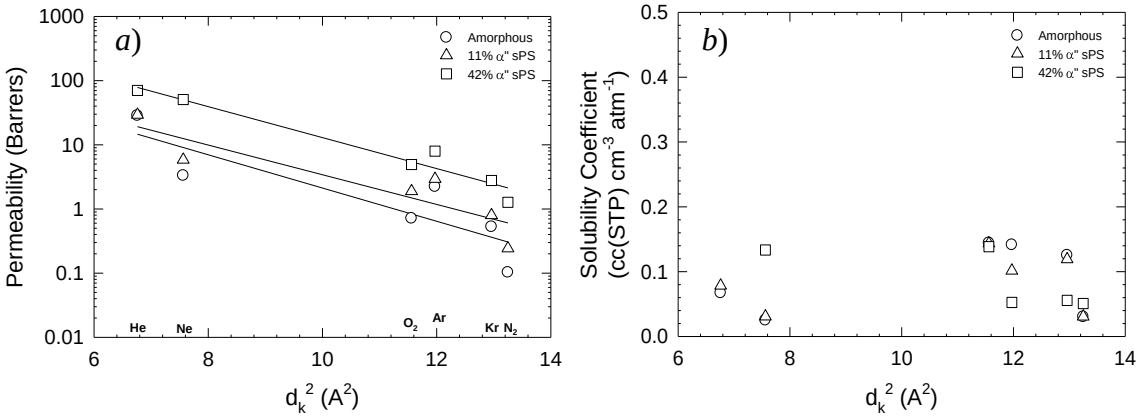

Figure 33. *a*) Permeability and *b*) solubility coefficient plotted as a function of kinetic diameter squared.

The dependence of permeability and solubility coefficient as it relates to kinetic diameter is shown in Figure 33. Solubility remains relatively unchanged with varying crystallinity and permeant kinetic diameter. It is apparent from the trends in permeability that diffusion dominates the transport of light gases in this system. A general lack of interaction and homogeneously controlled nanoporous cylindrical cavities make α" syndiotactic polystyrene excellent sieving materials for size selective permeation.

Conclusions

A dynamic gas permeation system utilizing mass-spectrometer (DGPS-MS) was successfully developed, based on the principles of the dynamic differential approach. A powerful

turbomolecular pumping system in the downstream compartment of the permeation cell helped the rapid establishment of the equilibrium concentration of permeant. With a NIST calibrated film and constant volume variable pressure setup, independent calibration was achieved for DGPS-MS. The permeation results of various gases through different polymer membranes demonstrated that DGPS-MS has the capability to measure from very fast (no more than a few minutes) to slow (a couple of days) diffusion of different gases and gas mixtures. The data obtained from DGPS-MS agreed well with the literature value(s).

The diffusion characteristics of amorphous, α, and β forms of sPS were successfully measured via the DGPS-MS system. It was shown that the amorphous and β forms demonstrate similar diffusion and did not vary depending on whether the diffusion was parallel or perpendicular to the chain axis. Conversely, experimental results as well as molecular dynamics simulations have shown that the unique "superstructure," packing of triplets forming hexagonally shaped nanochannels along the chain direction, found in the α" form of sPS facilitate high diffusion rates parallel to the chain direction in larger permeants (greater than 2.6Å). This was attributed to a transition from a nearly three-dimensional behavior for small permeant size, to a one-dimensional behavior for larger permeant sizes. Larger permeants are confined to the hexagonally shaped nanochannels between the triplets in the α" form and cannot move between parallel channels. The smaller permeants, however, can move relatively freely between neighboring channels, resulting in a more three-dimensional diffusion behavior.

References

1. Crank, J.; Park, G. S. In *Diffusion in Polymers* Medgi P. Ed; Academic Press: London and New York, 1968.

2. Vieth, W. R. In *Diffusion In and Through Polymers*, Hanser Verlag, Munich, 1991.

3. Pasternak, R. A.; Shimscheimer, J. F.; Heller, J. J. *J. Polym. Sci.* **1970,** *A2*, (8), 467.

4. Chern, R. T.; Coros, W. R.; Yui, B.; Hopfenberg, H. B.; Stannett, V. T. *J. Polym. Sci., Polym. Phys. De.* **1984,** *22*, 1061.

5. Felder, R. M. *J. Membrane Sci.* **1978,** *3*, 15.

6. Felder, R. M.; Spenge, R. D.; Ferrell, J. K. *J. App. Polym. Sci.* **1975,** *19*, 3193.

7. Pye, D. G.; Hoene, H. H.; Panar, M. *J. App. Polym. Sci.* **1976,** *20*, 287.

8. Eustache, H.; Jacquot, P. *Modern Plastics* **1968,** *45*, 163.

9. Ianno, N. J.; Makovicka, T. J. *Rev. Sci. Instr.* **1999,** *70*, 2072.

10. Laurenson, L.; Dennis, N. T. M. *J. Vac. Sci. Tech.* **1985,** *A3*, (3), 1707.

11. Mapes, M.; Hseuh, H. C.; Jiang, W. S. *J. Vac. Sci. Tech.* **1994,** *A-12*, (4), 1699.

12. Nörenberg, H.; Miyamoto, T.; Fukugami, N.; Tsukahara, Y.; Smith, G. D. W.; Briggs, G. A. D. *Vacuum* **1999,** *53*, 313.

13. Nörenberg, H.; Miyamoto, T.; Tsukahara, Y.; Smith, G. D. W.; Briggs, G. A. D. *Rev. Sci. Instr*. **1999,** *70*, 2414.

14. Webb, J. A.; Bower, D. I.; Ward, I. M.; Cardew, P. T. *J. Polym. Sci., Part B: Polym. Phys.* **1993,** *31*, 743.

15. Watson, J. M.; Baron, M. G. *J. Membr. Sci*. **1995,** *106*, 259.

16. TP., G. *Mag* **1866,** *32*, 402.

17. Koros, W.; Baker, R. W. In *Gas Separation, in: Membrane Separation Systems – Recent Developments and Future Directions*, Cussler E.L. Ed.;William Andrew Publishing, New Jersey 1991.

18. Breck, D. W., In *Zeolite molecular sieves: structure, chemistry and use*, John Wiley & Sons: New York, 1990.

19. Caro, J.; Noack, M.; Kolsch, P.; Schafer, R. *Microporous and Mesoporous Materials* **2000,** *38*, 3.

20. Koros, W. J.; Fleming, G. K. *J. Membr. Sci.* **1993,** *33*, 1.

21. Stern, A. *J. Membr. Sci.* **1994,** *94*, 1.

22. Van Krevelen, D. W., In *Properties of Polymers*, 3rd ed.; Elsevier: New York, 1990.

23. Puleo, A. C.; Paul, D. R.; Wong, P. K. *Polymer* **1989,** *30*, 1357.

24. Hodge, K.; Prodpran, T.; Shenogina, N. B.; Nazarenko, S. *J. Polym. Sci., Part B: Polym. Phys.* **2001,** *39*, 2519-2538.

25. Lin, H.; Freeman, B. D. *Macromolecules* **2006,** *39*, 3568.

26. Yoshino, M.; Ito, K.; Kita, H.; Okamoto, K. *J. Polym. Sci., Part B: Polym.Phys.* **2000,** *38*, 1707.

27. Teplyakov, V.; Meares, P.; . *Gas Separation and Purification* **1990,** *4*, 66-74.

28. Merkel, T. C.; V., B.; Nagai, K.; B.D., F. *J. Polym. Sci, Part B: Polym. Phys.* **2000,** *38*, 273.

29. Mercal, T. C.; Bondar, V.; Nagai, K.; Freeman, B. D.; Pinnau, I. *J. Polym. Sci, Part B: Polym. Phys.* **1999,** *38*, 413.

30. Brandrup, J.; Immergut, E. H.; Gruike, E. A.; Abe, A.; Bloch, D., *Polymer Handbook*. 4th ed.; John Wiley and Sons: 2005.

31. Tamai, Y.; Fukuda, M. *Polymer* **2003,** *44*, 3279-3289.

32. Olson, B. G.; Prodpran, T.; Jamieson, A. M.; Nazarenko, S. *Polymer* **2002,** *43*, 6775-6784.

CHAPTER IV

GUEST SORPTION IN δ_e SYNDIOTACTIC POLYSTYRENE: CHEMICAL WARFARE SENSING

Introduction

During the early twentieth century, various countries contributed to the development and deployment of biological and chemical weapons. In particular, sulfur mustard gas (2,2'-dichloro diethyl sulfide) is an alkylating chemical warfare agent that inflicts serious blisters upon contact with human skin. Sulfur mustard gas is considered a constant threat to the military owing to its simple method of preparation, low cost, incapacitating potential and ease of concealment. Despite efforts such as the 1925 Geneva Protocol for the prohibition of asphyxiating, poisonous, and/or bacteriological or gaseous methods of warfare agents during wartime,[1] terrorist organizations capable of producing viable chemical warfare agents has lead to a surge in research aimed at detecting these species.

Several requirements for a good detector include specificity towards the target analyte, fast response, mobility and ease of operation. Though effective, large and expensive detection systems based on gas chromatography and mass spectrometry require skilled operators, costly analyses, and long detection times. In an effort to overcome intrinsic deficiencies associated with current detection methods, extensive work has been conducted to merge sensing elements with high sensitivity transducers. Recently, gravimetric sensors based on quartz crystal microbalance technology have become of interest. The quartz crystal is a precise and stable oscillator capable of determining quantitative changes in mass through its direct relationship with oscillation frequency. Specifically, Saurbrey[2] established that change in frequency on the surface of a quartz crystal may be considered as an extension of the crystal itself according to:

$$\Delta f = \frac{-n}{t_q \rho_q} \Delta m \qquad (4.1)$$

Where: n is the harmonic frequency or overtone of interest (1, 3…13), t_q is the quartz crystal thickness (cm), ρ_q is the quartz crystal density (2.65 g cm^{-3}), Δm is the mass on the surface (ng cm^{-2}), and Δf is change in frequency of the crystal (Hz).

Quartz crystal microbalance based sensors are capable of detecting 2 ng cm^{-2} mass changes in air. However, they are only as effective as the sensing medium applied to their surface. One area of particular interest is that of polymer sorbent coatings. These materials sorb target analytes either on the surface (adsorption) or through the bulk (absorption), resulting in a change in mass. Polymers provide many advantages over existing sensor medium technology. They are relatively inexpensive, provide ease of fabrication, possess a wide variety of molecular structure, mechanical flexibility, and they can be deposited on various substrates.

The use of a host cavity organic and inorganic medium in conjunction with highly sensitive transducers is common in chemical sensing.[3-7] In particular, amorphous porous materials such as polyaniline[4] and poly(dimethylsiloxane)[3, 6] have been used as vapor phase chemical sensors. However, lack of sensitivity and loss in mechanical properties associated with high degrees of swelling limit their effectiveness. The primary emphasis of this research revolves around the clathrated δ phase of syndiotactic polystyrene possessing host guest interactions. Unlike their amorphous counterparts, crystalline sorption can actually lead to increases in mechanical properties. After uptake of 8 weight percent dichloroethane, syndiotactic polystyrene has shown a 5% increase in elastic modulus.[8] Previous work has revealed the potential of the nanoporous δ_e crystalline form of sPS to predominantly absorb aromatic hydrocarbon and halogenated low molecular compounds.[9-11] The capability of δ_e sPS to selectively absorb specific organic substances can be used to separate solvent mixtures or as sensing elements in senorics. Mensitieri et al.[12] showed that nanoporous sPS can be used as a sensing medium for the development of quartz crystal microbalance sensors for the detection of chlorinated compounds and other toxic volatile pollutants. The current research considers development of a new highly

sensitive quartz crystal microbalance based transducer for real-time detection in gaseous and aqueous environments the presence of dangerous chemical warfare agents. Specifically, mono-functional sulfur mustard simulant, 2-chloroethyl ethyl sulfide (CEES), and dimethyl methylphosphonate (DMMP), a nerve agent stimulant, were explored. Both samples being of similar size and molecular weight allows for the exploration of chemical selectivity.

Experimental

Quartz Crystal Microbalance System

QCM measurements were performed with a Q-SENSE E4 system equipped with an ISMATEC IPC high precision mechanical pump for liquid and custom built vapor control system for gas and vapor measurements. The crystals were 5MHz AT-cut gold coated quartz resonators with gold electrodes. Crystals were washed in methanol followed by acetone and cleaned with UV ozone for 30 min prior to use. If not stated otherwise, changes in normalized frequency of the third overtone (n=3, 15 MHz) are presented. Additionally, the crystal dissipation, which is related to viscoelastic response of the film, was measured simultaneously with frequency. In all cases, the film thickness is such that the film behaves rigidly, as the dissipation shift during the course of an experiment is less than $2x10^{-6}$. Under these conditions, adsorbed normalized masses, Δm, are deduced according to the Sauerbrey equation, $\Delta m = \Delta f * C/L$, with C=17.7 ng cm^{-2} Hz^{-1} and L=thickness cm, valid for thin, rigid films coupled without friction to the sensor surface.

The custom built apparatus designed to regulate gas and vapor pressure is shown in Figure 34. The entire system consists of ¼ inch stainless steel and Teflon tubing with high pressure ball valves purchased from Swagelok, designed to prevent corrosion. Vapor pressure was regulated by controlling mass transport of high purity nitrogen through a given solvent. The nitrogen gas is fed directly by a Teflon tube positioned at the bottom of a flask containing 100 ml solvent. In this method, test solvent saturated vapor pressure at room temperature represents maximum concentration. The saturated state is achieved by "bubbling" the nitrogen directly though the solvent. The addition of a secondary nitrogen flow reduces the concentration of the

vapor. Flow rates were controlled by identical adjustable two stage regulators connected to variable rate flow meters. The flow meter exiting the QC chamber was found to be within 5% of the sum of input flows, demonstrating limited pressure loss in the system.

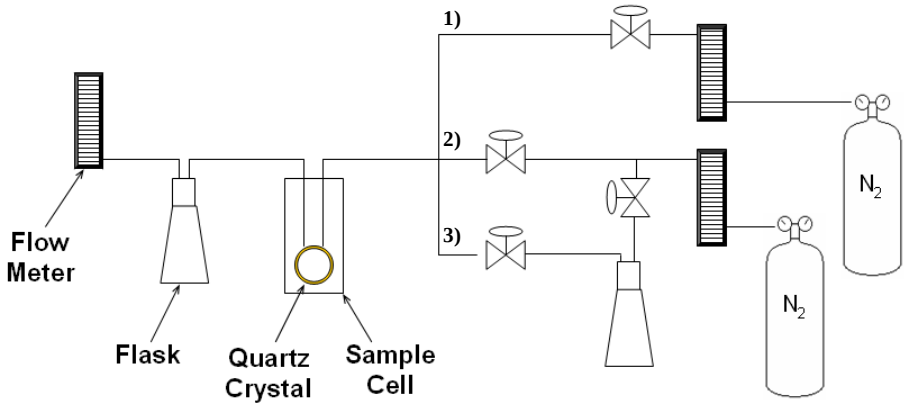

Figure 34. Model of a custom built vapor pressure control system.

Accurate thickness determination is essential for interpreting QCM results as coated volume directly relates to sorption characteristics of the sensing medium. Coated crystal thickness was determined through the frequency shift associated with coating of a pristine crystal and confirmed using scanning electron microscopy. Specifically, change in frequency between the pre-coated and post-coated crystal was found equivalent to mass of the coating per unit area. Dividing mass per unit area by the known coating density, determined from weight fraction crystallinity and known amorphous and 100% crystalline density, allows us to obtain thickness.

Headspace extraction and analysis. Two flat bottom flasks with rubber stoppers, as shown in the above system layout, allowed for in situ extraction of test vapor and subsequent headspace analysis through gas chromatography (GC). The headspace extraction process consists of four steps. First, a syringe is heated to 30°C in an oven for 20 min to avoid condensation. The syringe is transferred from the oven, penetrating the rubber stopper of the flask to ensure no gases enter or leave the controlled system. It is pumped 3 times to make certain syringe and headspace achieves equilibrium. A controlled aliquot of known volume (1ml) is removed from the headspace and injected directly into the GC.

In order to accurately determine the concentration of the test gas, analysis of saturated volume with known vapor pressure, well reported in literature at room temperature and one atmosphere pressure, was used as a standard and compared to vapor extracted downstream of the sample chambers. Conversion of the analog to digital signal was accomplished by integration of the area under the peaks and measurement of the peak height. Peak height was the preferred method showing the greatest reproducibility. In the discussions that follow, all data was reported as peak height. Each headspace measurement was repeated 3 times.

Material Preparation

Atactic and syndiotactic polystyrene with average molecular weight $M_w \approx 300{,}000$ g mol^{-1} and polydispersity $M_w/M_n \approx 2$ was supplied by the Dow Chemical Company, Midland, MI in pellet form**.**

Clathrated δ crystalline syndiotactic polystyrene. Samples containing the clathrated δ form were prepared by soaking amorphous syndiotactic polystyrene thin films (200 μm), as confirmed through WAXD, in guest solvents for 24 hours at ambient pressure and temperature followed by drying at room temperature.

32% δ_e Syndiotactic polystyrene. A solution of 0.5wt% sPS/$CHCl_3$ was spin coated onto a gold coated quartz crystal. The resulting coating contained a clathrated δ crystalline structure as confirmed through WAXD. Solvent extraction in supercritical CO_2 at 35°C and 200 bar for 1hr results in the δ_e crystalline phase.

42% δ_e Syndiotactic polystyrene. A solution of 0.5 wt% sPS/CS_2 was spin coated onto a gold coated quartz crystal. The resulting coating contained a completely amorphous structure as confirmed through WAXD. The amorphous sample was then converted to γ crystalline phase through conditioning in supercritical CO_2 at 35°C and 300 bar for 2 hrs. The sample was removed from the supercritical chamber and heated to 210°C for 1 hr followed by an ice water quench cooling, resulting in a transition to the α crystalline phase. Submerging of the sample in

CS_2 for 2 hours at 23°C allows for conversion to the clathrated δ crystalline phase. A final solvent extraction in supercritical CO_2 at 35°C and 200 bar for 1hr results in the δ_e crystalline phase.

Analysis

Solubility coefficient. The solubility coefficient, *S*, is defined as:

$$S = \Omega/p \tag{4.2}$$

Where: Ω is the volume ratio of low molecular weight permeant absorbed at equilibrium (cc(STP)) per volume of the sample (cm^3) and *p* is the final penetrant pressure (atm).

Diffusion coefficient. A simple and standard model for sorption experiments traditionally based on the transient pressure decay method developed by Crank was used to process QCM weight uptake measurements of similar design.[13] The measurement was modeled as one-dimensional diffusion into a plane sheet with the low molecular weight penetrant entering perpendicular to the plane surface. Edge effects are negated as the nature of QCM technique dictates that only the area in which the electrodes overlap induce frequency shifts. Furthermore, the ratio of area to thickness was incredibly small. Surface concentration was assumed to be independent of time as penetrant flow rates remained constant. Assuming Fickian behavior, values for the diffusion coefficient from transient sorption data was obtained utilizing the Crank initial-slope method[13]:

$$D = \frac{\pi}{16}\left[\lim_{t \to 0}\left(\frac{\frac{M(t)}{M_Y}}{\sqrt{\frac{t}{l^2}}}\right)\right]^2 \tag{4.3}$$

Where: $M_{(t)}$ is the mass uptake (g) of permeant at time t (sec), M_Y is the mass uptake of permeant at equilibrium , l is the thickness (cm) of the plane sheet, and D is the diffusion coefficient (cm^2 sec^{-1}) obtained from the linear portion of a plot of $M_{(t)}/M_Y$ vs $t^{0.5}$.

Results and Discussion

δ Syndiotactic Polystyrene

Upon fabrication of thin films at the specified conditions, wide angle X-ray diffraction (WAXD) and density measurements were conducted to verify the crystalline form. Figure 35 illustrates the X-ray diffraction pattern for clathrated δ and δ_e form syndiotactic polystyrene samples prepared from various solvents. Previous observations conclude that samples conditioned under supercritical CO_2 are converted from the clathrate to empty phase, as confirmed by WAXD and density measurements - demonstrating that the conditioned samples have a density less than 1.02 g cm^{-3}. The corresponding peak maximums for the emptied δ_e form are located at 2θ = 8.7 (010), 11.0 (210), 13.5 (220), 17.7 (020) (111), 21.3 (311) (321), 24.2 (421), and 28.3 degrees (132).[14]

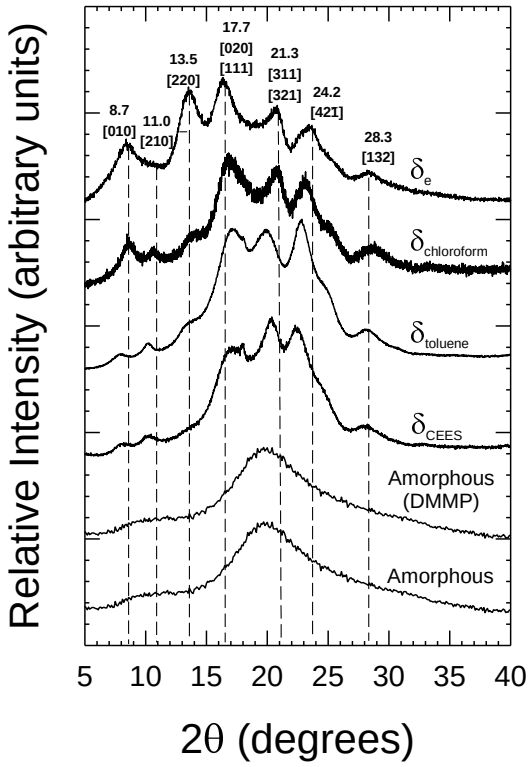

Figure 35. WAXD diffraction patterns for amorphous, clathrated δ (guest molecule indicated by subscript) and δ_e form syndiotactic polystyrene samples prepared from various solvents.

Chloroform and toluene have been shown extensively to form the clathrated structure with changes in crystalline diffractions indicative of changes in unit cell dimensions, the extent of which is beyond the scope of this research.[15] Chloroethyl ethyl sulfide (CEES) and dimethyl methyl phosphonate (DMMP) were chosen to determine the viability of using nanoporous δ phase sPS as a sensing medium for chemical warfare agents, in particular sulfur mustard gas. Results indicate CEES forms a clathrated δ phase while DMMP shows no sign clathrate formation despite similar size and molecular weight, demonstrating selective crystallization through preferential absorbance of the halide containing guest. In order for crystallization to take place, a certain amount of mobility must be allotted the polymer chains. The ability of the halogenated warfare agent to induce δ_e crystallization indicates high degrees of solvent ingress and alludes to potential selectivity.

Chloroform Liquid and Vapor Mass Uptake

Two characteristic frequency curves (where mass uptake is directly related to a decrease in frequency) of δ_e sPS coated sensors treated under chloroform vapor and in solution are shown in Figures 36a and b, respectively.

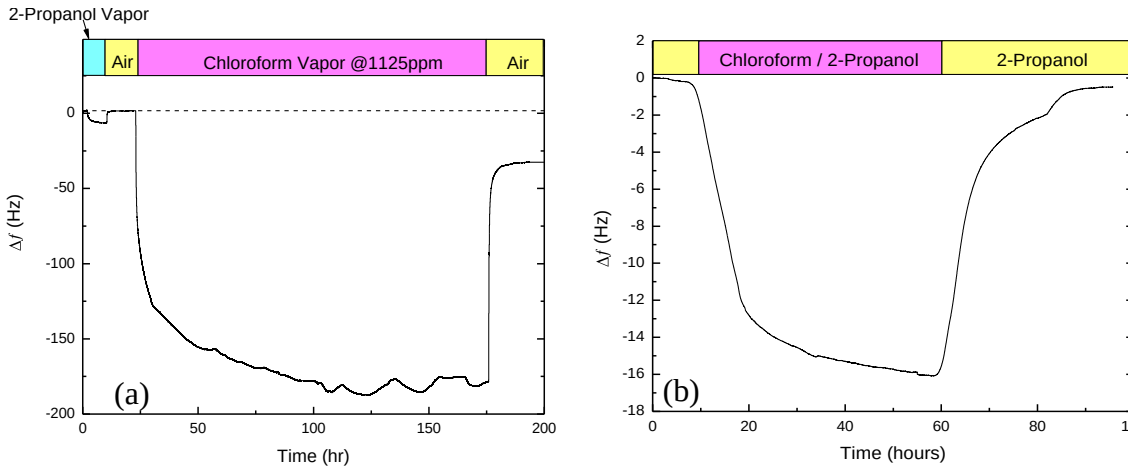

Figure 36. Corresponding change in frequency with time for 41% crystalline δ_e sPS treated under (a) isopropanol vapor followed by chloroform vapor, and (b) 10 mol% chloroform/isopropanol solution.

For both experimental methods, 2-propanol was used as a control due to its lack of affinity for sPS. In the case of 41% δ_e crystalline samples conditioned in 2-propanol vapor, shown in Figure 36a, a shift of 15Hz was observed. This frequency shift was observed in all measurements and was associated with condensation of the isopropanol on the surface of the sample. As observed, once the isopropanol vapor was evacuated from the chamber the baseline returned to normal. For chloroform vapor, it is demonstrated that the time to reach an equilibrium concentration is quite long (~150hrs). Though the overall kinetics of absorption appears to be long, the response time is actually rather short. A frequency shift of 80Hz (15.030g/100$g_{polymer}$) was observed within 10 minutes of vapor introduction. This result concludes that in practical applications a positive response to the presence of toxic industrial agents can be observed prior to equilibrium absorption. Additionally, an overall shift in the baseline of 40Hz (7.515g/100$g_{polymer}$) after equilibrium desorption has been obtained. This shift can be attributed to low concentrations

of chloroform vapor becoming trapped within the quadrapolar crystalline domains of the sensing medium. A summary of the vapor measurements are shown in Table 1. Initial experiments on 30% and 41% crystalline samples demonstrate that the sensitivity increased through increasing of the crystalline fraction. A direct correlation between crystalline fraction and sensor sensitivity cannot be made at this time. In order to determine this relationship a variation in the percent crystallinity is required. Though this may seem like a straight forward endeavor, complications arise when samples containing low degrees of crystallinity are considered, due to the inherent pathway for the formation of clathrated δ crystallinity via mobile amorphous domains. The answer may lie in varying the syndiotactic nature of PS through different synthetic routes and must be explored in greater detail, though this is beyond the scope of this research.

Shown in Table 1 is a comparison of the mass up-take for various solutions of chloroform in isopropanol ranging from 0.1 to 10 mol% chloroform. Tests conducted on 32% crystalline samples indicate that the response was below the detection limit for concentrations <1 mol% chloroform. It is established that with 10 mol% chloroform in 2-propanol, the mass up-take mainly takes place in the δ_e crystalline form and not the amorphous through the lack of frequency shift for the amorphous sample. It is also observed from Figure 36b that no chloroform became confined within the nanoporous structure, but rather indicated a two stage desorption process. The first stage can be attributed to unbound chloroform existing near the surface of the material. The second stage can be attributed to confined chloroform that is released through the decrease in chemical potential energy related to local concentration differences and a lower energy of activation associated with plasticized sPS amorphous domains.

Table 1

Equilibrium-Sorbed Amounts of Chemical Agent at 25°C

Sensing Medium	Testing agent	Sorbed agent (g/ 100 $g_{polymer}$)
Amorphous sPS		
0.2μm thick	$CHCl_3$ (vapor)	0.862
	$(CH_3)_2CHOH$ (vapor)	0.000
	0.1-10 mol% $CHCl_3/(CH_3)_2CHOH$	0.000
δ_e sPS		
32% cryst.	$CHCl_3$ vapor	7.532
	$(CH_3)_2CHOH$ vapor	0.00
	0.1 mol% $CHCl_3/(CH_3)_2CHOH$	0.00
	1 mol% $CHCl_3/(CH_3)_2CHOH$	0.598
	10 mol% $CHCl_3/(CH_3)_2CHOH$	2.763
41% cryst.	$CHCl_3$ vapor	33.155
	$(CH_3)_2CHOH$ vapor	1.750

Selective Vapor Mass Uptake

Characteristic frequency curves of δ_e sPS coated sensors treated under industrial vapors isopropanol, toluene, and chloroform are shown in Figure 37. This figure demonstrates the ability of the δ_e syndiotactic polystyrene coated quartz crystal to accurately detect mass uptake of various organic vapors in this system.

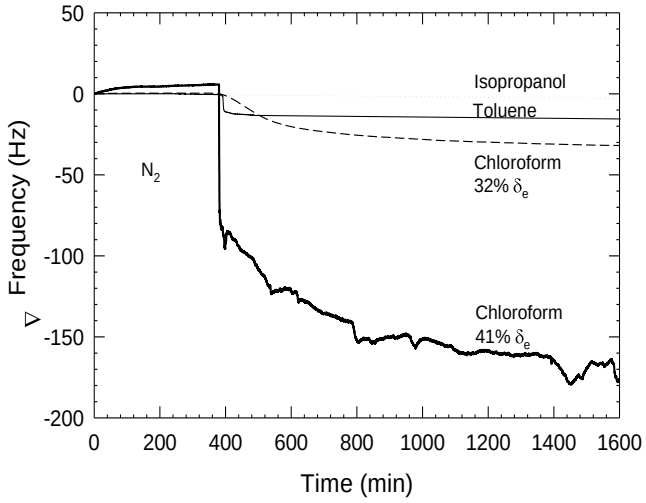

Figure 37. Frequency change with time for 32% δe sPS samples treated under chloroform (-) and 41% δe sPS samples treated under chloroform (-) and toluene (---) vapor.

An initial baseline was established for several hours using a constant N_2 flow with stability +/- 2Hz. Isoproanol was chosen as a control due to a lack of measurable frequency shift for both amorphous and semi-crystalline sPS during characteristic testing times. Toluene shows an equilibrium frequency shift of 13 Hz, corresponding to absorption of 1.756g/100$g_{polymer}$, occurring after one hour of testing. Both 32% and 41% δ_e crystalline samples demonstrate similar sorption kinetics with an equilibrium frequency shift after 17 hours. Though the rate of absorption is similar, the effect of crystallinity on equilibrium mass uptake is pronounced. Increasing crystallinity from 32 to 41% improves sorption by a factor of 4, from 7.532 to 33.155 g/100$g_{polymer}$. High degrees of crystallinity were obtained via solid state crystalline transition following the γ-α-δ_e pathway outlined in the experimental section. Presumably, the presence of the previously formed crystallite acts to assist the nucleation process, through introducing surfaces suitable in development of the lattice structure of the stable phase. The nature of the interaction between the host crystalline polymer and guest penetrant appears to drive mass uptake.

Utilizing a custom built QCM, Figure 38 demonstrates frequency shifts associated with the introduction of DMMP and CEES analytes. As observed in the WAXD analysis, the QCM sensor shows preferential adsorption towards the CEES blistering agent simulant at equilibrium vapor pressure. The relative lack of response for g-agent DMMP demonstrates selectivity of this material for halide containing penetrants and in particular CEES over other known warfare agents of similar volume. Furthermore, equilibrium mass uptake is achieved in a relatively quick 45 minutes with an overall sorption of 8.135 g/100g polymer.

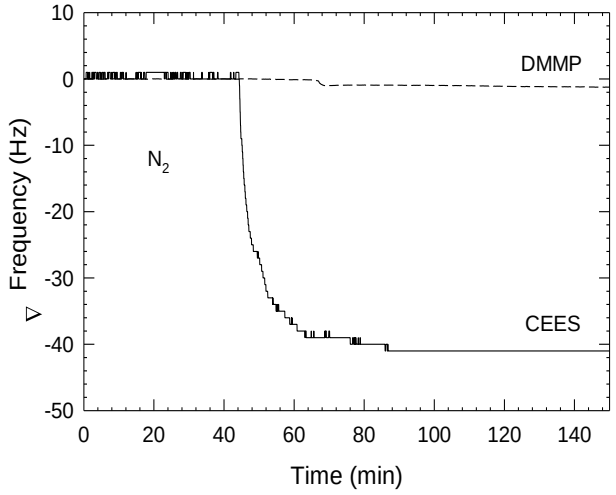

Figure 38. Change in frequency with time for δe sPS samples treated under DMMP (---) and CEES (-) warfare agent stimulant vapor.

The final equilibrium adsorption results for tests conducted on both amorphous and semicrystalline δe sPS samples are shown in Table 2. The increasing absorption with increasing crystallinity implies that the analyte is preferentially absorbed into the crystalline domains. Furthermore, the absorption is not a free volume driven process but rather a result of secondary interactions within the nanoporous structure of the crystalline domains, resulting in selectivity towards halogenated species.[16]

Table 2

Equilibrium-Sorbed Amounts of Analyte at 25°C

Sensing Medium	Test Analyte	Adsorption (g / 100g polymer)
Amorphous PS		
	Chloroform	0.862
	Isopropanol	0.000
δ_e sPS		
32% cryst.	Chloroform	7.532
	Isopropanol	0.000
41% cryst.	Chloroform	33.155
	Isopropanol	0.000
	Toluene	1.756
	DMMP	0.000
	CEES	8.135

Figure 39 provides a demonstration of intrinsic material recovery, reproducibility and effective selectivity through response magnitude in the crystalline domains. The magnitude of the response in the crystalline nanopore reiterates the importance of increased crystallinity made possible through original work on new crystalline/crystalline transition pathways described previously. Despite a relative deficiency in nanoporous crystalline δ_e sPS selectivity to a distinct molecular structure, reversibility makes this system an attractive first response mechanism over more selective materials.

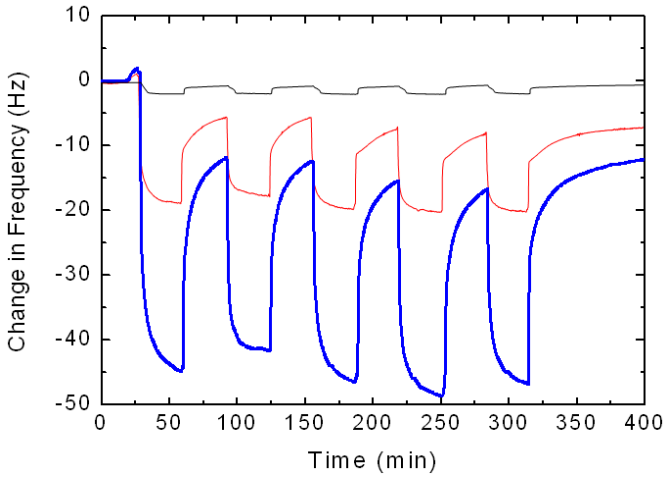

Figure 39. Effect of repeated exposure to chloroform in amorphous (black), 32% δ_e semicrystalline syndiotactic PS (red) and 41% δ_e syndiotactic PS (blue).

2-Chloroethyl Ethyl Sulfide Sensing

The 2-chloroethyl ethyl sulfide sorption isotherms at 35°C for amorphous atactic and semicrystalline syndiotactic polysyrene coated quartz crystals are well represented in Figure 40. When compared to amorphous plots, crytalline samples demonstrate greater uptake across all concentrations. The isotherm for amorphous atactic polystyrene is linear, consistent with the generally expected nature of gas and vapor sorption in rubbery polymers. Conversely, δ_e semicrystalline sPS samples are analogous Langmuir isotherms typical of dissolution in pre-existing microvoids.

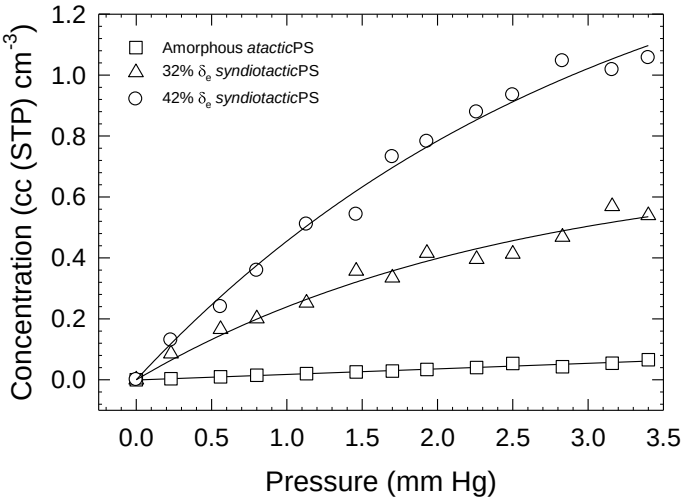

Figure 40. 2-chloroethyl ethyl sulfide sorption isotherms in semicrystalline and amorphous PS at 35°C.

The concave nature of the isotherm is well described by the dual mode sorption model, where penetrant sorption occurs in the equilibrium densified amorphous matrix and in the excess volume present in the nanoporous crystalline cavities. The total concentration of dissolved molecules or the solubility, *c*, is related with equilibrium pressure, *p*, and contributed from these two dissolution process:[17]

$$c = k_D p + c_H' bp/(1+bp) \tag{4.3}$$

Where: k_D is the solubility coefficient in Henry's law limit, c_H' is the Langmuir saturation constant, and *b* is the Langmuir affinity constant. Additionally, increased concentration at a given pressure is mirrored with an increase in the volume fraction of the crystalline domain. This is indicative of the high sorption capacity intrinsic to the low density crystalline nanopore.

Figure 41 is representative of crystalline amorphous ratio selectivity versus penetrant concentration. Selectivity is higher at low concentrations as a result of the Langmuir sorption intrinsic to the crystalline cavity as compared to Henry's type sorption of the amorphous domains. The increased crystalline amorphous ratio selectivity of the crystalline domains at low activity makes these materials highly beneficial in real world applications. Furthermore, the

importance of crystallinity is shown as 42% crystalline samples demonstrate higher selectivity over analogous 32% crystalline samples for all pressures.

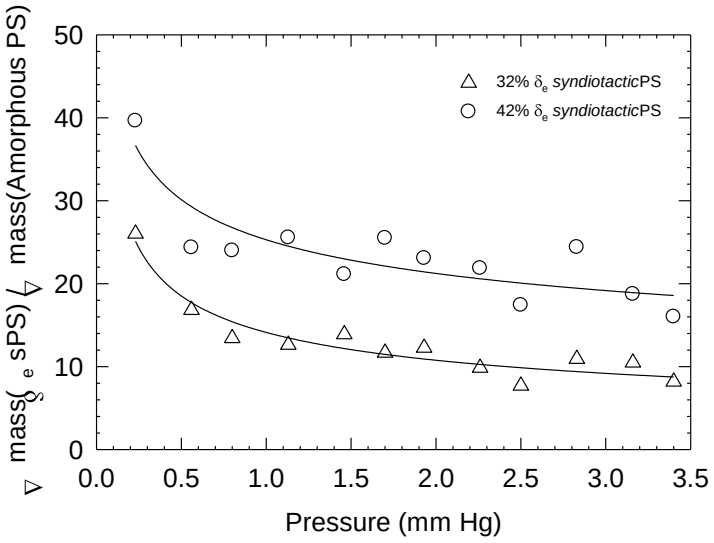

Figure 41. Change in crystalline amorphous ratio selectivity between semicrystalline δ_e phase and amorphous PS samples with concentration.

Figure 42 shows the mass uptake as measured by QCM plotted in the form of equation 4.3 for volume fraction crystallinity in polystyrene. In general, the initial fast stage has been found to be Fickian and the initial slope can be used to calculate the diffusion coefficient for the penetrant.

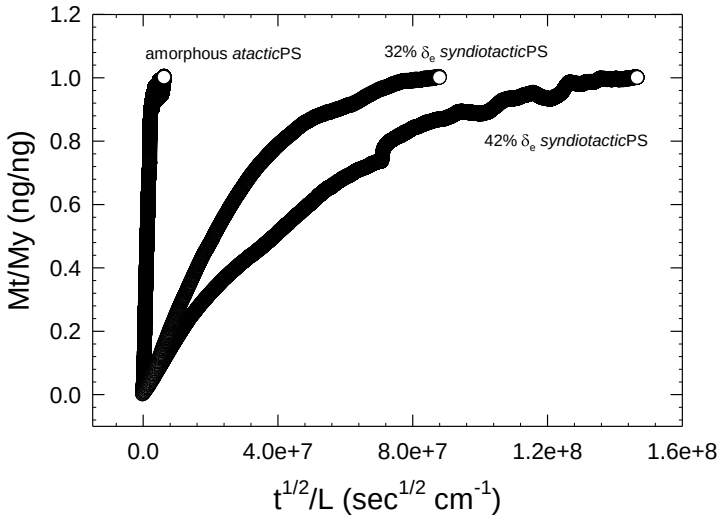

Figure 42. CEES sorption kinetics for amorphous atactic PS and 32% and 42% δ_e syndiotactic PS.

Typically for two stage absorption, the second stage is significantly slower than the first. Using the initial slope of the absorption and neglecting the non-Fickian behavior all samples were equally fit. For all samples, it was found that diffusion kinetics do not change with changing penetrant concentration. A definitive decrease in the rate of diffusion is observed as the volume fraction crystallinity increases. Typical diffusion process is modeled as a sequence of unit diffusion steps or jumps during which the particle passes over a potential barrier separating one position from the next. However, a certain number of van der Waals type or other interactions between the component molecules and chain segments must be broken to allow a rearrangement of the local structure. The amount of energy required for this rearrangement will increase as the mobility of the polymer matrix decreases. This process requires a localization of energy to be available to the diffusing molecule and its polymer chain segment neighbors to provide the energy needed for rearrangement against the cohesive forces of the medium with effective movement of the penetrant for a successful jump. The overall transport process is extremely sensitive to the magnitude and size distribution of holes available per unit time and volume for diffusive jumps as determined by the inherent or modified polymer chain segmental mobilities. It may be concluded that the increase in diffusion rate is representative of immobilized crystalline

chain segments requiring more energy and longer rearrangement time to allow for a diffusive jump to take place.

Conclusions

The solution and vapor sorption of several industrial and chemical stimulants within semicrystalline domains of δ_e syndiotactic polystyrene was studied using a quartz crystal microbalance technique. Sorption capacity is dominated by the crystalline domains. To increase the overall sensitivity of the sensing medium a new method for sample preparation was proposed. This method has utilized the ability to prepare high degrees of g phase crystallinity, through supercritical CO_2, to generate highly de crystalline samples via crystalline-crystalline solid state transitions. Sorption characteristics are established as a function of crystalline fraction and chemical properties of the test analytes. The use of δ_e crystalline phase sPS as a sensing medium in cooperation with QCM to selectively detect the chemical warfare stimulant 2-chloroethyl ethyl sulfide was demonstrated. Selectivity was shown to be higher at low concentrations making these materials highly beneficial in real world applications. A definitive decrease in the rate of diffusion is observed as the volume fraction crystallinity increases. This is representative of immobilized crystalline chain segments requiring more energy and longer rearrangement time to allow for a diffusive jump to take place.

References

1. Geissler, E., *Biological and Toxin Weapons Today*. Oxford University Press Inc.: New York, 1986.

2. Sauerbrey, G. Z. *Z. Phys.* **1959,** *155*, 206.

3. Du, X.; Ying, Z.; Jiang, T.; Liu, Z.; Yang, T.; Xie, G. *Sens. Actuat.* **2008,** *B134*, 409.

4. Gao, J. B.; Sansinena, J. M.; Wang, H. L. *Synth. Metals* **2003,** *135*, 809.

5. Mulloni, V.; Pavesi, L. *Appl. Phys. Lett.* **2000,** *76*, 2523.

6. Perez, G. P.; Crooks, R. M. *Anal. Chem.* **2004,** *76*, 4137.

7. Pisco, M.; Consales, M.; Cutolo, A.; Cusano, A.; Penza, M.; Aversa, P. *Sens. Actuat.* **2008,** *B129*, 163.

8. Daniel, C.; Sannino, D.; Guerra, G. *Chem. Mater.* **2008,** *20*, 577.

9. Chatani, Y.; Shimane, Y.; Inoue, Y.; Inagaki, T.; Ishioka, T.; Ijitsu, T.; Yukinari, T. *Polymer* **1992,** *33*, 488.

10. Guerra, G.; Vitagliano, V. M.; De Rosa, C.; Petraccone, V.; Corradini, P. *Macromolecules* **1990,** *23*, 1539.

11. Immirzi, A.; de Candian, F.; Iannelli, P.; Vittoria, V.; Zambelli, A. *Makromol. Chem. Rapid Commun.* **1988,** *9*, 761.

12. Mensitieri, G.; Venditto, V.; Guerra, G. *Sensors and Actuators* **2003,** *B92*, 255-261.

13. Crank, J.; Park, G. S. In *Diffusion in Polymers*; Mendi P.; Academic Press: London and New York, 1968.

14. Rizzo, P.; Mensitieri, G.; Di Maio, L. *Macromol. Symp.* **2002,** *185*, 65.

15. De Rosa, C.; Guerra, G.; Petraccone, V.; Pirozzi, B. *Macromolecules* **1997,** *30*, 4147-4152.

16. Milano, G.; Guerra, G.; Cavallo, L. *Eur. J. Inorg. Chem.* **1998**, 1513.

17. Stern, S. A.; Trohalaki, S. In *Barrier Polymers and Structures*; Koros, W. J., Ed.; American Chemical Society: Washington DC, 1990.

CHAPTER V

GUEST SORPTION IN δ_e SYNDIOTACTIC POLYSTYRENE: EFFECT OF SIZE AND ELECTRONEGATIVITY

Introduction

The primary emphasis of this chapter revolves around the clathrated δ phase of syndiotactic polystyrene possessing host guest interaction. Two solvent induced γ and δ forms of syndiotactic polystyrene (sPS) demonstrate s(2/1)2 helical chains having TTGG conformation with an identity period c = 7.7 Å, by means of the δ crystalline lattice encaging guest solvent molecules (clathrated δ form), while γ is absent of guests. Unlike the γ form, upon removal of the guest solvent by appropriate techniques, a nanopore (a = 17.40 Å, b = 11.85 Å, and $\gamma=117^{\circ}$) is created within the crystalline unit cell, resulting in the δ_e form.[1] The crystalline density of the δ_e form is 0.977 g cm^{-3}, much lower than that of amorphous sPS, 1.049 g cm^{-3}. It has been shown that samples of sPS in the δ_e form rapidly absorb molecules of suitable organic substances and transform into the clathrate δ form.[2-4] Investigation of sorption behavior in these systems have shown impressive selectivity towards polar and halogenated guest molecules as compared to nonpolar molecules, suggesting that specific interactions between the cavities and guests may be implied.[5-7] One of the only known analogous low density crystalline polymers, isotactic poly(4-methyl-1-pentane), also absorbs gases such as CO_2 or CH_4; however, the molecules do not form a clathrate structure, they dissolve into the crystalline phase at a much lower concentration compared to the amorphous phase and show no selectivity.[8] X-ray diffraction and FTIR spectroscopy have been used extensively to study the molecular interactions that occur between guest molecules and host nanoporous syndiotactic polystyrene. Milano and co-workers have explored crystal structure parameters, guest volume and volume of the δ_e sPS cavity for dichloroethane, iodine, and toluene guest molecules.[9] A distinct change in cavity size accompanied by increasing guest volume indicates a crystalline host structure capable of dynamic

swelling. Dynamic because removal of said guests results in a total recovery of the initial δ_e cavity size (115 $Å^3$). Additionally, sorption studies of a broad range of alkyl and cyclic guests including several chlorinated molecules, experimentally demonstrated that guest volumes up to 250 $Å^3$ can be encapsulated within the sPS host cavity.[10]

Though work has shown size selectivity based on calculated van der Waals guest volume, the question still remains as to what role electrostatic interactions play in the accommodation of guest molecules. If it is strictly based on size, two guests with equal volume should occupy the cavity to the same extent. However, Guerra and coworkers discovered that gauche and trans conformations of 1,2-dichloroethane and 1,2-dichloropropane absorbed in the amorphous domains of the sPS samples are nearly equally populated, whereas the trans conformation largely prevails for molecules trapped in the host cavities of the crystalline δ-form.[1, 11, 12] In this case, molecular mechanics energy minimization results indicate conformational selectivity based on a good electrostactic fit with the extensively quadrapolar cavity.[11] Despite a comprehensive study concerning model systems of benzene/X_2 (X=F, Cl, Br, I), no work has experimentally explored the effect of halide electrostatic interaction as it relates to syndiotactic polystyrene amorphous and crystalline domains. Systematically studying the transport characteristics between various alkyl halide test analytes is the logical next step in determining the role that electrostatic interactions and size play in the sorption of host sPS nano-pores.

Background

The study of sorption in polymers involves both the equilibrium uptake and kinetics of the absorption process. The rate of vapor sorption can be used to estimate the diffusion coefficient of a vapor. The measurement of this transport rate can also be used to study relative mobility rates of a penetrant and the polymer chain during the sorption process.[13]

It has long been known that the gas diffusion mechanisms are drastically different in rubbery and glassy polymers, due to the fact that glassy polymers are not in a state of true

thermodynamic equilibrium.[14] The difference in mechanism is reflected in the significant differences observed by the dependence of the diffusivity coefficient, as well as the permeability and solubility coefficients on the penetrant gas pressure, concentration in polymers, and on temperature.

Rubbery polymers have very short relaxation times and respond rapidly to external stresses. A change in a temperature results in an immediate adjustment to a new equilibrium state. Similarly, the absorption equilibrium can be established rapidly when small gas molecules are sorbed by rubbery polymers. The diffusivity, solubility and permeability coefficients for light gases in rubbery polymers are usually found to be independent of concentration and applied pressure.

By contrast, glassy polymers have very long relaxation times and long segmental chain motions are restricted. Segmental motion is further exacerbated when one considers polymeric crystalline structures. The diffusivity coefficients for light gases in glassy polymers are commonly nonlinear functions of pressure and concentration that increase significantly with increasing concentration, reaching a constant value at sufficiently high concentrations. The solubility and permeability coefficients are also highly dependent on concentration and pressure. A theory known as the "dual-mode sorption" model was proposed to explain this concentration dependence of gas transport parameters in glassy polymers.[14] In this model, it was suggested that two distinct modes of gas sorption and diffusion in glassy polymers exist: (1) normal dissolution of gas molecules into the polymer as in rubbery polymers, following Henry's law and (2) dissolution of gas molecules in the pre-existing microvoids in the polymer matrix, following Langmuir isotherm. The total concentration of dissolved molecules or the solubility, *c*, is related with equilibrium pressure, *p*, and contributed from these two dissolution process:[14]

$$c = k_D p + c_H' bp/(1+bp) \tag{5.1}$$

Where: k_D is the solubility coefficient in Henry's law limit, $c_H^{'}$ is the Langmuir saturation constant, and b is the Langmuir affinity constant. This dual-sorption model is widely accepted because of the excellent agreement between experimental results and theoretical predictions.

Penetrant sorption in polymers is regarded as a two step thermodynamic process: (1) condensation of the gaseous penetrant to a liquid-like density and (2) mixing of the pure compressed penetrant with the polymer segments.[15] One of the fundamental factors governing the equilibrium sorption of a vapor in a polymer is the Flory-Huggins interaction parameter, a measure of intermolecular interaction between the polymer and vapor. There are several methods of obtaining this value - we will consider two. First, uptake of vapor in a polymer is frequently described using the Flory-Huggins expression:[16]

$$\ln a = \ln \phi + (1-\phi) + \chi(1-\phi)^2 \tag{5.2}$$

Where: penetrant activity, a, is equal to the relative pressure, p/p_{sat}, p_{sat} is the saturation vapor pressure under ambient conditions, χ is the Flory-Huggins interaction parameter and the volume fraction of sorbed penetrant, ϕ, is calculated from the equilibrium penetrant concentration in the polymer, C, according to:[17]

$$\phi = \frac{C_a(V_1 / 22{,}414)}{1 + C_a(V_1 / 22{,}414)} \tag{5.3}$$

Where: V_1 is the saturated liquid penetrant partial molar volume ($cm^3\ mol^{-1}$). Therefore, χ can be obtained for polymer penetrant systems where activity and the volume fraction of sorbed penetrant are known.

Many researchers observed a linear correlation between the semi-logarithmic dependence of solubility with measures of gas condensability such as normal boiling point,[18] Lennard-Jones force constant,[19] and critical temperature.[20] For gases in liquids, Korosy[21] demonstrated that solubility can be expressed as:

$$LnS = a + bT_c \tag{5.4}$$

Where: the intercept, *a*, and slope, *b*, are adjustable constants. Furthermore, Korosy hypothesized that physical forces are responsible for the solubility relation to gas condensability and that chemical affinity results in deviation from this relation.[21] Gee et al.[18] further dissected the solubility relationship with gas boiling point into fundamental thermodynamic parameters. Utilizing the Guldberg-Guye rule,[20] relating boiling point and critical temperatures (i.e T_b=0.6T_c), Gee's expression may be written as:

$$LnS = -(4.5 + \chi) + \left(\frac{0.6\Delta S_{vap}}{RT} \right) T_c \tag{5.5}$$

Where: *S* is gas solubility in the polymer in units of cc(STP) cm^{-3} atm^{-1}, ΔS_{vap} is the entropy of vaporization of the penetrant gas at its normal boiling point with a value of 20 cal mol^{-1} K^{-1} according to Trouton's rule, *R* is the universal gas constant (1.987 cal mol^{-1} K^{-1}), and *T* is absolute temperature K. Expanding Korosy's work from liquids to polymers, Michaels and Bixler[22, 23] demonstrated similar slope values. In this study both methods are fit to experimental results and used to characterize differences in χ value as it relates to monosubstituted linear organohalides of varying electronegativity in amorphous and δ_e semicrystalline syndiotactic polystyrene thin films.

Experimental

Quartz Crystal Microbalance System

QCM measurements were performed with a Q-SENSE E4 system equipped with an ISMATEC IPC high precession mechanical pump for liquid and custom built vapor control system for gas and vapor measurements. A thermoelectric heating device regulates temperature with accuracy +/- 0.02 K. The crystals were 5MHz AT-cut gold coated quartz resonators with gold electrodes. Crystals were washed in methanol followed by acetone and cleaned with ultraviolet ozone for 30 min prior to use. If not stated otherwise, changes in normalized frequency of the third overtone (n=3, 15 MHz) are presented. Additionally, the crystal

dissipation, which is related to viscoelastic response of the film, was measured simultaneously with frequency. In all cases, the film thickness is such that the film behaves rigidly, as the dissipation shift during the course of an experiment is less than $2x10^{-6}$. Under these conditions, adsorbed normalized masses, Δm, are deduced according to the Sauerbrey equation, $\Delta m = \Delta f * C/L$, with C=17.7 ng cm^{-2} Hz^{-1} and L=thickness cm, valid for thin, rigid films coupled without friction to the sensor surface. [24]

The custom built apparatus designed to regulate gas and vapor pressure is shown in Figure 43. The entire system consists of ¼ inch stainless steel and Teflon tubing with high pressure ball valves purchased from Swagelok, designed to prevent corrosion. Vapor pressure was regulated by controlling mass transport of high purity nitrogen gas through liquid solvents. The nitrogen gas is fed directly by a Teflon tube to the bottom of a flask containing 100 ml solvent. In this method, test solvent saturated vapor pressure at room temperature represents maximum concentration. The saturated state is achieved by "bubbling" the nitrogen directly though the solvent. The addition of a secondary nitrogen flow reduces the concentration of the vapor. Flow rates were controlled by identical adjustable two stage regulators connected to variable rate flow meters. The flow meter exiting the QC chamber was found to be within 5% of the sum of input flows, demonstrating limited pressure loss in the system.

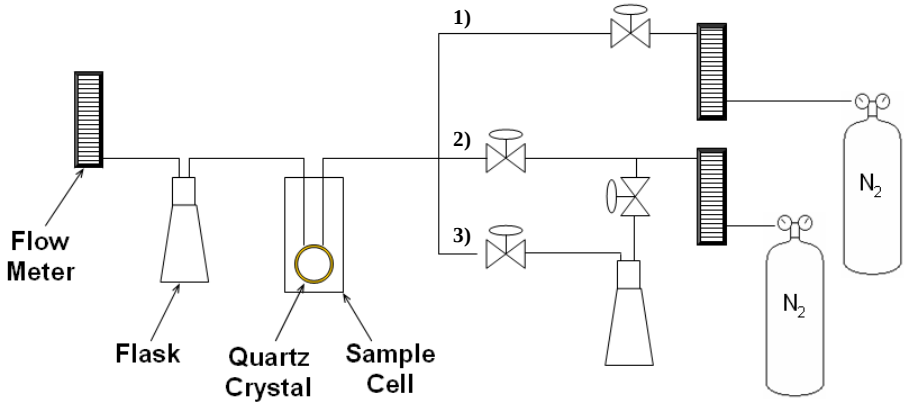

Figure 43. Custom built vapor pressure control system.

Spin coating procedure. Five micro-liters of solution were injected onto the center of the quartz crystal prior to beginning the spin coating process. Samples were spin coated at 5000 rpm for one minute. Accurate thickness determination is essential for interpreting QCM results. Spin coated crystal thickness was determined through the frequency shift associated with coating of a pristine crystal and confirmed using scanning electron microscopy. Specifically, change in frequency between our pre-coated and post-coated crystal were found equivalent to mass of the coating per unit area. Dividing mass per unit area by the known coating density allowed for thickness determination.

Headspace extraction and analysis. Two flat bottom flasks with rubber stoppers as shown in the system layout allowed for in situ extraction of test vapor and subsequent headspace analysis through gas chromatography (GC). The headspace extraction process consists of four steps. First, a syringe is heated to 30°C in an oven for 20 min to avoid condensation. The syringe is transferred from the oven, penetrating the rubber stopper of the flask to ensure no gases enter or leave the controlled system. The graduated volume is cycled 3 times to make certain syringe and headspace achieves equilibrium. A controlled aliquot of known volume (1 ml) is removed from the headspace and injected directly into the GC unit.

In order to accurately determine the concentration, analysis of saturated volume with known vapor pressure (well reported in literature at 20°C and one atmosphere pressure) was used as a standard and compared to vapor extracted downstream of the sample chambers. Conversion of the analog signal to digital data was accomplished by integration of the area under the peaks and measurement of the peak height. Peak height was the preferred method showing the greatest reproducibility. In the discussions that follow, all data was reported as peak height. Each headspace measurement was repeated three times with standard deviations reported.

Material Preparation

Atactic and syndiotactic polystyrene with average molecular weight $M_w \approx 300{,}000$ g mol^{-1} and polydispersity $M_w/M_n \approx 2$ was supplied by the Dow Chemical Company, Midland, MI in

pellet form. Atactic polystyrene, lacking the structural regularity necessary for crystallization, was chosen as an amorphous control to eliminate the threat of solvent-induced crystallization.

32% δ_e Syndiotactic polystyrene. A solution of 0.5 wt% sPS/$CHCl_3$ was spin coated onto a gold coated quartz crystal. The resulting coating contained a clathrated δ crystalline structure as confirmed through wide angle x-ray diffraction (WAXD). Solvent extraction in supercritical CO_2 at 35°C and 200 bar for one hour results in the δ_e crystalline phase.

42% δ_e Syndiotactic polystyrene. A solution of 0.5 wt% sPS/CS_2 was spin coated onto a gold coated quartz crystal. The resulting coating contained a completely amorphous structure as confirmed through WAXD. The amorphous sample was then converted to γ crystalline phase through conditioning in supercritical CO_2 at 35°C and 300 bar for two hours. The sample was removed from the supercritical chamber and heated to 210°C for one hour followed by an ice water quench cooling, resulting in a transition to the α crystalline phase. Submerging of the sample in CS_2 for 2 hours at 23°C allows for conversion to the clathrated δ crystalline phase. A final solvent extraction in supercritical CO_2 at 35°C and 200 bar for one hour ensures removal of all solvents and the formation of the δ_e crystalline phase.

Test Penetrants

All solvents were reagent grade, purchased from Aldrich Chemical Company. Physical properties are outlined below in Table 3.

Table 3

Physical Properties of Test Penetrants

Test Analyte	Molecular Formula	Molecular Mass (g/mol)	Density (g/cm^3)	Boiling Point (^oC)	Vapor Pressure (mm Hg @ 20C)	Van Der Waals Volume ($cm^3\ mol^{-1}$)
Chloropropane	C_3H_7Cl	78.54	0.890	47	284.90	45.75
Chlorobutane	C_4H_9Cl	92.57	0.880	79	80.00	55.98
Chloropentane	$C_5H_{11}Cl$	106.59	0.880	107	20.25	66.21
Chlorodecane	$C_{10}H_{21}Cl$	176.73	0.868	223	0.10	117.36
Bromoethane	C_2H_5Br	108.97	1.470	38.4	389.89	38.30
Bromopropane	C_3H_7Br	123.01	1.354	70.9	99.76	48.53
Bromobutane	C_4H_9Br	137.02	1.269	101.4	40.00	58.76
Bromopentane	$C_5H_{11}Br$	151.05	1.204	130	12.50	68.99
Bromodecane	$C_{10}H_{21}Br$	221.8	1.069	241	0.06	120.14
Iodoethane	C_2H_5I	155.97	1.950	71	100.00	43.08
Iodopropane	C_3H_7I	169.99	1.74	101	43.00	53.31
Iodobutane	C_4H_9I	184.02	1.617	130	13.88	63.54
Iodopentane	$C_5H_{11}I$	198.05	1.517	154	3.65	73.77
Iododecane	$C_{10}H_{21}I$	268.18	1.257	132	0.01	124.92

Results and Discussion

Sorption

Sorption isotherms have been measured for a variety of linear organic halide penetrants in amorphous atactic polystyrene and semicrystalline δ_e phase syndiotactic polystyrene thin films at 35°C and partial pressures below atmospheric. Each penetrant was measured three times; a sample of the raw data for chloropropane in amorphous polystyrene is shown in Figure 44. Also shown are desorption kinetic plots, overlaid with the corresponding sorption kinetic response.

Minimal variation was observed over all samples between sorption and desorption kinetic processes, typical of low penetrant concentration in polymeric systems. It was assumed that sorption and desorption diffusivity is independent of concentration, analogous to low penetrant activity sorption kinetic processes following Henry's Law.

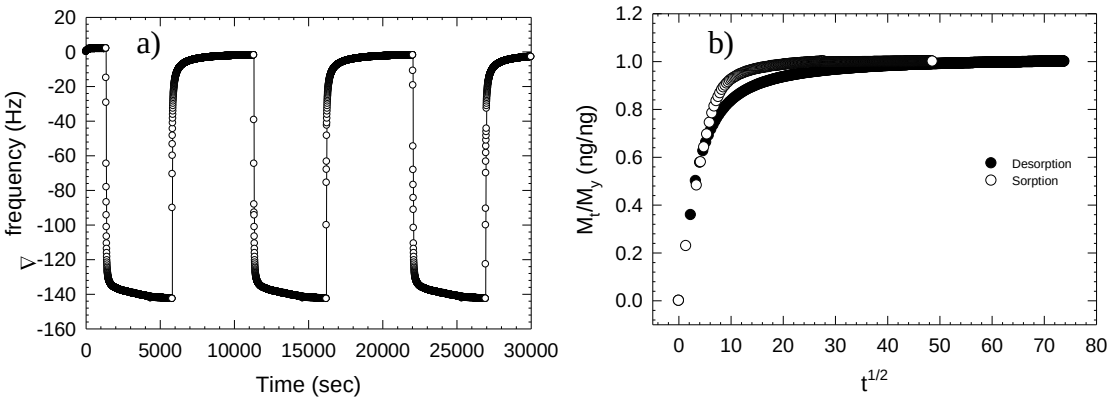

Figure 44. Representative experimental a) QCM frequency output with respect to time and b) sorption and desorption kinetic profiles for chloropentane in amorphous polystyrene.

All measurements were highly repeatable, providing high resolution statistical analysis of sorption and desorption kinetics. Raw data was converted from frequency to mass uptake using the Sauerbrey equation[24] and normalized according to thickness. The solubility coefficient (S) was defined as:

$$S = \Omega/p \tag{5.6}$$

Where: Ω is the volume ratio of low molecular weight penetrant absorbed at equilibrium (cc(STP)) per volume of the sample (cm^3) and p is the penetrant vapor pressure (atm). It is expected that the relationship between concentration and pressure would demonstrate dual mode sorption, typical of vapor and gas sorption in glassy polymers. However, in many polymers at low penetrant pressure, concentration is well described by Henry's law showing deviation to Langmuir type sorption as pressure increases. All measurements were conducted at pressures well below atmosphere. Therefore, in analyzing the data it was assumed that the solubility coefficient in the limit of zero absolute pressure approaches zero for all vapors:

$$S_{\infty} = \lim_{p \to 0} \frac{C}{p} \tag{5.7}$$

Infinite dilution solubility, S_{∞}, allows us to treat this system in a thermodynamic manner and model according to previous work by Gee.[18] Future work into the exact nature of the sorption process as it relates to pressure is needed to properly evaluate these assumptions.

Monosubstituted Linear Organic Halide Mass Uptake

Polystyrene coated quartz crystal microbalance response converted from frequency to mass uptake and normalized for film thickness with respect to chloro-alkane penetrants is shown in Figure 45. In all cases, penetrant sorption increases with increasing crystalline fraction, signifying greater loading capacity within the crystalline nanopore. The capacity of these nanopores for various guest solvents is well reported in the literature with guest/monomer-unit molar ratio generally 1:4.[11, 25-27] All samples were measured at a vapor activity of 0.30 +/-0.05. Vapor activity (*a*), assuming ideal vapor-phase behavior, was evaluated as p/p_o, where p is the pressure of vapor and p_o is the vapor pressure at the test temperature, 35°C.

The time to reach equilibrium sorption in the δ_e phase is greater than that of the amorphous phase, demonstrating a reduced kinetic response intrinsic to the host cavity. Similar results are reported for gas and vapor penetrants in the nanoporous crystalline cavity of syndiotactic polystyrene when compared to analogous amorphous domains.[28] For amorphous and semicrystalline syndiotactic polystyrene, increasing the penetrant molecular size also increases the time to reach equilibrium, a measure of diffusion rate. The diffusion coefficient is known to be concentration independent assuming Henry's law of solubility is applicable.

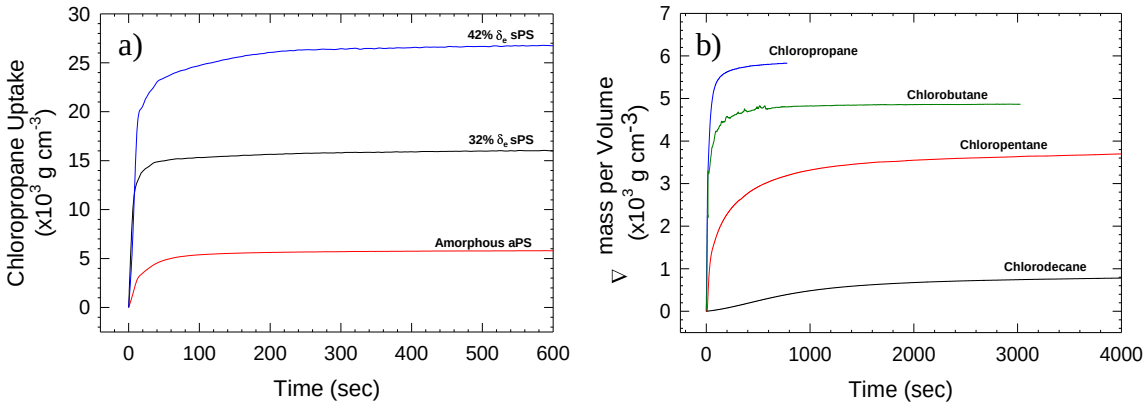

Figure 45. Mass uptake per unit volume of polymer with respect to time for a) chloropropane in atactic and δ_e syndiotactic polystyrene and b) various chloro-alkanes in amorphous polystyrene.

Mass uptake depreciates as 1-chloro-alkane chain length increases in amorphous syndiotactic polystyrene, expressed as ng cm^{-3} in Figure 45b. In fact, this process is representative of the penetrants at equal activity but it should be noted that the concentration of chlorodecane is by four orders of magnitude less than that of chloropropane at 35°C. The large mass difference between the penetrants combined with the nature of the experiment actually demonstrates that the system is more responsive towards heavier penetrants at equal concentrations.

Monosubstituted Linear Organic Halide Equilibrium Absorption

For varying linear alkyl chain length monosubstituted organic halides in *atactic*PS and 32 and 42% crystalline samples of δ_e *syndiotactic*PS, solubility isotherms are plotted with respect to critical temperature shown in Figures 46, 47, and 48. Considering the relationship between solubility and critical temperature first shown by Korosy[21] and later broken down into theoretical thermodynamic parameters by Gee[18], adjustable constants *a* and *b* were obtained and are provided in Table 4 below.

Table 4

Slope and Intercept Values for the Linear Dependence between lnS and T_c

Classification	Medium	b x 10^3 (K^{-1})	a ($cc/cm^3/atm$)
Rubbers	Natural Rubber	18[a]	
	Amorphous polyethylene	16[a]	
	Poly(butadiene)-hydrogenated	17[a]	
	Poly(dimethylsiloxane)	17[b]	
Glassy Polymers	polysulfone	17[c]	
	Poly(phenylene oxide)	16[d]	
	Poly(ethylene terephthalate)	19[e]	
Chloro-Alkanes	Amorphous Polystyrene	20.6	-13.82
	32% δe syndiotactic Polystyrene	28.4	-18.05
	42% δe syndiotactic Polystyrene	29.8	-17.35
	100% δ_e syndiotactic Polystyrene	29.8	-16.68
Bromo-Alkanes	Amorphous Polystyrene	18.4	-11.76
	32% δe syndiotactic Polystyrene	10.4	-6.05
	42% δe syndiotactic Polystyrene	10.3	-6.45
	100% δ_e syndiotactic Polystyrene	9.8	-4.53
Iodo-Alkanes	Amorphous Polystyrene	20.9	-13.71
	32% δe syndiotactic Polystyrene	6.1	-3.96
	42% δe syndiotactic Polystyrene	7.9	-4.52
	100% δ_e syndiotactic Polystyrene	9.1	-4.62

Note. [a]25C and 1 atm, [b]35C, [c]35C and 10 atm for all gases except n-C_4H_{10}, which is at infinite dilution. [d]35C and infinite dilution. [e]24-45C and infinite dilution. This table was reproduced from work explored by Freeman and coworkers.[22, 29-32]

Chloro-alkanes in this system present linear semilogarithmic dependence between solubility and critical temperature and therefore appear to follow classic thermodynamic models for vapors in glassy polymers proposed by Gee.[18] A best fit linear regression allows for determination of *a* and *b*.

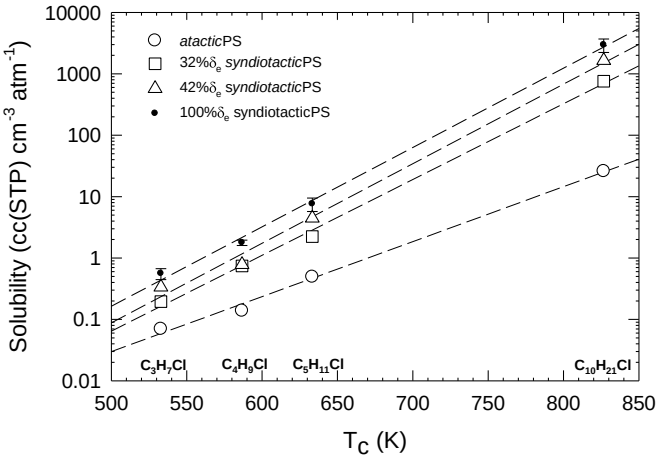

Figure 46. Monosubstituted chloro-alkane penetrant solubility as a function of solvent critical temperature.

It has been shown experimentally that specific interactions between gas molecules and polymer chains can cause deviations in the gas solubility from the expected value based on *lnS* vs T_c correlation. For example, significant deviations have been found for CO_2 solubility in many polymers.[33] Gee's[18] thermodynamic interpretation assumes the interaction parameter between polymer and penetrant deviates insignificantly. However, experimentally this is often not the case. For systems varying from a slope of 0.019 K^{-1}, Freeman et al.[29] proposed that the interaction parameter may be expressed as two adjustable constants, χ_0 and χ_1, determined from a least squared linear fit of experimental χ values, consisting of a penetrant family, versus critical temperature, $\chi = \chi_o + \chi_1 T_c$. Furthermore, Gee's[18] thermodynamic relation can be modified as follows:

$$LnS = -(4.5 + \chi_o) + \left(\frac{0.6\Delta S_{vap}}{RT} - \chi_1 \right) T_c \qquad (5.8)$$

This approach was taken by Freeman and coworkers[29] to deal with variations in the *lnS* vs T_c dependence of linear alkanes and fluorocarbon vapors in PDMS, LDPE and TFE/PMVE49, yielding excellent correlation and was adopted in this research.

Adopting this procedure, values of χ were calculated. The Flory Huggins interaction parameter, χ, is a relative measure of the affinity between penetrant and polymer. Values of χ were found to be lower in the crystalline host cavity than in the amorphous bulk. Therefore, van der Waals interactions are higher in the host cavity than the amorphous domains. Researchers have investigated the interaction between the phenyl group and penetrants; however to our knowledge, this is the first experimental obtainment of measure for the interaction present in the pore. Furthermore, this is the first report that the interactions in the pore are remarkably different than the bulk polymer. An effect that may be more pronounced for di-substituted organic halides as the work by Guerra et al. has demonstrated preference to the trans conformation of 1,2-dichloroethane.[9] It is important to point out that this is simply a first approximation and offers a guide for permeant selectivity in the δ_e crystalline phase. It is important to note the models for which this research is based were first utilized in liquids and may break down for samples with large void size, such as the system under investigation. However, in the limits of low penetrant concentration the model shows good agreement.

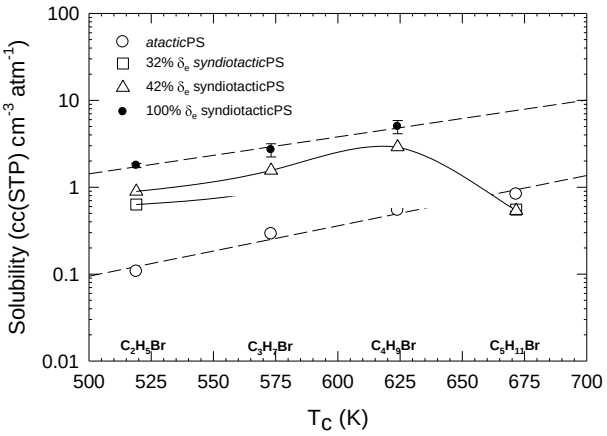

Figure 47. Bromo-alkane penetrant solubility as a function of solvent critical temperature for amorphous and δ_e *syndiotactic* polystyrene.

In the case of bromo-alkanes, homogeneous amorphous polystyrene samples correlate well, demonstrating a linear dependence across all penetrant critical temperatures. Short chain bromo-alkanes mirror this relationship up to three carbon backbone chain lengths. However,

bromopentane permeant demonstrates a very distinct decrease in sorption upon exposure to δ_e crystalline samples. While the absorption of monosubstituted bromine organohalides is accomplished by a similar enthalpy effect, for longer alkyl chain lengths - the interaction with the cavity reduces the conformational freedom of the molecule. The result is a decreased interaction with the pore. Extraction of the amorphous phase sorption shows that bromopentane is exclusively absorbed in amorphous domains. Therefore, we can assume that the size of the bromopentane molecule is too large for the host cavity. Bromopentane possesses a van der Waals volume of 114.56 A^3 mol^{-1}, only slightly larger than chloropentane, 109.94 A^3 mol^{-1}, and much less than chlorodecane at 194.88 A^3 mol^{-1}. Previous work has alluded to the fact that the pore is too small to accommodate a molecular penetrant with size greater than $250A^3$. **[9]** This creates a belief that interaction as well as size plays a critical role in δ_e phase cavity sorption. To expand on this concept, the idea that crystalline nanopores possess a critical size is not unjustified, but the critical size is dependent upon molecular shape and interaction. Therefore, the estimated pore size is a good approximation, but in fact varies depending on the nature of host/guest van der Waals interaction. It is noted that bromodecane was also tested, but the system showed minimum sorption and though we cannot rule out mass uptake, experimental scatter was such that the results could not properly be evaluated. It is inferred, bromodecane with van der Waals volume 199.50 A^3 mol^{-1} is incapable of sorption within the crystalline nanocavity.

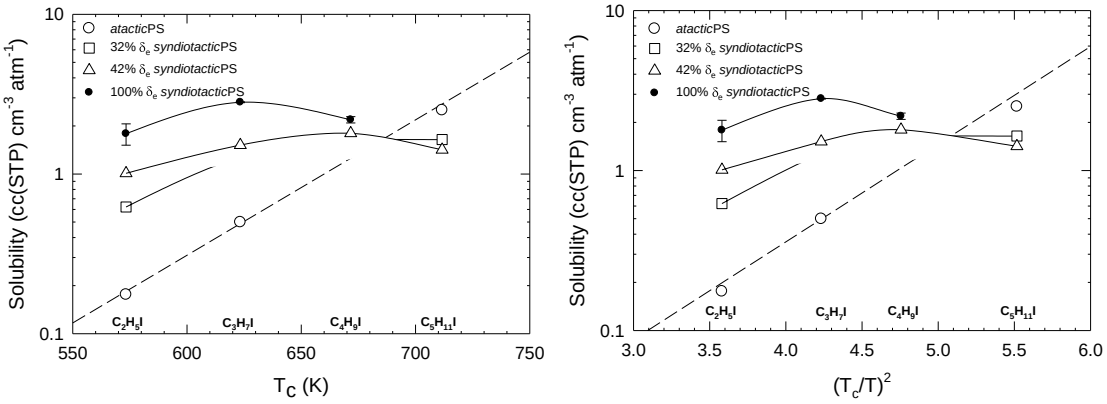

Figure 48. Iodo-alkane penetrant solubility as a function of a) solvent critical temperature and b) $(Tc/T)^2$ for amorphous and δ_e *syndiotactic* polystyrene.

In the case of iodo-alkanes, homogeneous amorphous polystyrene samples once again demonstrate a linear dependence across all penetrant critical temperatures. For iodo-alkanes in crystalline host/guest systems, a deviation from the classic model occurs and non linear behavior is observed. This process is most pronounced for penetrants iodobutane and iodopentane. The fact that iodobutane adsorption takes place in the nanoporous host cavity, but not to the extent that is expected, implies unfavorable conditions. One possibility is increased conformational entropy contributions related to the size of the penetrant adversely affecting the interactions present in the cavity. In a study concerned with separation of a hexane-cyclohexane solution using clathrated sPS,[34] it was determined that while the absorption of these two compounds is accomplished by a similar enthalpy effect - for the linear isomer, the interaction with the cavity would reduce the conformational freedom of the molecule. Therefore, the driving force for the preferential retention of the cyclic isomer is represented by the entropy factor. In contrast no substantial drop of entropy is expected to accompany the formation of clathrate with cyclohexane.

The experimental values for *b* are quite reasonable for amorphous polystyrene, however, this linear relation begins to break down as the size of the penetrant increases in bromo- and iodo-substituted series. Also, the effect is dependant not only upon the size but the van der Waals interactions associated with the guest halide. It would appear that chloroform interacts favorably

with styrene units in the amorphous bulk and crystalline host cavities, while changing to a less electronegative halide structure alters the relative solubility of the system. Furthermore, the cavity and the bulk amorphous phase differ in their interaction with the penetrant. As progression moves from bromo and iodo propane to butane the linear relationship between solubility and critical temperature is lost.

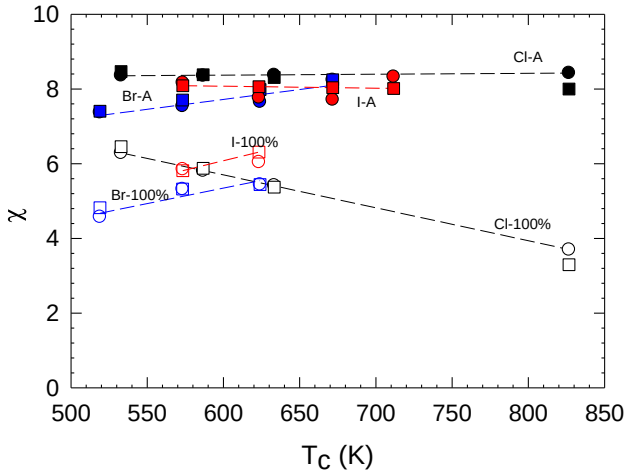

Figure 49. Flory-Huggins interaction parameter as a function of critical temperature. Closed symbols correlate to amorphous polystyrene while open symbols represent extrapolated 100% δ_e crystalline syndiotactic polystyrene.

It is of practical and scientific interest to investigate a correlation between χ value and chemical structure of monosubstituted linear organic halide penetrants in this system. Values of χ for amorphous and 100% δ_e crystalline sPS were obtained through use of the Flory-Huggins equation and extracted from *a* and *b* in which according to Freeman et al.[29], a modified Gee's correlation based on variation in χ with penetrant condensability is assumed. In Figure 49, χ is obtained using equation 5.2 and 5.8 and plotted versus critical temperature. In all cases amorphous polystyrene samples show good agreement with values reported by Van Krevlan[19] while the δ_e nanoporous cavity shows lower values of χ. A measure of polymer solvent interaction, lower χ values demonstrate greater affinity for the host guest interactions in the nanopore. In general, δ_e syndiotactic polystyrene possesses a greater affinity for organohalides than the amorphous bulk matrix. The nature of the nanopore would imply decreased interaction

with increasing electronegativity. For the polymeric material molecular size dependency of interaction parameter agrees with an expectation of χ varying in proportion to the molecular size in a homologous series of penetrants.[31] The nanoporous cavity demonstrates a lower χ value for chloro substituted penetrants and a progressively higher χ value as you progress from bromine to iodine containing organic halides.

One possibility is that χ changes due to the conformational entropy associated with accommodating a cylindrical organic halide in a spherical nanopore. With an increasing number of carbon groups in the organic halide backbone a decrease in the degrees of freedom results. This causes unfavorable deviation from the preferred T-shaped geometry proposed by Milano and coworkers[35] based on electrostatic fields generated by the two interacting molecules. This is similar to the explanation of why the trans- conformation of dichloroethane is preferred.

Absorption Process Kinetics

A simple and standard model for sorption experiments traditionally based on the transient pressure decay method developed by Crank was used to process QCM weight uptake measurements of similar design.[36] The measurement was modeled as one-dimensional diffusion into a plane sheet with the low molecular weight penetrant entering perpendicular to the plane surface. Edge effects are negated as the nature of QCM technique dictates that only the area in which the electrodes overlap induce frequency shifts. Furthermore, the ratio of area to thickness was incredibly small. Surface concentration was assumed to be independent of time as penetrant flow rates remained constant.

Assuming Fickian behavior, values for the diffusion coefficient from transient sorption data was obtained utilizing the initial-slope method by Crank:[36]

$$\frac{M_t}{M_\infty} = 2\left(\frac{Dt}{h^2}\right)^{0.5}\left(\frac{1}{\pi^{0.5}} + 2\sum_{n=1}^{\infty}(-1)^n ierfc\frac{nh}{2(Dt)^{0.5}}\right) \tag{5.9}$$

Where: M_t is the mass uptake (g) of permeant at time t (sec), M_∞ is the mass uptake of permeant at equilibrium , h is the thickness (cm) of the plane sheet, and D is the diffusion coefficient (cm^2 sec^{-1}). At short times ($M_t/M_\infty \leq 0.5$), this expression can be simplified to:

$$\frac{M_t}{M_\infty} = \frac{2}{h}\sqrt{\frac{Dt}{\pi}} \tag{5.10}$$

Which results in a simple expression for the diffusivity:

$$D = \frac{\pi}{4}\left(\frac{\frac{M_t}{M_\infty}}{\frac{\sqrt{t}}{h}}\right)^2 \tag{5.11}$$

The diffusion coefficient can be determined from the initial slope obtained from the linear portion of a plot of M_t/M_∞ vs $t^{0.5}/h$. This approach is fundamentally sound in the amorphous phase. However, there have been numerous examples of small molecule diffusion in polymers showing various non-Fickian behaviors, ranging from type II to two stage to sigmoidal. For the case of two stage absorption, the first stage Fickian in nature, is followed by an anomalous stage which is not diffusion controlled. Specifically, the nature of the crystalline host cavity is expected to lead to anomalous diffusion of type II, becoming more pronounced with larger penetrant size.

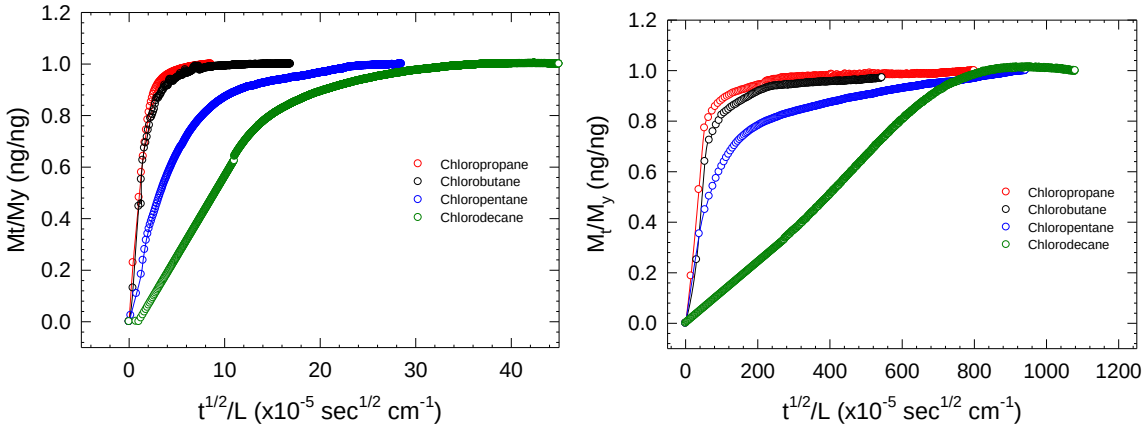

Figure 50. Isothermal mass uptake kinetic plots with respect to chloro-alkane penetrants in a) amorphous and b) 42% δ_e *syndiotactic* PS.

Figure 50 illustrates the mass uptake as measured by QCM plotted in the form of equation 5.11 for chloro-alkane penetrants in polystyrene. In general, the initial fast stage has been found to be Fickian and the initial slope can be used to calculate the diffusion coefficient for the penetrant. Typically for two stage absorption, the second stage is significantly slower than the first. Using the initial slope of the absorption and neglecting the non-Fickian behavior all samples were equally fit. The overall transport process is extremely sensitive to the magnitude and size distribution of holes available per unit time and volume for diffusive jumps as determined by the inherent or modified polymer chain segmental mobilities leading to differences in amorphous and crystalline diffusivity.

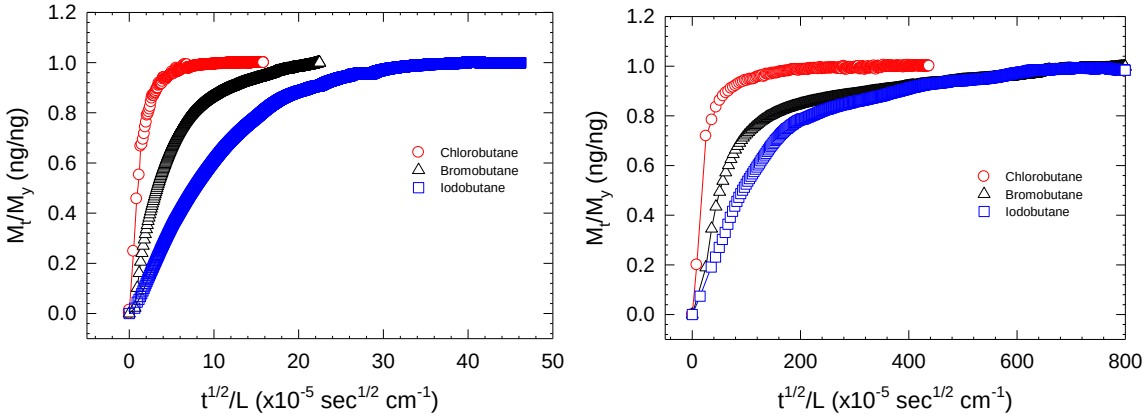

Figure 51. Isothermal mass uptake kinetic plots with respect to halide-butane penetrants in a) amorphous and b) 42% δ_e *syndiotactic* PS.

Shown in Figure 51 are the mass uptake kinetic plots for butane-halides in amorphous and 42% δ_e crystalline samples. A decreased kinetic response is observed with increasing halide size. In non-spherical penetrant diffusion, sorption rates are predominantly dependent upon effective diameter and not overall volume. In this manner the diffusion follows a process similar to reptation theory in which permeant molecules undergo diffusion along a snake like path consisting of segmental penetrant diffusion rather than one distinct penetrant jump. In linear molecular penetrants, larger individual backbone unit diameters negatively impact diffusivity. If we consider the monosubstituted halide as the limiting factor in this system experimental trends correspond to differences in halide critical diameters in the order of Cl < Br < I.

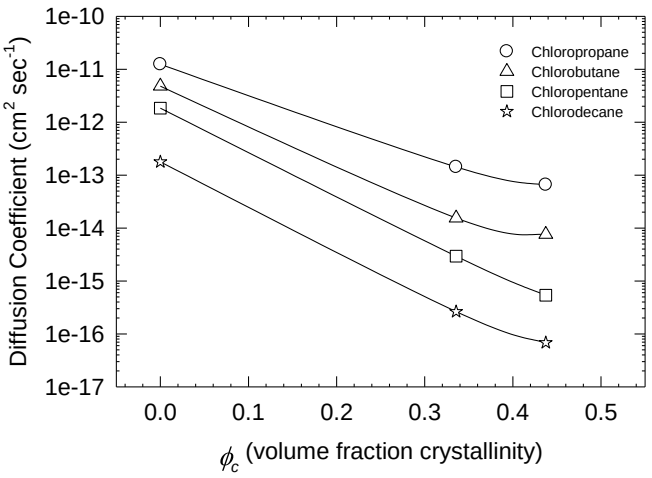

Figure 52. Dependence between diffusion coefficient and volume fraction crystallinity for linear chloro-alkane penetrants.

The diffusion coefficient was plotted with respect to volume fraction crystallinity for various alkyl chain length monosubstituted chloride penetrants, shown in Figure 52. In all cases, diffusivity decreases with increasing crystalline fraction. Maxwell's model[37] was used to extract amorphous and crystalline diffusivity contributions. The Maxwell model is expressed as:

$$D = \frac{D_a}{\phi_a + S_{ac}\phi_c} + 3D_a S_a \phi_c \left[\frac{D_c / D_a / S_{ac} + 2}{D_c / D_a / S_{ac} - 1} - \phi_c \right]^{-1} \tag{5.12}$$

Where: subscripts *a* and *c* refer to amorphous and crystalline phases, *D* represents diffusion of a given phase ($cm^2\ sec^{-1}$), *S* represents penetrant solubility in a given phase ($cc(STP)\ cm^{-3}\ atm^{-1}$), S_{ac} is the ratio between amorphous and crystalline solubility, and ϕ is the volume fraction of a given phase.

There is a definitive effect of size in regards to the diffusion process in this system. Attempts to fit experimental data to classic low molecular weight transport models such as the relationship between diffusivity and critical volume have failed. The diffusion process is still consistent with conceptual interpretation based on a sequence of unit diffusion steps or jumps during which the particle passes over a potential barrier separating one position from the next. Despite inconsistencies in developing an all inclusive molecular model for prediction of diffusion characteristics, suffice to say, the amount of energy required for rearrangement (or "hole" formation) increases as the size and shape of the penetrant molecule increase. While classic approaches were designed with spherical penetrants in mind deviations occur when non-spherical penetrants are considered. In such cases diffusion is perhaps better represented through reptation theory than classical free volume theory based on low molecular weight permeant. Further work is needed to understand this process thoroughly.

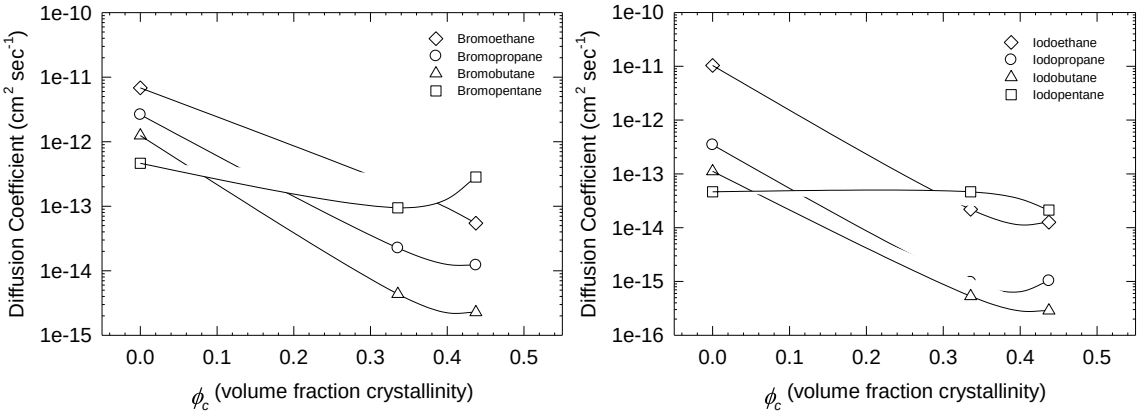

Figure 53. Dependence between diffusion coefficient and volume fraction crystallinity for monosubstituted a) bromo- and b) iodo- linear alkane penetrants.

Diffusivity coefficients plotted with respect to volume fraction for bomo- and iodo-monosubstituted organohalides are shown in Figure 53. It is curious that in both cases pentane-halide show much higher diffusion coefficients in crystalline samples. This is an effect of crystalline cavity exclusion from the diffusion process. Unlike smaller penetrants capable of sorption in the nanoporous host cavity, bromo- and iodo-pentane penetrants follow a more classic response. The effect of densely packed crystalline phase on the solubility and diffusivity has been studied before[38] and it was shown that the crystallite act as inert fillers in which gases can neither dissolve nor diffuse. Most transport in typical semicrystalline polymers take place through the amorphous phase while the crystals are practically impermeable. Michaels[39], in studies of polyethylene with gases and organic vapors, suggested that the crystallites not only act to restrict the segmental motion of the chains, but also the lead to longer and more tortuous diffusion paths. In this respect, factors such as crystallite size, shape and degree of crystallinity will effect a materials overall diffusivity.[40]

Conclusions

Sorption isotherms have been measured for a variety of organic halide penetrants in amorphous atactic polystyrene and semicrystalline δ_e phase syndiotactic polystyrene thin films at 35°C and partial pressures below atmospheric. In all cases, penetrant sorption increases with increasing crystalline fraction, signifying greater loading capacity within the crystalline nanopore. The crystalline phase demonstrates capability to absorb chlorodecane but is impermeable to bromopentane, indicating factors other than size exclusion responsible for crystalline nanoporous cavity capacity. Values of χ were extracted from Flory-Huggins expression and Gee's[18] thermodynamic interpretation of the relationship between solubility and critical temperature. Both methods showed excellent agreement and were used to characterize differences in χ value as it relates to monosubstituted linear organohalides of varying electronegativity in amorphous and δ_e semicrystalline syndiotactic polystyrene thin films. In general, δ_e syndiotactic polystyrene

possesses a greater affinity for organohalides than the amorphous bulk matrix. The nanoporous cavity demonstrates a lower χ value for chloro- substituted penetrants and a progressively higher χ value as you progress from bromo- to iodo- containing organic halides.

A simple and standard diffusion model for sorption experiments traditionally based on the transient pressure decay method developed by Crank[36] was used to process quartz crystal microbalance weight uptake measurements. The time to reach equilibrium sorption in the δ_e phase is greater than that of the amorphous phase, demonstrating a reduced kinetic response intrinsic to the host cavity. Likewise, decreased kinetic response is observed with increasing alkyl chain length and systematically increased monosubstituted halide diameter. Attempts to fit experimental data to classic low molecular weight transport models such as the relationship between diffusivity and critical volume have failed. The diffusion process is still consistent with conceptual interpretation based on a sequence of unit diffusion steps or jumps during which the particle passes over a potential barrier separating one position from the next. Bromo- and iodo-pentane penetrants show much higher diffusion coefficients in crystalline samples, implying crystalline cavity exclusion from the diffusion process.

References

1. Guerra, G.; Milano, V.; Venditto, P.; Musto, C.; De Rosa, C.; Cavallo, L. *Chem. Mater.* **2000,** *12,* 363.

2. Larobina, D.; Sanguigno, L.; Venditto, V.; Guerra, G.; Mensitieri, G. *Polymer* **2004,** *45,* 429-436.

3. Mohri, S.; Amutha, R.; Yamamoto, Y.; Tsujita, Y.; Yoshimizu, H. *J. Polym. Sci., Part B: Polym. Phys.* **2004,** *42,* 238-245.

4. Yamamoto, Y.; Amutharani, D.; Sivakumar, M.; Yoshiharu, T.; Yoshimizu, H. *Desalination* **2002,** *148,* 289-291.

5. Chatani, Y.; Shimane, Y.; Inoue, Y.; Inagaki, T.; Ishioka, T.; Ijitsu, T.; Yukinari, T. *Polymer* **1992,** *33,* 488.

6. Guerra, G.; Vitagliano, V. M.; De Rosa, C.; Petraccone, V.; Corradini, P. *Macromolecules* **1990,** *23,* 1539.

7. Immirzi, A.; de Candian, F.; Iannelli, P.; Vittoria, V.; Zambelli, A. *Makromol. Chem. Rapid Commun.* **1988,** *9,* 761.

8. Puleo, A. C.; Paul, D. R.; Wong, P. K. *Polymer* **1989,** *30,* 1357.

9. Milano, G.; Venditto, V.; Guerra, G.; Cavallo, L.; Ciambelli, P.; Sannino, D. *Chem. Mater.* **2001,** *13,* 1506.

10. Tarallo, O.; Petraccone, V.; Venditto, P.; Guerra, G. *Polymer* **2006,** *47,* 2402.

11. De Rosa, C.; Rizzo, P.; Ruiz de Ballesteros, O.; Petraccone, V.; Guerra, G. *Polymer* **1999,** *40,* 2103.

12. Guerra, G.; Manderkern, L.; Musto, C.; Tavone, S. *Macromolecules* **1998,** *31,* 1329.

13. Felder, R. M.; Huvard, G. S.; Fava, R. A. *In Methods of Experimental Physics: Polymers*; Felder, R. Ed.; Academic Press: New York, 1980; pp 315-377.

14. Stern, S. A.; Trohalaki, S. In *Barrier Polymers and Structures;* Koros, W. J., Ed.; American Chemical Society: Washington DC, 1990.

15. Petropoulos, J. H. In *Polymeric Gas Separation Membranes*; Paul, D. R.; Yampol'skii, Y. P., Eds.; CRC Press: Boca Raton, 1994.

16. Flory, P. J. *J. Chem. Phys.* **1950,** *18,* 108.

17. Singh, A.; Freeman, B. D.; Pinnau, I. *J. Polym. Sci. Part B: Polym. Phys.* **1998,** *36*, 289.

18. Gee, G. *Quarterly Reviews* **1947,** *1*, 265.

19. Van Krevelen, D. In *Properties of Polymers, Their Correlation with Chemical Structure, Their Numerical Estimation and Prediction from Additive Group Contributions*, Elsevier: Amsterdam, 1990.

20. Barrer, R. M.; Skirrow, G. *J. Polymer Sci.* **1948,** *3*, 564.

21. Korosy, F. *Transactions of the Faraday Society* **1937,** *33*, 416.

22. Michaels, A. S.; Bixler, H. J. *J. Polymer Sci.* **1961,** *50*, 393.

23. Serad, F. E.; Freeman, B. D.; Stewart, M. E.; Hill, A. J. *Polymer* **2001,** *42*, 6929.

24. Sauerbrey, G. Z. *Z. Phys.* **1959,** *155*, 206.

25. Chatani, Y.; Inagaki, T.; Shimane, Y.; Shikuma, H. *Polymer* **1993,** *34*, 4841.

26. Chatani, Y.; Shimane, Y.; Inagaki, T.; Ijitsu, T.; Yukinari, T.; Shikuma, H. *Polymer* **1993,** *34*, 1620.

27. Tarallo, O.; Petraccone, V. *Macromol. Chem. Phys.* **2005,** *206*, 672.

28. Manfredi, C.; Del Nobile, M. A.; Mensitieri, G.; Guerra, G.; Rapacciuolo, M. *Polym. Sci., Polym. Phys.* **1997,** *35*, 133.

29. Prabhakar, R. S.; Angelis, M. G.; Sarti, G. C.; Freeman, B. D.; Coughlin, M. C. *Macromolecules* **2005,** *38*, 7043.

30. Ghosal, K.; Chern, R. Y.; Freeman, B. D.; Savariar, R. *J. Polym. Sci., Part B: Polym. Phys.* **1995,** *33*, 657.

31. Kamiya, Y.; Naito, Y.; Terada, K.; Mizoguchi, K.; Tsuboi, A. *Macromolecules* **2000,** *33*, 3111.

32. Toi, K.; Morel, G.; Paul, D. R. *J. Appl. Polym. Sci.* **1982,** *27*, 2997.

33. Ghosal, K.; Freeman, B. D. *Polym. Adv. Tech.* **1994,** *5*, 673.

34. Uda, Y.; Kaneko, F.; Kawaguchi, T. *Macromolecular Rapid Comm.* **2004,** *25*, 1900.

35. Milano, G.; Guerra, G.; Cavallo, L. *Eur. J. Inorg. Chem.* **1998**, *1*, 1513.

36. Crank, J.; Park, G. S. In *Diffusion in Polymers*; Mendi, P. Ed.; Academic Press: London and New York, 1968.

37. Petropoulos, J. H. *J. Polym. Sci, Part B: Polym. Phys.* **1985,** *23,* 1310.

38. Vieth, W. R., In *Diffusion in and through Polymers*, Hanser: Munich, 1991.

39. Michaels, A. S.; Bixler, H. J. *J. Polym. Sci.* **1959,** *36,* 21.

40. Hedenqvist, M.; Gedde, U. W. *Prog. Polym. Sci.* **1996,** *21*, 299-333.

CHAPTER VI

THE STUDY OF OXYGEN BARRIER, FREE VOLUME, COHESIVE ENERGY, AND OTHER RELATED PROPERTIES OF VINYL ALCOHOL COPOLYMERS: EFFECT OF COMPOSITION

Introduction

Ethylene vinyl alcohol (EVOH) copolymers have a broad range of practical applications due to their excellent oxygen barrier properties, processibility and thermal stability.[1, 2] Produced by complete hydrolysis of ethylene vinyl acetate random copolymers, permeability properties of EVOH are mainly dependent on the copolymerization ratio of ethylene and vinyl alcohol, which determines the degree of hydrogen bonding. EVOH copolymers with 20 mol % of ethylene are hygroscopic and lose their practical application, while EVOH copolymers with 25-45mol % ethylene are considered to have superior gas barrier properties and are used commercially. Limited gas permeation through EVOH is attributed to intermolecular and intramolecular cohesive energy.[3] From an academic stand point, this systematically changing fundamental system provides an excellent opportunity to explore classical diffusion models.

The various classical diffusion models can be generally classified as either free-volume or molecular models.[4] Free-volume models are based on the idea that the mobility of both the polymer segment and the penetrant molecule are primarily determined by the quantitative free volume present in the system.[48] A thermodynamic diffusivity coefficient, *D*, is related to the fractional free volume, v_f, by:

$$D = RTA_d e^{\left(\frac{-B_d}{v_f}\right)} \tag{6.1}$$

Where: A_d and B_d are characteristic parameters independent of concentration and temperature.

Molecular models analyze the specific motions of penetrant molecules and polymer chains, together with interaction parameters. Research has shown that the exponential

temperature dependence of diffusion (*D*) is characteristic of an activated process that can be described by the Arrhenius equation:

$$D = D_o e^{\frac{E_a}{RT}} \tag{6.2}$$

Where: D_o is constant for a given series and E_a is the energy of activation. In this model, the diffusion is controlled by overcoming the energy barrier required to jump from one molecular hole to the next. Further explanation through the Brandt model[5] shows that in order for a hole to accept a small molecule, both the energy required for the polymer backbone to accept a permeant molecule, based on polymer backbone rigidity and van der Waals interactions, and the repulsion forces between adjacent polymeric chains affect the energy of activation. In 1954, Meares did work on the diffusion of penetrant gasses He and Ar through polyvinyl acetate (PVA) both above and below the glass transition temperature, T_g.[6] Through this work he found that there was a linear relationship between E_a and the square of the penetrant diameter. The relationship between the square of the permeant diameter and E_a led Meares to the conclusion that the driving force for diffusion is the energy required to create a hole capable of housing the penetrant, allowing for a jump to take place. In this regard, E_a has been related to diffusivity through the Meare's equation:

$$E_a = 0.25\pi N_a \sigma_A^2 \lambda_A CED \tag{6.3}$$

Where: such energy is dependent upon the kinetic size of the permeant gas (σ_A), jump length from one hole to the next (λ_A), and cohesive energy density (*CED*) of the polymer matrix.

From a fundamental standpoint based on classical models, diffusion is directly proportional to either the fractional free volume or cohesive energy density in the system. Ito et al. reported that the linear correlation obtained between the Log of oxygen permeability and reciprocal hole free volume for EVOH copolymers is diffusion controlled and strictly follows free volume theory.[7] Though the free volume approach can accurately define the changes in permeability, due in part to the magnitude of the diffusion variable, structural effects resulting in

changes to the solubility coefficient cannot be ignored. Furthermore, it is prudent to test this approach at different temperatures and to model penetrant diffusion on the basis of a molecular interpretation. Specifically, efforts will be made to (1) relate diffusion directly to CED to better understand the physical parameters responsible for changes in diffusion and (2) attempt to uncover the relation between diffusion models based on free volume and molecular motions respectively.

Experimental

Materials and Sample Preparation

Ethylene vinyl alcohol (EVOH) copolymers with various ethylene contents (0, 27, 32, 38, 44, 48, 60, 75, 82, 95 and 100 mol %), were used in this study. Materials are labeled as EVOHxx where xx represents mol% ethylene in the copolymer. Low density polyethylene, LDPE, was used for the ethylene control sample. EVOH copolymers containing 0-60 mol % are commercial products and were generously provided by EVALCA while EHOH75, 82 and 95 were prepared in the lab via saponification of the corresponding ethylene vinyl acetate (EVA) copolymers following the procedure described in details elsewhere.[89] Briefly, the corresponding EVAxx copolymer was first added to a boiling mixture of benzene and 2-propanol at 84^{o}C, then potassium hydroxide was added in excess of two to four times the stoichiometric amount followed by vigorous agitation. Saponification reaction was carried out under reflux for 72 hours. The product, EVOH copolymer, was collected after precipitation in pure 2-propanol followed by washing of the product several times with distilled water. Washed polymer then was dried in a vacuum oven at 60^{o}C for 24 hours. Thin films of EVOH copolymers were prepared via compression molding. After being dried in vacuum at 60^{o}C for at least 24 hours, the copolymers, some of which were available as pellets and some as powders, were placed in the 165mm x 165mm cavity of 200 μm thick spacer and sandwiched between polished steel plates covered with thin Kapton® films. The plates were placed in the press preheated at a temperature 30^{o}C above

the corresponding copolymer melting temperature and held without pressure for 15 minutes. Then the pressure was subsequently increased to 25,000 psi, held for 15 minutes and released. After the pressure was released the plates were quenched into the ice-water mixture. To prepare films with higher crystallinity (these samples are further referred in the text as isothermally crystallized or EVOH-IC), the plates after the mold pressure was released were instantly transferred into preset at 30^{o}C below the corresponding EVOH copolymer melting temperature convection oven and annealed there for one hour followed by quenching into the ice-water mixture. All films were dried in vacuum oven and stored in dessicator before the measurements were conducted.

Measurements

The crystalline structure of EVOH copolymers and the amount of crystallinity were determined by wide-angle X-ray diffraction (WAXD). WAXD measurements were conducted at room temperature with a Rigaku Ultima III X-ray spectrometer operating in reflection mode using nickel filtered CuKα radiation (wavelength 1.542 Å). Powder samples were scanned within scattering angle 2θ from 5 to 40^{o}. PeakFit automated nonlinear peak separation and analysis software was employed to deconvolute the crystalline reflections and amorphous halo. The weight fraction of crystallinity, ω_c, was determined from the corresponding integrated areas under the crystalline reflections and the amorphous halo.

Density was measured using a density gradient column constructed from a solution of toluene and carbon tetrachloride in accordance with ASTM-D Standard 1505 Method B. It was confirmed that the selected combination of solvents does not lead to measurable swelling of EVOH copolymers. The column was calibrated with glass floats of known density. Small film pieces (~25mm^2) were cut and placed in the graduate column and allowed to equilibrate for 2 hours before the measurements were taken. Experimental error of density measurements did not exceed ± 0.0004 g/cm^{-3}.

Using a Bruker Tensor 37 FTIR spectrometer, FTIR spectra were recorded. A total of 64 scans at a resolution of 4 cm^{-1} were recorded at room temperature under nitrogen purge and averaged. Spectra were collected in the mid range from 400 to 4000 cm^{-1}.

Differential scanning calorimetry (DSC) was used to measure glass transition temperature (T_g). The measurements were carried out under nitrogen purge from -30^oC to 240^oC at a heating rate of 10^oC min^{-1} using a Perkin-Elmer DSC 7. The midpoint of the corresponding C_p transition was used to define the glass transition temperature (T_g). Second heating scans have been used.

Positron annihilation lifetime spectroscopy (PALS) was used to probe free volume of EVOH copolymers at various temperatures. PALS measurements were performed using custom built instrument available in our lab which consists of BaF_2 scintillation crystals coupled with photomultiplier tube for gamma ray detection a fast-fast coincidence system[10] (time resolution 220 ps). Standard software package PATFIT was used to process the data and to extract mean ortho-positronium (o-Ps) lifetimes and o-Ps decay intensities. The PALS spectra were tested against three- and four-component fits however optimal fits were obtained to three components with variances smaller than 1.1. PALS methodology is described in details elsewhere.[11,12]

Oxygen flux, *J(t)* at various temperatures and 0% of relative humidity was measured using MOCON OX-TRAN® 2/21 commercially built diffusion apparatus. This instrument employs continuous flow cell method (ASTM D3885-81) using nitrogen as a carrier gas. Oxygen partial pressure 1atm across the film thickness was maintained. Oxygen permeability in the temperature interval from 5^oC till 40^oC was measured using a built-in diffusion cell and above 40^oC using a remote cell that was placed in the convection oven preset at given temperature. The temperature during permeation measurements was controlled within ± 0.5^oC. All samples were preconditioned in a vacuum dessicator for at least 24 hours and rapidly transferred to the test cell to minimize humidity exposure. Permeability and diffusion coefficient were obtained by performing a two parametric least square fit of the experimental flux data to the solution of Fick's second law:

$$J(t) = \frac{Pp}{l}\left[1 + 2\sum_{n=1}^{\infty}(-1)^n \exp(-D\pi^2 n^2 t / l^2)\right] \tag{6.4}$$

Where: P is the permeability coefficient, D is the diffusion coefficient, l is the specimen thickness determined by micrometer, and p is oxygen partial pressure difference across the film. The solubility S was obtained from the relationship $P=DS$.

Results

FTIR Characterization and Study of Hydrogen Bonding

Primary interest in this work was the establishment of a link between hydrogen bonding and the transport of small molecules. In this respect, infrared spectroscopy (FTIR) has been traditionally used to characterize H-bonding.

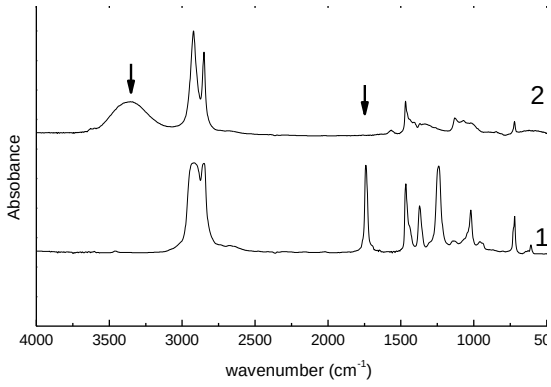

Figure 54. FTIR spectra of EVAc75 copolymer (1) before and (2) after saponification.

Figure 54 shows a typical mid FTIR spectra in the range from 400 to 4000 cm^{-1} for EVAc75 copolymer before and after saponification. The most noticeable difference between these two spectra is the complete disappearance for EVAc75 copolymer, a fairly narrow band situated at 1710 cm^{-1} attributed to stretching of carbonyl groups, and the appearance for EVOH copolymer a very broad peak situated at about 3300 cm^{-1} attributed to H-bonded (OH-OH) hydroxyl groups. [13] This implies that within the detection limits of mid FTIR, all vinyl acetate groups of EVAc75 copolymers have been hydrolyzed.

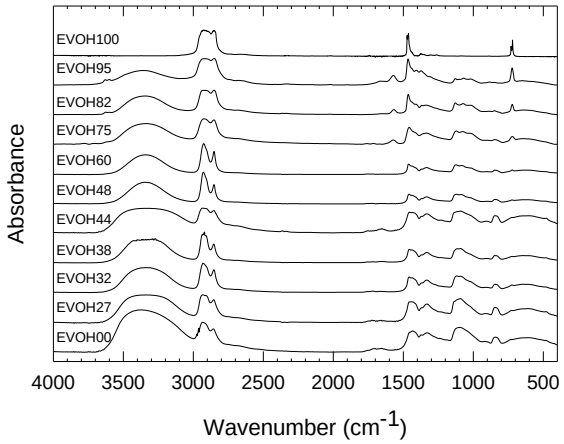

Figure 55. FTIR spectra for the EVOH copolymers used in this study.

Room temperature FTIR spectra of EVOH copolymers with different vinyl alcohol content are depicted in Figure 55. The area of interest is the stretching vibration of intermolecular and intramolecular hydroxyl groups. A large, broad peak centered at about 3,300 cm^{-1} has been observed for all tested samples, except for the LDPE control, and assigned to hydrogen bonded (HB) hydroxyl groups.[13] The peak is broad due to a distribution of hydrogen bonded -OH associations ranging from dimers to multimers. As expected, both the width and the intensity of this peak decreased gradually with decreasing vinyl alcohol content.[14] In addition to the above discussed 3300 cm^{-1} peak, specimens with larger ethylene content i.e. EVOH75, EVOH82 and EVOH95, exhibited a new band situated at about 3600 cm^{-1} appearing in the corresponding spectra in the form of a tiny shoulder. This band was attributed to stretching vibrations of free hydroxyl groups unaffected by hydrogen bonding.[15] Although, as evident from the figure, free hydroxyl group's band intensity increased progressively with increasing of ethylene content, this peak still remained hardly detectable as compared to the one associated with hydrogen bonded hydroxyls even for EVOH95 which exhibited the largest ethylene content. This implies that the amount of free, unassociated hydroxyls in EVOH copolymers is always very small. This fact can be attributed to remarkable backbone flexibility of all EVOH copolymers so

the hydroxyl groups practically always can find each other and form hydrogen bonded associations.[16]

Solid State Crystalline Structure

The primarily objectives of this section were probing of the crystalline structure of the EVOH copolymers and determination of the amount of crystallinity. Also the density of amorphous phase for EVOH copolymers was determined.

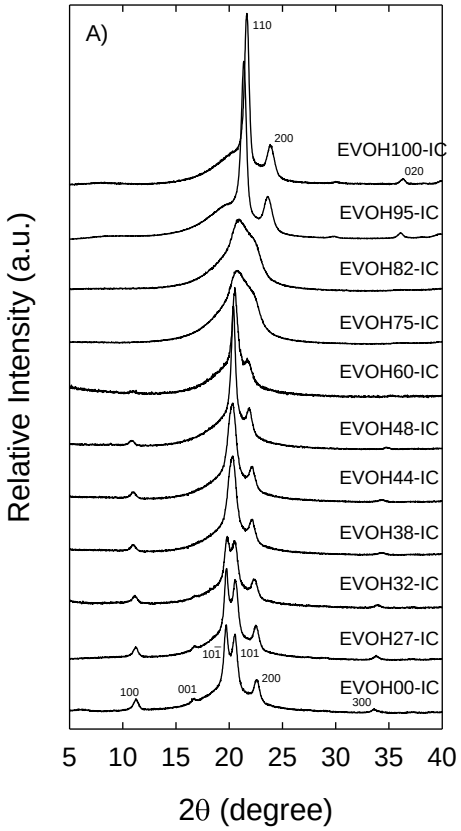

Figure 56. WAXD of isothermally crystallized from the melt EVOH samples.

Figure 56 shows wide angle X-ray diffraction (WAXD) data recorded for isothermally crystallized EVOH-IC copolymers including pure low density polyethylene (EVOH100) and polyvinyl alcohol (EVOH00) controls. The peaks were assigned and the crystalline structure was identified as reported previously by Takahashi et al.[17,18,19,20,21,22,23,24]. The crystalline structure for EVOH0 and EVOH100 controls exhibited monoclinic and orthorhombic lattices respectively with crystalline reflections identified and labeled in Figure 56 as follows: PVA 2Θ =11.1(100),

17.3(001), 19($10\bar{1}$), 20.6(101), 22.7(200) and 33.8(300); LDPE 2Θ = 20.1 (100), 24.2(200) and 35.4 (020)[25,26,27,28]. EVOH 27, 32, 38, 44, 48, and 60 exhibited monoclinic crystalline lattice. Reflections 100, 200, and 300 can be seen for all copolymers exhibiting monoclinic structure. Reflection 001 was only observed for EVOH 27 and 32. Reflections $10\bar{1}$ and 101can only be individually resolved for EVOH 27 and 32, while they overlapped forming one peak as polyethylene content increased. The diffractograms for EVOH 75 and 82 consisting of two or more broad overlapping peaks were assigned to pseudo-hexagonal crystalline lattice the nature of which has been previously discussed.[29] Finally, EVOH 95 displayed X-ray diffractogram very similar to that of EVOH100 implying a well-defined orthorhombic lattice.

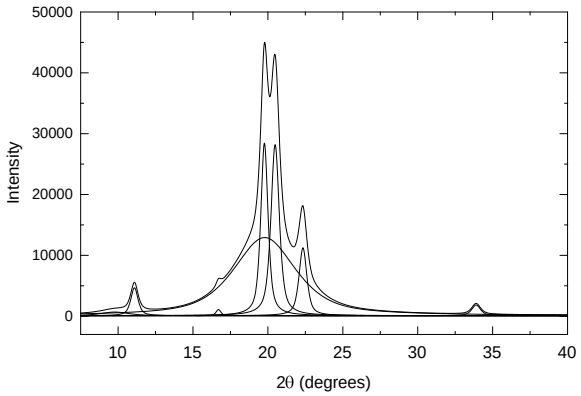

Figure 57. Representative amorphous and crystalline component deconvolution of EVOH32.

Standard PeakFit commercially available software was employed to resolve crystalline peaks and amorphous halo. An example of this fit for EVOH32 is shown in Figure 57. The linear fit was first applied to the background radiation and after the background was subtracted standard Gaussian-Lorentzian Cross Product non-linear fit was applied to all of the crystalline reflections and the amorphous halo. In this fit, the angular positions of the corresponding crystalline peaks (Takahashi[13] assignments have been used) were kept fixed while the angular position of amorphous halo for various copolymers was allowed to vary as this information was not available. The fits were fairly good (R^2=0.997). Amorphous halos determined for

isothermally crystallized EVOH copolymers, assuming that they changed negligibly after the copolymers have been quenched, were used to resolve the scattering intensity associated with the crystalline I_c and amorphous phases I_a for quenched samples as shown in Figure 57. The weight crystallinity, w_c, for both isothermally crystallized and quenched samples was determined according as follows $w_c = I_c/(I_c + I_a)$. The amorphous density, ρ_a, was determined assuming the two phase model as follows $\rho_a = \rho_c\rho \cdot (1 - w_c)/(\rho_c - \rho w_c)$ where ρ is the sample density measured experimentally and ρ_c is the crystalline density calculated for EVOH copolymers using WAXD data by Takahashi et al. The crystalline density for EVOH27, not reported by Takahashi et al.[13], was obtained by linear extrapolation.

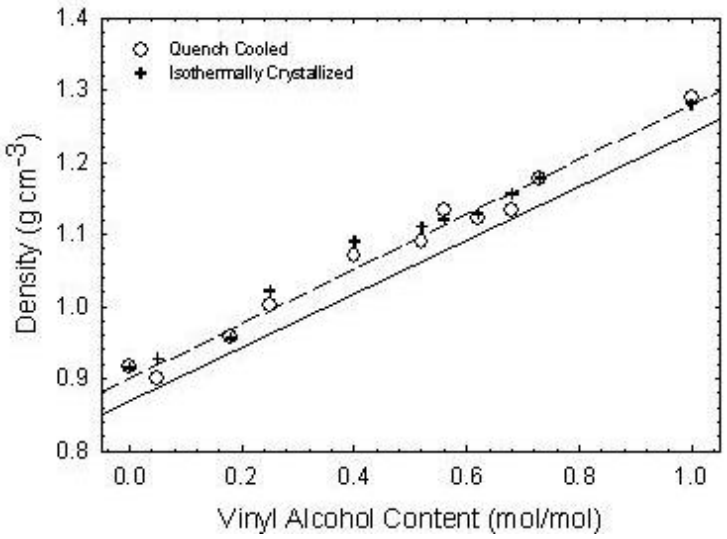

Figure 58. Change in amorphous density with respect to vinyl alcohol content for quenched (o) and isothermally crystallized (+) samples. Solid line represents theoretical density from group contributions.[30]

A plot of experimentally measured amorphous density of EVOH copolymers as a function of copolymer vinyl alcohol content is shown for both isothermally crystallized and quenched EVOH samples in Figure 58 (experimental points with dotted line representing least square fit). Solid line is the prediction based on van Krevelen group contribution method which is based on linear correlation of bulk densities obtained for a broad range of amorphous polymers in

both rubbery and the glassy state and their van der Waals volume.[30] The results for quenched and isothermally crystallized systems fell inside the limits (±0.02 g/cm^3) of the same linear trend which was nearly parallel to that predicted via group contributions. Experimentally determined densities however were systematically larger by about 0.03-0.04 g/cm^3. The reason for this difference is not exactly clear. One possibility is that WAXD is known to underestimate weight crystallinity due to fairly small size of polymer crystals in general and also their imperfection.

Computer Modeling of Cohesive Energy Density

A quantitative measure of a molecule's intermolecular forces in the polymer can be expressed through cohesive energy, or when normalized per volume, cohesive energy density CED. The cohesive energy density may be divided into three additive parts, corresponding to the three types of interaction forces, i.e. dispersion, polar and hydrogen bonding, and it is conveniently presented in terms of solubility parameter δ, $CED = \delta^2 = \delta_d^2 + \delta_p^2 + \delta_h^2$. Experimentally, the solubility parameter and its dispersion, polar and hydrogen bonding contributions are most often measured by dissolving presumably amorphous polymer in series of solvents and building the solubility sphere in accordance with Hansen method.[30] This process, however, proves difficult when dealing with semicrystalline copolymers, and especially when comonomers are very dissimilar like in the case of crystallizable EVOH copolymers. In the current research we employ the Hoy additive group contribution method along with molecular dynamic simulation for determining CED and solubility parameter components.[30] Computer simulation is a new powerful tool which potentially can be used for this kind of applications.

Bulk structure of EVOH copolymers was generated and simulated by means of Accelrys Material Studio® (Insight II-Discover) software using a COMPASS force field. Each amorphous cell consisted of 1 chain possessing 600 monomer units. Vinyl alcohol and ethylene monomer units were statistically integrated into the chain representing various EVOH copolymer compositions. A molecular mechanics method was employed using in which nuclei motion was

governed by means of a COMPASS "force field," representing the equilibrium time average effects of the electrons. The force field is represented in terms of bond stretching/compression, valence angle deformation, torsion or rotation about bonds, and non-bonded interactions. The force field approach allows for fast computational times of large systems.

In order to obtain an equilibrated amorphous cell at room temperature a series of dynamic simulations were conducted in which number of atoms, temperature, pressure, or volume were held constant while molecular atoms underwent energy minimization. A summary of the amorphous cell equilibration parameters are shown in Table 5. An initial density of 0.6 g/cm^3 was used to allow for a large degree of mobility in the initial energy minimization. Temperature was varied from 650K to 298K and pressure was varied from 0.2 GPa to 0.0001013 GPa. Once room temperature conditions were reached volume of the amorphous cell was controlled and correlated to experimental density.

Table 5

Molecular Dynamic Simulation Parameters for Obtaining Equilibrium Amorphous Cell

Constant	Temperature (K)	Pressure (GPa)	Time (ps)
NVT	650	variable	30
NPT	650	0.1	50
NVT	500	variable	20
NPT	500	0.25	30
NVT	450	variable	20
NPT	450	0.5	30
NVT	298	variable	20
NPT	298	0.0001013	60

Note. N = # of atoms, V = volume, P = pressure, and T = temperature

In order to obtain the cohesive energy density within the minimized amorphous cell the total potential energy was established for each copolymer. The total potential energy is the sum of inter and intra molecular interactions acting upon the polymeric chain. Therefore the total

potential energy minus the sum of the intramolecular interactions, including bond energy, angle energy, torsion energy etc., results in the overall cohesive energy of the system.

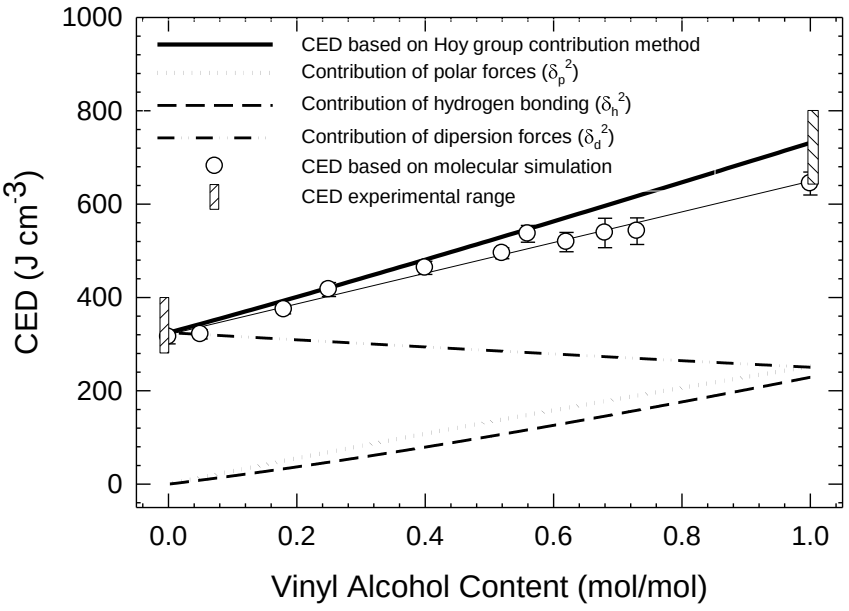

Figure 59. Cohesive energy density versus vinyl alcohol content for molecular simulation (–) and Hoy method predictions (Solid line). Experimental CED range is shown with a hatched box for LDPE and PVA.

In Figure 59, cohesive energy density obtained from group contribution method and molecular dynamic simulation is shown with respect to vinyl alcohol content. As shown by the hashed CED experimental range obtained from literature, both methods accurately predict CED. Furthermore, individual solubility parameters from which group contribution method is based indicate that hydrogen bonding and polar forces dominate CED in this system. Therefore, it is reasonable that CED finds it physical dependence in hydroxyl hydrogen bonding moiety.

Positron Annihilation Lifetime Spectroscopy

The free volume hole radius, *R*, was calculated from the ortho-positronium, o-Ps, lifetime, τ_3, using the semi-empirical equation:[31,32]

$$\tau_3 = \frac{1}{2}\left[1 - \frac{R}{R+\Delta R} + \frac{1}{2\pi}\sin\left(\frac{2\pi R}{R+\Delta R}\right)\right]^{-1} \text{ns} \qquad (6.5)$$

Where: ΔR has been empirically determined to be ΔR=0.1656 nm by fitting the above equation to o-Ps annihilation data for molecular solids of known pore sizes.

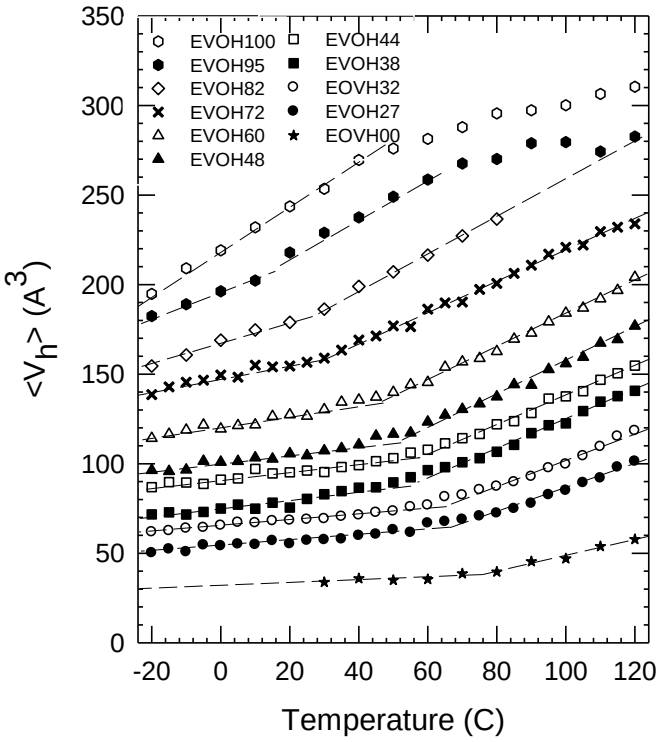

Figure 60. Temperature dependence of average hole free volume, $<V_h>$, with respect to vinyl alcohol content. For clarity the data are shift on the vertical scale by 10 $Å^3$ to each other.

Temperature dependence of the average hole free volume in EVOH copolymers is shown in Figure 60. Uncertainties of the experiments are smaller than the size of the data points. Increase in the average hole free volume with temperature mirrors the thermal expansion of free volume. Glass transition was obtained from the intersection of two linear regressions indicative of thermal expansion in the glassy and rubbery state respectively. Additionally, mean hole free volume decreases with increasing vinyl alcohol content, indicative of a higher amorphous packing density.

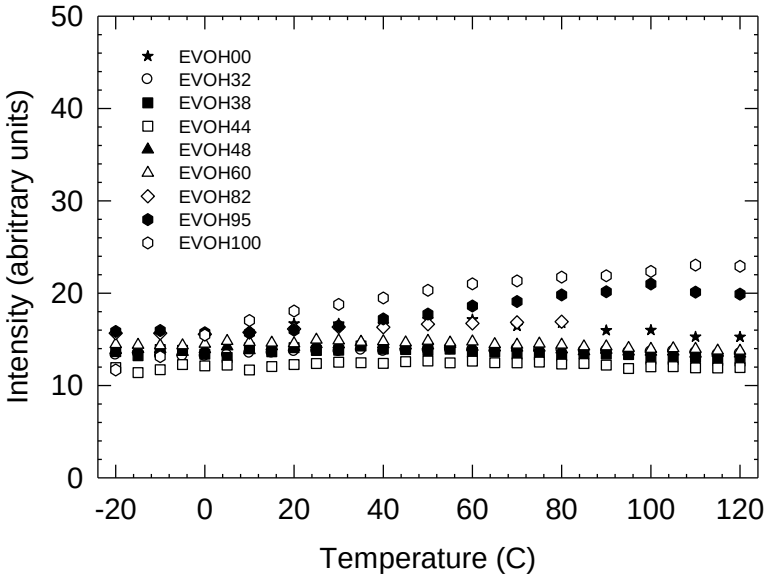

Figure 61. Change in positronium intensity with respect to temperature and vinyl alcohol content.

Minimal change in intensity was observed with varying copolymer composition, indicated in Figure 61. The only deviation is observed for the pure polyethylene and EVOH95 samples. This can be explained through molecular motions associated with the glass transition. Considering motion modes of molecular segments, the thermal expansion process can be expressed as a pre-glass-transition stage just prior to glass transition and a post-glass-transition stage.[33,41] The latter deals with short-range diffusional motions which permit large segments to undergo conformational reordering, this generates new free-volume holes with the same average size. In our case temperature measurements demonstrate this phenomenon as an apparent increase in intensity. As researchers have shown that intensity can be directly related to the free volume hole density through the use of a correctional factor, it is assumed that the population of free volume holes with vinyl alcohol content greater than 5% remains constant over all compositions.

Thermal Transitions

Glass transition temperature was calculated from DSC and PALS. A linear correlation in glass transition temperature, T_g, with increasing vinyl alcohol concentration is shown in Figure 62.

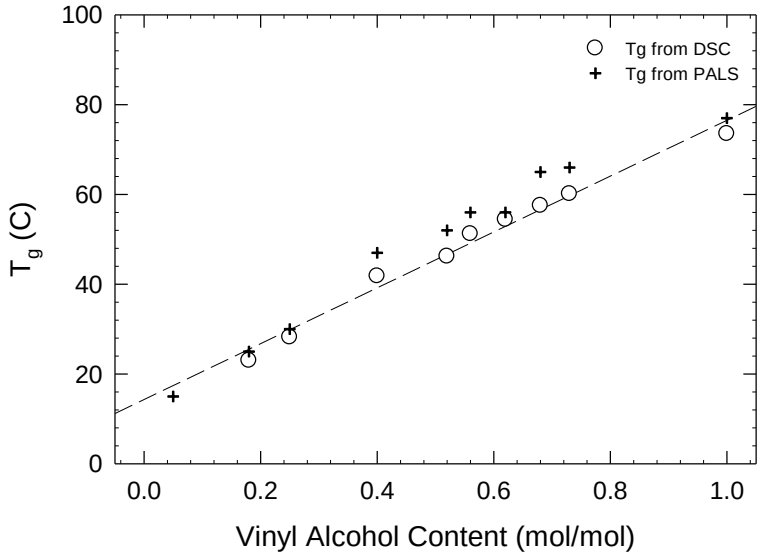

Figure 62. Glass transition temperature dependence on EVOH copolymer composition.

Structural units having higher non covalent bonds including specific and secondary interactions generally confer higher value of T_g in polymers. In the current research an increased population of hydrogen bonding moiety with vinyl alcohol content inhibits the onset of long range segmental motion, i.e. T_g. Glass transitions for EVOH95 and LDPE could not be measured directly in our system due to limited sensitivity of the instrument in detecting change in specific heat capacity, ΔCp, at glass transition. However, relaxations of LDPE have been extensively investigated by many researchers.[34,35,36,37] In particular, the glass transition was studied by X-ray diffraction,[38] Raman spectroscopy,[39] DSC using long alkyl chain as a model of PE,[39] dynamic mechanical measurement, ESR,[40] positron annihilation measurement,[41] dielectric[42] and fluorescent probe measurements.[43] It has been found that three relaxation processes exist in PE all possessing fundamental characteristics of a glass transition. The nature of these transitions is however beyond the scope of the current work. In 1973 Davis and Eby[44] compiled the

experimental distribution of 50 reports on PE relaxation phenomenon. These results illustrate an α relaxation at 150±10, β at 195±10, and a γ relaxation present at 245±15˚K. If we consider the linear relationship in our system between T_g and vinyl alcohol content to hold true at low vinyl alcohol content then extrapolation to 0% vinyl alcohol results in a glass transition of 287K. In this case, further argument is made in justifying the γ relaxation as a true glass transition. It should be noted that the γ relaxation associated with T_g is greatly affected by crystallinity and molecular weight, and is believed responsible for the relative shift to higher apparent relaxation temperature observed here.

Oxygen Transport

Typical experimental curves in Figure 63 describe the oxygen flux, J(t), through EVOH27 and LDPE. To make possible comparisons among specimens that varied in thickness, the flux curves were normalized to a film thickness of 100 μm. The initial increase in oxygen flux reflected typical non steady-state diffusion.

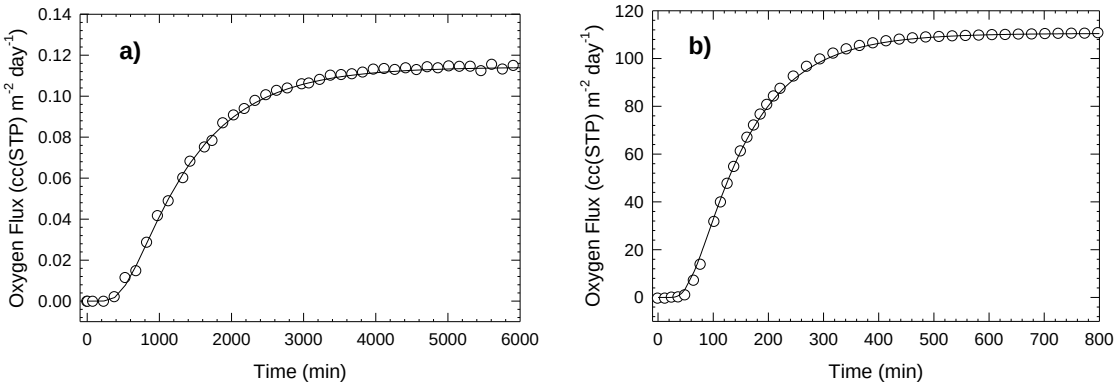

Figure 63. Experimental oxygen flux curves for (a) EVOH27 and (b) EVOH100 normalized to a thickness of 100 μm and fit to eq 6.4.

Non-steady state flux was controlled mainly by the diffusivity, *D*. As the permeant concentration in the specimen reached a constant distribution, the flux reached a steady-state value, J_o. This value, normalized to the film thickness, *l*, and oxygen partial pressure drop across the film, p, define the permeability, $P=J_o l/p$. *P* and *D* were obtained by performing a two-

parametric least square fit of the experimental flux data to eq. 6.4. The solubility, *S*, is then obtained from the relationship $P=DS$. Fitting curves are included with the experimental points in Figure 63. Accurate film thickness measurements are essential in this calculation. Average bulk thickness of each specimen was determined as $l=W/A\rho$, where W is the sample weight, *A* is the sample area, and ρ is the density.[45] The fit was equally good for all the experiments in the study.

In Figure 64 oxygen permeability is plotted as a function of copolymer composition for temperatures ranging from -5 to 45C. As observed, a linear correlation exists over all temperatures resulting in a decreased permeability with increasing vinyl alcohol content, extrapolating to a value of 8.1×10^{-6} cc(STP) cm m^{-2} day^{-1} atm^{-1} for dry polyvinyl alcohol at 23C. Permeability changes by five orders of magnitude from 16.687 to 0.00029 cc(STP) cm m^{-2} day^{-1} atm^{-1} for LDPE and EVOH27 at 23C respectively. In Figure 65 the diffusion coefficient is plotted as a function of copolymer composition over all temperatures. As in the case of permeability, diffusivity decreased in a linear fashion with increasing vinyl alcohol content over approximately 5 orders of magnitude from 40.9 to 0.0012 cm^2 s^{-1} for LDPE and EVOH27 respectively at 23C. It is apparent from the experimental trends that permeability is controlled primarily through diffusion over all copolymer compositions, owing to a comparatively weak decline in solubility.

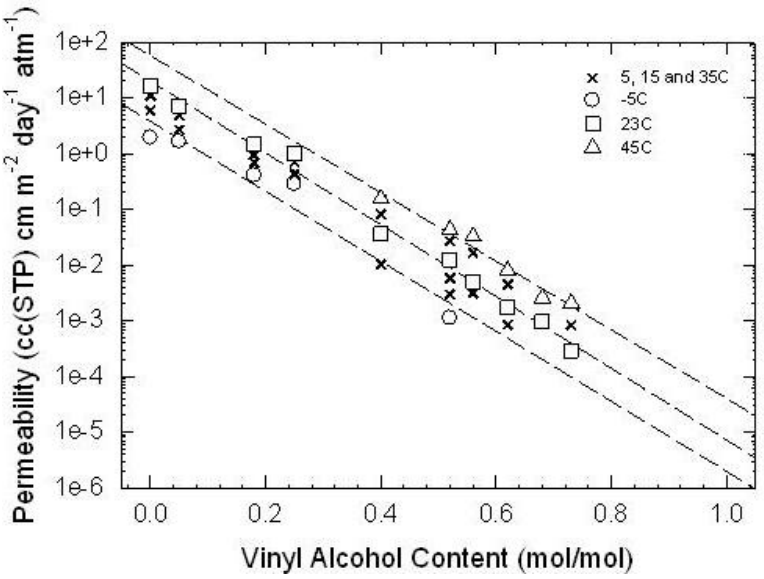

Figure 64. Change in permeability with respect to copolymer composition as it relates to temperature.

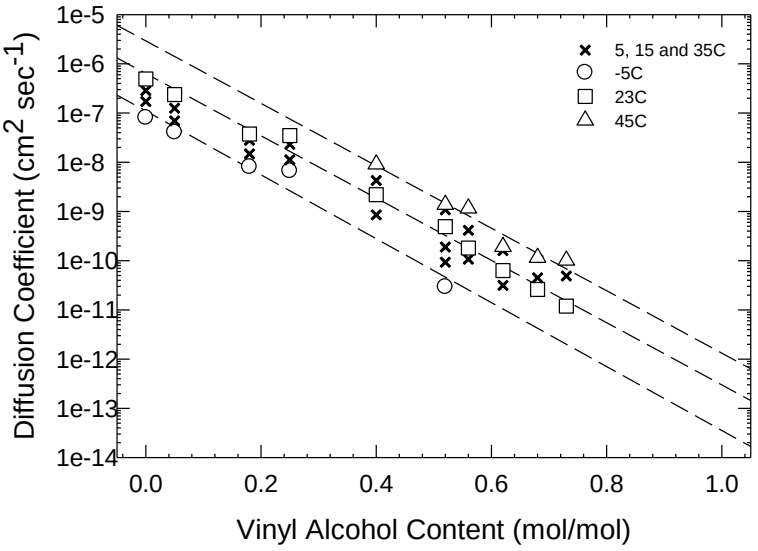

Figure 65. Change in diffusion with respect to copolymer composition as it relates to original temperature.

Though diffusion can accurately define changes in permeability, due to the magnitude of the diffusion variable in our system, structural effects resulting in changes in the solubility coefficient cannot be ignored. The slight decrease in solubility with increasing vinyl alcohol content shown in Figure 66 can be attributed to an increased amorphous phase density.

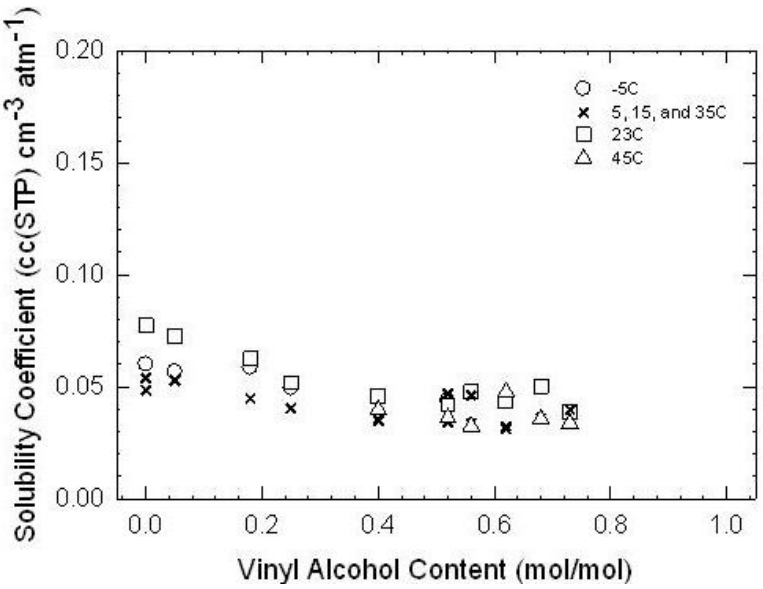

Figure 66. Change in solubility with respect to copolymer composition as it relates to original temperature.

Similar results were shown in a study of PET and PET copolymers where increased gas solubility was attributed to a decrease in density of the amorphous phase termed "de-densification."[46,45,47] Increasing amorphous density with increasing vinyl alcohol content is a result of inter and intra molecular hydrogen bonding escalating the association energies within the polymer chains. Therefore, "de-densification" due to reduced vinyl alcohol content results in increased average hole free volume size and a greater concentration of gas molecules in the polymer, a measure of solubility coefficient.

Discussion

As the diffusion coefficient was shown dependent upon vinyl alcohol content several theoretical approaches were considered. Fujita[48] applied the free volume theory to relate the thermodynamic diffusion coefficient to fractional free volume of concentrated polymer solutions and rubbery polymers, yielding:

$$D = A_d \exp\left(\frac{B_d \overline{V_h^*}}{\upsilon_f}\right) \tag{6.9}$$

Where: A_d and B_d depend on penetrant size and shape, $\overline{V_h^*}$ represents the volume of one mol of holes of the minimum size required for a diffusion jump, and υ_f is the fractional free volume. It has already been shown in Figure 63 that ortho positronium intensity is constant across all copolymer compositions. Intensity is often related to the population of free volume voids present in the system. Therefore, we can assume that the number of holes is constant in our system. Furthermore, as υ_f is the product of the number of holes and average hole free volume we can combine $\overline{V_h^*}$ and the number of holes into the B_d term and demonstrate a direct correlation to reciprocal average hole free volume. In Figure 67 the logarithm of EVOH copolymer diffusion coefficients are plotted versus their reciprocal average hole free volume. A linear relation suggests the classical correlation between diffusion coefficient and free volume was accurately predicted by the free volume model.

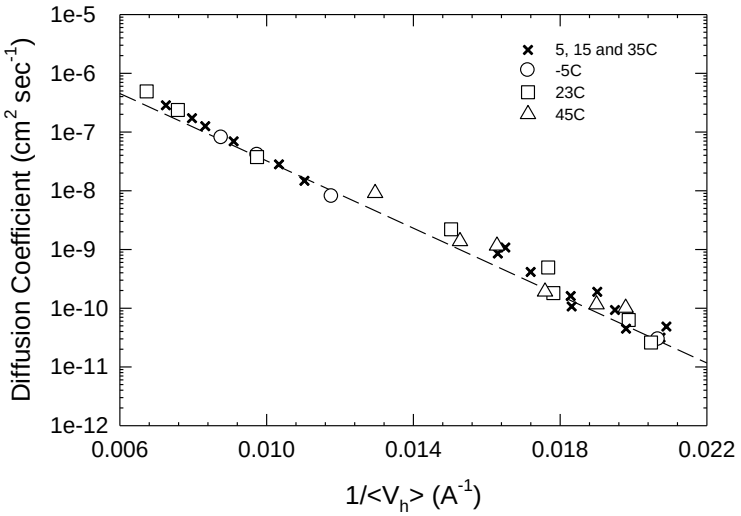

Figure 67. Change in diffusion coefficient from -5 to 45 C with respect to reciprocal average hole free volume.

Two primary factors control the free volume within a polymeric material; the attractive forces between the chain backbones referred to as cohesive energy and the backbone chain rigidity. The pseudo second order transition temperature or glass transition of a polymer is generally regarded as a measure of the chain molecules flexibility. As a polymer is cooled to the

glass transition the rotation of its atoms becomes inhibited. Therefore, at glass transition the polymer atoms lack sufficient rotational energy to overcome intermolecular forces holding the molecules together. Hayes[49] found for a series of polymers that a relation exists which directly correlates intermolecular forces in the form of cohesive energy density with the glass transition temperature. This can be expressed as:

$$CED = 0.5nRT_g + C \tag{6.10}$$

In this expression, *CED* represents the intermolecular forces holding the molecules together and $0.5nRT_g$ represents the atoms rotational energy where *n* is a number analogous to the degrees of freedom in expressions of kinetic energy and *C* is a constant which includes molecular weight and rate effects. A plot of EVOH copolymer cohesive energy density versus T_g is shown in Figure 68. The linear correlation demonstrates that the backbone chain stiffness, relating to the number of degrees of freedom in the molecular atoms, is constant across all compositions. If we consider intrinsic chain mobility to be constant across all compositions then it can be inferred that hydrogen bonding and polar interactions are predominant in determining phase changes in our system and that a measure of this response is possible through CED.

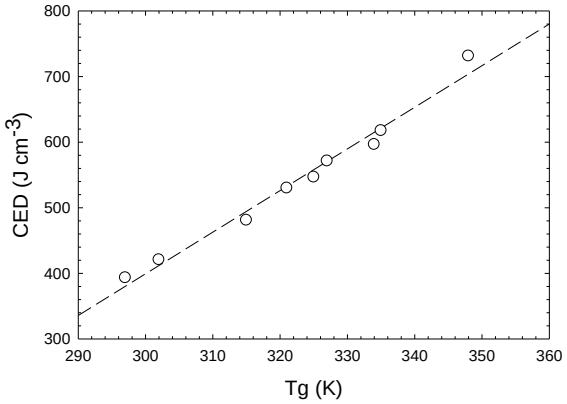

Figure 68. EVOH copolymer CED versus glass transition temperature.

Furthermore, it can be inferred that the primary compositional dependence controlling free volume is not a change in chain backbone rigidity but rather cohesive energy in this system. It is important to point out that this relation is only applicable to systems possessing similar chain

rigidity and will not hold for a broad range of materials. In Figure 69 the logarithm of diffusion coefficients of EVOH copolymer compositions are plotted versus their cohesive energy density over temperature. A linear relationship indicates a correlation between CED and diffusion. Therefore, both free volume and molecular models can accurately predict diffusion kinetics of small molecules over a broad temperature range in this system.

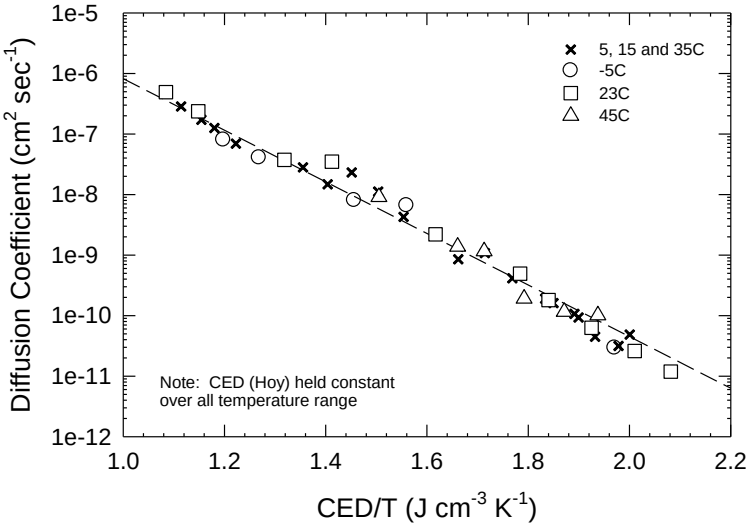

Figure 69. Change in diffusion coefficient with respect to cohesive energy density over temperature.

Free Volume for Predicting Activation Energy

Given a direct relationship between average hole free volume and cohesive energy density it is possible to predict transport over an extended temperature range directly from PALS average hole free volume data. Specifically, relating hole free volume to cohesive energy density allows for determination of energy of activation, the controlling factor in temperature measurements.

Assuming Arrhenius relation, experimental activation energy of diffusion, E_a, was obtained through a linear regression involving natural log of diffusion coefficient versus reciprocal temperature:

$$LnD = A - \frac{E_a}{RT} \tag{6.11}$$

Data is shown in Figure 70 and showed excellent agreement over the entire experimental temperature range.

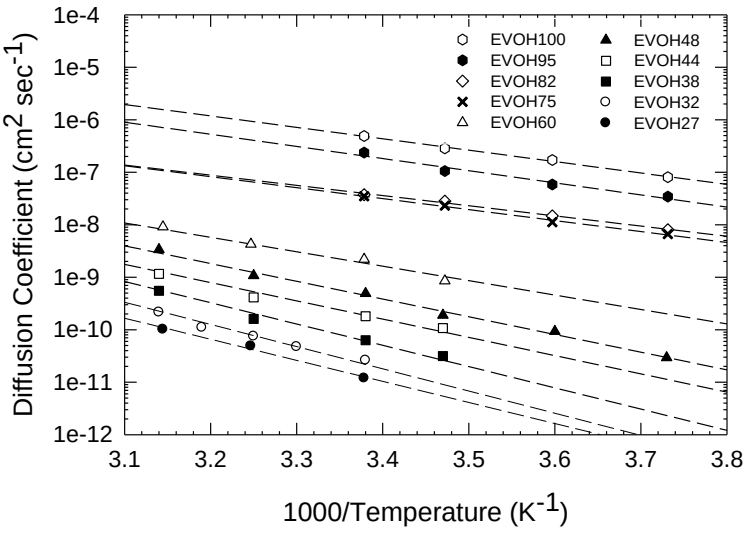

Figure 70. Diffusion coefficient variation with reciprocal temperature in EVOH copolymers. Dashed lines represent best fit linear regressions.

Along with this traditional method, development of average hole free volume with respect to diffusion coefficients permits calculation of diffusion coefficient temperature dependence over a broad range. This is brought about through combination of the linear dependence of diffusion coefficient verses reciprocal average hole free volume,

$$LnD = A'' - \frac{B''}{\langle V_h \rangle} \tag{6.12}$$

where *A"* and *B"* are -10.5 and -653.8 respectively, and the linear dependence of $1/\langle V_h \rangle$ verses 1/T:

$$\frac{1}{\langle V_h \rangle} = A' - \frac{B'}{T} \tag{6.13}$$

Where: *A'* and *B'* are dependent upon EVOH copolymer composition. If we substitute equation 6.13 into equation 6.12, a predictive equation in the form of the Arrhenius equation is obtained:

$$LnD = A'' - B''A' - \frac{B''B'}{T} \tag{6.14}$$

Where: $E_a = RB''B'$ and $A = A'' - B''B'$. Direct traditional and predicted approaches for E_a are shown below in Figure 71. Error bars are indicative of the E_a difference between the glassy and rubbery states.

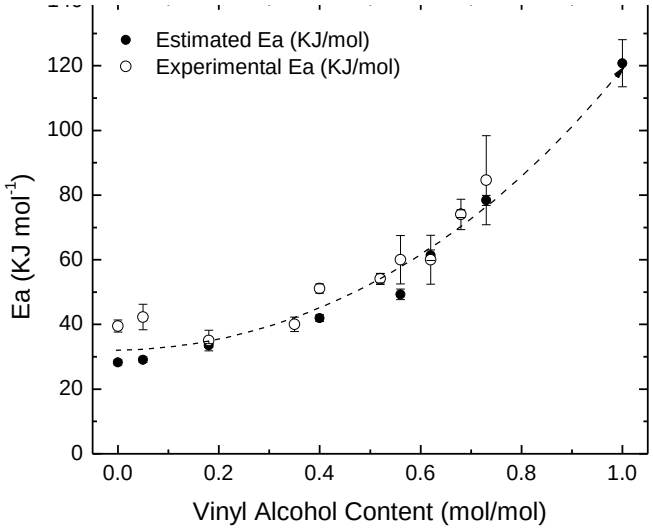

Figure 71. Energy of activation of diffusion versus vinyl alcohol content. The dashed line is drawn to indicate a trend.

The activation energy of diffusion increases with increasing vinyl alcohol content in both cases. Furthermore, an apparent continuous change in the rate of E_a increase is observed with increasing vinyl alcohol content. The rate of E_a increase may be elucidated as changes in the thermal expansivity of the base polymer. As vinyl alcohol content increases a redistribution of hole free volume is hindered by the increasing population density of hydrogen bonding moiety present in the chain backbone. This increased presence of intermolecular interaction retards expansion of preexisting holes as well as inherently changes the energy required for a permeant gas molecule to undergo diffusion. An effect that is more prominent with increasing concentration. The magnitude of the response depends on the strength of the interactions and mobility in the system.

Conclusions

In the current research a direct measurement of oxygen diffusion and solubility coefficients were obtained over a broad range of EVOH copolymers. A strong structural correlation to transport lead to the use of FTIR quantify the extent of hydrogen bonding. The width and intensity of the hydrogen bonded band increased with increasing vinyl alcohol content demonstrating an overall increase in concentration of intermolecular and intramolecular hydrogen bonded species. The structural parameters average hole free volume and cohesive energy density were measured with respect to copolymer concentration and show direct linear correlation. This allows for direct correlation to existing models involving low weight molecular transport phenomenon in amorphous solids. Although gas transport characteristics exhibit a general correlation with free volume, alone free volume cannot adequately describe gas barrier. The chain rigidity and the strength of intermolecular interactions are two additional important factors which are manifested via activation energy. We have shown through a correlation of cohesive energy density and glass transition that the degrees of freedom in expressions of kinetic energy of the chain backbones are constant across all EVOH copolymer compositions. Therefore, it was shown that the primary factor controlling free volume is not chain rigidity but cohesive energy in this system. A predictive approach based on hole free volume and cohesive energy density allows for determination of energy of activation, the controlling factor in transport temperature measurements.

References

1 . Alvarez, V.A.; Ruseckaite, R.A.; Vâzquez, A. *J. Appl.Polym. Sci***, 2003**, *90*, 3157

2 . Zhang, Z.; Britt, I.J.; Tung, M.A. . *J. Appl. Polym. Sci*, **2001**, *82*, 1866

3 . Iwanami, T.; Hirai, Y. *Tappi Journal*, **1983,** *66*,85

4 . Stern, S.A.; Trohalaki, S. In *Barrier Polymers and Structures*; Koros, W.J. Ed.; American Chemical Society, Washington DC, 1990

5 . Brandt, W.W. *J. Chem. Phys.* **1959**, *63*, 1080

6 . Meares, P.; *J. Am. Chem. Soc.* **1954**, *76*, 3415

7 . Ito, Kenji.; Saito, Yoichiro.; Yamamoto, Tomoyuki.; Ujihira, Yusike.; Nomura, Kiyoshi. *Macromol*, **2001**, *37*, 6153

8. Koopmans, J.J.; Van Der Linden, R.; Vansant, E.F. *J.Adhesion*, **1980**, *11*, 191-202.

9. Lee, K.M.; Han, C.D. *Macromolecules*, **2003**, *36*, 7165-7178.

10. Cheng, G. W.; Yu, Z.; Jamieson, A. M.; McGervey, J. D. *J. Appl. Polym. Sci.* **1997**, *63*, 483.

11. Kobayashi, Y.; Zheng, W.; Meyer E. F.; McGervey, J. D.; Jamieson, A. M. *Macromolecules* **1989**, *22*, 2302.

12. Kluin, J. E.; Yu, Z.; Vleeshouwers, S.; McGervey, J. D.; Jamieson, A. M.; Simha, R. *Macromolecules* **1993**, *26*, 1853.

13. Coleman, M. M.; Yang, X.; Zhang, H.; Painter P. C. *Journal of Macromolecular Science, Physics* **1993**, *B32*, 295-326.

14 . Yeh, J.-T.; Chen, H.-Y. *Journal of Material Science* **2007**, *42*, 5742-5751.

15 . Nir, Y.; Narkis, M. *Journal of Macromolecular Science, Physics* **1998**, *B37*, 863-882.

16 . Radmard, B.; Dadmun, M. D. *Polymer* **2001**, *42*, 1591-1600.

17 . Bunn, C. W.; Peiser, H. S. *Nature* **1947**, *159*, 162.

18. Nakamae, K.; Kameyama, M.; Matsumoto, T. *Polymer Engineering and Science* **1979**, *19*, 572-578.

19. Cerrada, M. L.; Perez, E.; Perena, J. M.; Benavente, R. *Macromolecules* **1998**, *31*, 2559-2564.

20. Takahashi, M.; Tashiro, K.; Amiya, S. *Macromolecules* **1999**, *32*, 5860-5871.

21 . Lagaron, J. M.; Gimenez, E.; Saura, J. J.; Gavara, R. *Polymer* **2001**, *42*, 7381-7394.

22. Alavaez, V. A.; Kenny, J. M.; Vazquez A. *Journal of Applied Polymer Science* **2003**, *89*, 1071-1077.

23. Lopez-Rubio, A.; Lagaron, J. M.; Gimenez, E.; Cava, D.; Hernandez-Munoz, P.; Yamamoto, T.; Gavara R. *Macromolecules* **2003**, *36*, 9467-9476.

24. Krasteva, M.; Cerrada, M. L.; Benavente, R.; Perez, E. *Polymer* **2005**, *46*, 9831-9839.

25 . Bunn, C. W. *Nature* **1948**, *161*, 929.

26 . Sakurada, I.; Fuchino, K.; Odada, N. *Bull. Inst. Chem. Res. Kyoto Univ.* **1950**, *23*, 78.

27. Assender, H. E.; Windle, A. H. *Polymer* **1998**, *39*, 4295-4302.

28. Yurovskikh, S. V.; Chvalun, S. N.; Lyoo, W. S. *Polymer Science* **2001**, *43*, 278-284.

29. Matsumoto, T.; Nakamae, K.; Ogoshi, N.; Kawasoe, M.; Oka, H. *Kobunshi Kagaku* **1971**, *28*, 610.

30 . Van Krevelen, O. W. In *Properties of Polymers*; Elsevier, Amsterdam 1990

31. Tao, S. J.; *J. Chem. Phys.* **1972**, *56*, 5499.

32. Nakanishi, H.; Wang, S. J.; Jean, Y. C. *Proceedings of the International Conference on Positron Annihilation in Fluids, Arlington, TX; World Scientific Publishing: Singapore*, **1987**; p 292.

33. Aharoni, S. M.; *J. Macromol. Sci. B* **1974**, *9*, 699.

34. (Alvarez, A., & Vasquez, 2003)Boyer, R. F. *Rubber Chem. Technol.* **1963**, *36*, 1303.

35. McKenna, L. W.; Kajiyama, T.; MacKnight, W. J. *Macromolecules* **1969**, *2*, 58.

36. Stehling, F. C.; Manderkern, L. *Macromolecules* **1970**, *3*, 242.

37 . Boyer, R. F. *Macromolecules* **1973**, *6*, 288.

38. Ohlberg, S. M.; Fenstermaker, S. S. *J. Polym. Sci*. **1958**, *32*, 514.

39. Cutler, D. J.; Glotin, M.; Hendra, P. J.; Jobic, H. *J. Polym. Sci., Polym. Phys. De*. **1979**, *17*, 907.

40. Rabold, G. P. *J. Polym. Sci., Part A-1* **1969**, *7*, 1203.

41. Lin, D.; Wang, S. J. *J. Phys.: Condens. Matter* **1992**, *4*, 3331.

42. Schurr, O.; Yamaki, B. S.; Wang, C.; Atvars, T. D. Z.; Weiss, R. G. *Macromolecules* **2003**, *36*, 3485.

43. Van der Berg, O.; Sengers, W. G. F.; Jager, W. F.; Picken, S. J.; Wubbenhorst, M. *Macromolecules* **2004**, *37*, 2460.

44. Davis, G. T.; Eby, R. K. *J. Appl. Phys.* **1973**, *44*, 4274.

45. Sekelik, D. J.; Stepanov, S. V.; Nazarenko, S.; Schiraldi, D.; Hiltner, A.; Baer, E. *J Polym Sci Part B: Polym Phys* **1999**, *37*, 847–857.

46. Polyakava, A.; Stepanov, S. V.; Nazarenko, S.; Shiraldi, D.; Hiltner, A; Baer, E. *J. Polym. Sci., Part B: Polym. Phys.* **1999**, *37*, 847-857.

47. Lin, J.; Shenogin, S.; Nazarenko, S. *Polymer* **2002**, *43*, 4733-4743.

48. Fujita, H.; Kishimoto, A. *J. Chem. Phys.* **1961**, *34*, 393.

49. Hayes, R. *Journal of Applied Polymer Science* **1961**, *5*, 318-321.

CHAPTER VII

CONCLUDING REMARKS

Solid-state structure, crystalline morphology, crystallization kinetics, thermal, free volume and gas transport properties of semicrystalline *syndiotactic* polystyrene (sPS) and ethylene vinyl alcohol copolymers (EVOH) have been investigated. Solid-state structure of sPS after crystallization from the melt and glassy state was examined by differential scanning calorimetry (DSC), density and wide angle x-ray diffraction analysis (WAXD). The measurements confirmed density of *syndiotactic* polystyrene crystalline forms, which in the case of α and δ_e was smaller than the glassy amorphous sPS density. Positron annihilation lifetime spectroscopy (PALS) experiments were conducted to study the free volume properties of these materials.

Chapter II explored syndiotactic polystyrene solid state structure, determination of the crystalline fraction, crystallization kinetics and nature of crystalline-crystalline transitions. Wide angle X-ray diffraction patterns of α, β, γ, δ and the mesomorphic phases are presented. Quantitative comparisons of the percent crystallinity for differential scanning calorimetry, wide angle X-ray diffraction and density are reported. Heat of fusion for 100% α and β crystalline sPS, 56 and 52 $\pm$ 1 J g^{-1} respectively, is obtained though extrapolation of $\Delta H = H_m - H_{cc}$ with respect to density for a series of melt-crystallized and crystalline-crystalline manipulated samples. Weight fraction crystallinity versus density linear regression demonstrates 100% γ form crystalline density to be 1.074 g cm^{-3}. Isothermal crystallization kinetics of γ phase sPS with respect to pressure is shown. Efficiency of step wise, carbon disulfide and supercritical CO_2 solvent extraction methods for removal of trapped solvents within the chlathrated δ form of sPS is also reported.

In Chapter III a dynamic gas permeation system utilizing mass-spectrometer (DGPS-MS) was successfully developed, based on the principles of the dynamic differential approach. A

powerful turbomolecular pumping system in the downstream compartment of the permeation cell helped the rapid establishment of the equilibrium concentration of permeant. With a NIST calibrated film and constant volume variable pressure setup, independent calibration was achieved for DGPS-MS. The permeation results of various gases through different polymer membranes demonstrated that DGPS-MS has the capability to measure from very fast (no more than a few minutes) to slow (a couple of days) diffusion of different gases and gas mixtures. The data obtained from DGPS-MS agreed well with the literature value(s).

The diffusion characteristics of amorphous, α, and β forms of sPS were successfully measured via the DGPS-MS system. It was shown that the amorphous and β forms demonstrate similar diffusion and did not vary depending on whether the diffusion was parallel or perpendicular to the chain axis. Conversely, experimental results as well as molecular dynamics simulations have shown that the unique "superstructure," packing of triplets forming hexagonally shaped nanochannels along the chain direction, found in the α" form of sPS facilitate high diffusion rates parallel to the chain direction in larger permeants (greater than 2.6Å). This was attributed to a transition from a nearly three-dimensional behavior for small permeant size, to a one-dimensional behavior for larger permeant sizes. Larger permeants are confined to the hexagonally shaped nanochannels between the triplets in the α" form and cannot move between parallel channels. The smaller permeants, however, can move relatively freely between neighboring channels, resulting in a more three-dimensional diffusion behavior.

In Chapter IV sorption isotherms have been measured for a variety of organic halide penetrants in amorphous atactic polystyrene and semicrystalline δ_e phase syndiotactic polystyrene thin films at 35°C and partial pressures below atmospheric. In all cases, penetrant sorption increases with increasing crystalline fraction, signifying greater loading capacity within the crystalline nanopore. The crystalline phase demonstrates capability to absorb chlorodecane but is impermeable to bromopentane, indicating factors other than size exclusion responsible for

crystalline nanoporous cavity capacity. Values of χ were extracted from Flory-Huggins expression and Gee's thermodynamic interpretation[1] of the relationship between solubility and critical temperature. Both methods showed excellent agreement and were used to characterize differences in χ value as it relates to monosubstituted linear organohalides of varying electronegativity in amorphous and δ_e semicrystalline syndiotactic polystyrene thin films. In general, δ_e syndiotactic polystyrene possesses a greater affinity for organohalides than the amorphous bulk matrix. The nanoporous cavity demonstrates a lower χ value for chloro-substituted penetrants and a progressively higher χ value as you progress from bromo- to iodo-containing organic halides.

A simple and standard diffusion model for sorption experiments traditionally based on the transient pressure decay method developed by Crank[2] was used to process quartz crystal microbalance weight uptake measurements. The time to reach equilibrium sorption in the δ_e phase is greater than that of the amorphous phase, demonstrating a reduced kinetic response intrinsic to the host cavity. Likewise, decreased kinetic response is observed with increasing alkyl chain length and systematically increased monosubstituted halide diameter. Attempts to fit experimental data to classic low molecular weight transport models such as the relationship between diffusivity and critical volume have failed. The diffusion process is still consistent with conceptual interpretation based on a sequence of unit diffusion steps or jumps during which the particle passes over a potential barrier separating one position from the next. Bromo- and iodo-pentane penetrans show much higher diffusion coefficients in crystalline samples, implying crystalline cavity exclusion from the diffusion process.

In Chapter VI a direct measurement of oxygen diffusion and solubility coefficients were obtained over a broad range of EVOH copolymers. A strong structural correlation to transport lead to the use of FTIR quantify the extent of hydrogen bonding. The width and intensity of the hydrogen bonded band increased with increasing vinyl alcohol content demonstrating an overall

increase in concentration of intermolecular and intramolecular hydrogen bonded species. The structural parameters average hole free volume and cohesive energy density were measured with respect to copolymer concentration and show direct linear correlation. This allows for direct correlation to existing models involving low weight molecular transport phenomenon in amorphous solids. Although gas transport characteristics exhibit a general correlation with free volume, alone free volume can not adequately describe gas barrier. The chain rigidity and the strength of intermolecular interactions are two additional important factors which are manifested via activation energy. We have shown through a correlation of cohesive energy density and glass transition that the degrees of freedom in expressions of kinetic energy of the chain backbones are constant across all EVOH copolymer compositions. Therefore, it was shown that the primary factor controlling free volume is not chain rigidity but cohesive energy in this system. A relation between hole free volume to cohesive energy density allows for determination of energy of activation, the controlling factor in transport temperature measurements.

References

1. Gee, G. *Quarterly Reviews* **1947,** *1*, 265.

2. Crank, J.; Park, G. S. In *Diffusion in Polymers*; Mendi, P. Ed.; Academic Press: London and New York, 1968.